UC Santa Barbara
UC Santa Barbara Electronic Theses and Dissertations

Title

Spectroscopic elucidation of surface reactions involved in the NO-CO reaction over atomically dispersed Rh/alumina catalysts

Permalink

https://escholarship.org/uc/item/15z6w06m

Author

Gadinas, Nick

Publication Date

2022

Peer reviewed|Thesis/dissertation

UNIVERSITY OF CALIFORNIA

Santa Barbara

Spectroscopic elucidation of surface reactions involved in the NO-CO reaction over

atomically dispersed Rh/alumina catalysts

A Thesis submitted in partial satisfaction of the

requirements for the degree Master of Science

in Chemical Engineering

by

Nicholas L. Gadinas

Committee in charge:

Professor Phillip Christopher, Chair

Professor Susannah Scott

Professor Michael Gordon

September 2022

The thesis of Nicholas L. Gadinas is approved.

_____

Susannah Scott

_____

Michael Gordon

_____

Phillip Christopher, Committee Chair

August 2022

ABSTRACT

Spectroscopic elucidation of surface reactions involved in the NO-CO reaction over
atomically dispersed Rh/alumina catalysts

by

Nicholas L. Gadinas

Over the last 50 years, the reduction of automotive emissions has been a critical component of environmental legislation. The catalytic converter is one of the tools used by automotive engineers to reduce emissions: it facilitates the conversion of residual fuels and CO to CO_2 and the reduction of NO_x to N_2 over the 'three-way catalyst' (TWC) containing a mix of precious metals, such as Pt, Rh, or Pd supported on high surface area γ-Al_2O_3. NO_x reduction is accomplished by Rh, and while it achieves nearly complete conversion to N_2 at steady state operating conditions, harmful emissions such as NH_3 and N_2O are produced during startup.

Previous studies identified a mix of Rh particles and atoms in typical TWC formulations, and others found that Rh atoms are responsible for NH_3 production in the presence of NO, CO, and H_2O (which is present in automotive exhaust). We aim to study aspects of the mechanism of NO reduction over atomically dispersed Rh/γ-Al_2O_3 catalysts to inform the design of catalysts and control systems that limit the production of harmful emissions. We focus on the dry reduction of NO by CO (no H_2O), as this will serve as the base

case for future studies including water and employ a combination of *in situ*, temperature programmed, and cryogenic infrared (IR) spectroscopy with UV photolysis in our study.

First, we found that the stable Rh dicarbonyl, $Rh(CO)_2$, is the most abundant Rh species during the reaction in 0.5 kPa CO and 0.1 kPa NO (5000 ppm and 1000 ppm, respectively) at 205 °C, which models dry reaction conditions during startup of the catalytic converter. The abundance of $Rh(CO)_2$ suggests that reactions involving this species initiate the catalytic cycle. Experimental and theoretical study of the influence of surface *OH (* denoting species adsorbed on γ-Al_2O_3 or Rh) on $Rh(CO)_2$ found that high local *OH density on the support (in excess of ~10 *OH nm^{-2}) near $Rh(CO)_2$ lowers *CO vibrational frequency and energy barriers to *CO desorption while stabilizing a monocarbonyl intermediate, Rh(CO). At reaction conditions, it is likely that $Rh(CO)_2$ in *OH dense regions of γ-Al_2O_3 are the most active species, and that $Rh(CO)_2$ is directly coordinated to a *OH ligand shared with the support.

After *CO desorbs from $Rh(CO)_2$, Rh was initially assumed to interact with gaseous NO to form a mixed $Rh–(NO)_x–CO$ intermediate during NO reduction, but this could not be verified *in situ* due to the presumed rapid reactivity of this intermediate and the abundance of $Rh(CO)_2$ species. Therefore, we used photolysis to induce *CO desorption from $Rh(CO)_2$ at cryogenic temperature in the presence of NO to form and kinetically trap what we believe is $Rh(CO)(NO)_2$, which was highly reactive below –75 °C. The assignment of this species and its speculated participation in the reaction mechanism is supported by previous studies of NO reduction by CO by homogeneous Rh catalysts and by density functional theory (DFT) calculations presented in this work. Finally, we extended the boundary of Rh interactions with support species by identifying reactions between $Rh(CO)_2$ and NO-derived species on γ-Al_2O_3 at cryogenic temperature which consume $Rh(CO)_2$ and oxidize Rh.

In this work, we establish the kinetic relevance of $Rh(CO)_2$ consumption to the NO-CO reaction over atomically dispersed $Rh/\gamma\text{-}Al_2O_3$ and identify three processes that could be involved: *CO desorption followed by formation of $Rh(CO)(NO)_2$ and subsequent reaction, reaction of $Rh(CO)_2$ with NO-derived surface species on $\gamma\text{-}Al_2O_3$, and a Rh redox cycle. We also demonstrate the feasibility of UV photolysis for the generation and observation of reactive intermediates. Finally, we propose further experiments to determine which of the three processes are relevant to NO reduction over atomically dispersed $Rh/\gamma\text{-}Al_2O_3$ at TWC conditions.

Table of Contents

1. Introduction

The rapid industrialization of the 19th century led to the development of many large-scale chemical processes, and with these processes came environmental emissions that became an increasing focus of regulators. The U.S. Clean Air Act of 1970 posed an enormous regulatory hurdle for automotive manufacturers in particular, as centralized methods of pollution control would not be feasible to reduce the emission of contaminants from internal combustion engines, including hydrocarbons, carbon monoxide (CO), and nitrogen oxides (NO_x, x = 1, 2). Instead, a highly efficient distributed chemistry would have to be employed to match the scale of the automobile and meet ever stricter emissions standards. This technology was developed in the 1960s and became standard in the market in 1975 as the catalytic converter.[1]

The catalytic converter contains a high surface area ceramic monolith onto which the three-way catalyst (TWC) is deposited. So named for its ability to catalyze three types of reactions, the TWC contains mixtures of precious metals such as Pt, Pd, and Rh, which catalyze the combustion of hydrocarbons, oxidation of CO, and reduction of NO_x to N_2. The reduction of NO_x to the desired product N_2 and simultaneous oxidation of CO is often performed by Rh supported on γ-Al_2O_3 in the TWC due to its excellent steady state NO_x reduction performance.[2] At low temperature (e.g., during engine startup), however, NO_x reduction over Rh produces unwanted compounds such as the greenhouse gas N_2O and pollutant NH_3.[3] A mechanistic understanding of NO_x reduction that explains the formation of these compounds can inform exhaust control systems and TWC design, assisting manufacturers seeking to further reduce automotive emissions.

TWC formulations typically contain less than 0.5% Rh by weight supported on γ-Al$_2$O$_3$, which leads to a mix of Rh particles and atomically dispersed species.[4–6] The structure of γ-Al$_2$O$_3$ supported Rh is also known to change with environmental conditions: adsorbed *CO and *NO (* denoting adsorbed species) affect the relative stability of atomically dispersed and particle Rh structures,[7–14] and the high mobility of Rh on γ-Al$_2$O$_3$ allows speciation to proceed at nontrivial rates.[15] This dynamic structural behavior makes it difficult to establish structure-function relationships for Rh/γ-Al$_2$O$_3$ catalysts without an understanding of each Rh structure present in the catalyst under varying reaction conditions. Past mechanistic investigations of Rh catalysts for NO$_x$ reduction often focused on extended Rh surfaces and oxide supported Rh particles, where NO reduction proceeds via the dissociation of *NO which leads to the recombination of *N to form N$_2$ and scavenging of *O by CO to form CO$_2$.[16] Isolated Rh atoms on γ-Al$_2$O$_3$ offer no adjacent Rh sites available for *NO dissociation and are typically in the +1 oxidation state after reductive treatment, whereas Rh particles contain primarily metallic Rh.[11,17,18] These differences imply that the mechanism of NO reduction over atomically dispersed Rh should be quite dissimilar from that over Rh particles.

These expected mechanistic distinctions are further motivated by differences in reactivity and selectivity between Rh particles and atoms supported on γ-Al$_2$O$_3$. In dry NO reduction by CO (reaction mixture of 0.5 kPa CO, 0.1 kPa NO, balance Ar), light-off (onset of reactivity) occurs at slightly higher temperature on Rh atoms than on Rh particles, suggesting atoms are less reactive. Yet in the presence of water, the reactivity trend is reversed as the Rh atom catalyzed reaction lights off 50 °C lower than the particle catalyzed reaction, and Rh atoms selectively produce NH$_3$ while particles produce N$_2$ and N$_2$O.[19] Preliminary unpublished steady state reactivity studies of dry (in the absence of water) NO reduction suggest that Rh

2

particles are more selective to N_2O, while Rh atoms favor N_2 (205 °C, 0.5 kPa CO, 0.1 kPa NO, isoconversion). Interestingly, the oxide support composition appears to influence the relationship between Rh particle and atom reactivity. For example, a recent study[20] of Rh/CeO_2 found that Rh^{+1} atoms were substantially more reactive than Rh^0 particles even during dry NO reduction by CO: Rh atoms reached full conversion in this Rh/CeO_2 system at 100 °C, whereas Rh particles, generated by high temperature H_2 reduction, reached only 5 % conversion at 120 °C. This distinction between Rh/Al_2O_3 and Rh/CeO_2 may originate from differences in Rh–support interactions between the irreducible Al_2O_3 and reducible CeO_2, which should be more pronounced for isolated Rh atoms than for Rh particles, on which the extended Rh surfaces may be insulated from Rh–support interactions. In the TWC, Rh is typically supported on γ-Al_2O_3 due to its high surface area, which facilitates high Rh dispersion and efficient use of the precious metal.[21]

In NO reduction by CO over Rh/CeO_2, reaction of Rh(CO)$_2$ with NO was proposed to proceed via multiple adsorption of NO, *NO dimerization, and rapid decomposition of Rh(CO)(N_2O_2) based on IR spectroscopic observation of N_2O generation with loss of Rh(CO)$_2$ and preliminary DFT calculations.[20] NO probe molecule IR also indicated that reaction of Rh(CO)$_2$ with NO led to oxidation of Rh^{+1} to Rh^{+3}, suggesting the involvement of a Rh redox cycle. This work parallels studies of NO reduction over homogeneous [RhCl$_2$(CO)$_2$]$^-$, in which the formation of [RhCl$_2$(CO)(NO)$_2$]$^-$ was proposed as an intermediate species based on the stoichiometric evolution of N_2O and CO_2.[22,23] We propose similar species in the atomically dispersed Rh/γ-Al_2O_3 system, as discussed in this text. Other mechanisms for NO reduction catalysis by atomically dispersed Rh/SiO_2 have been proposed from a combined theoretical and spectroscopic study; they begin with mixed Rh(NO)(CO) species decomposing to form

CO_2 and Rh(N) which then continues to react through one of two pathways which generate NCO or N_2O, and finally N_2.[24] These proposed mechanisms suggest details of interactions between Rh atoms and gas phase species and reactions between adsorbates on Rh sites. They do not discuss interactions between atomically dispersed Rh and species present on the oxide support, into which we provide further insight.

The agglomeration of Rh atoms into particles during light-off of NO reduction has also been noted as an important factor in reactivity of Rh catalysts,[13,25] but we have focused our study solely on the action of Rh atoms. Conversion of atoms to particles may be an important component of the mechanism at conditions *after* start-up of the catalytic converter, but in the low temperature regime (~ 200 °C) we have found the Rh atoms remain the dominant Rh species in low loading catalysts ($\leq$ 0.1 wt.% Rh). However, the well documented reconstruction of Rh sites should be considered during synthesis and characterization of ostensibly atomically dispersed Rh catalysts to ensure that effects of particles do not influence the study of Rh atoms.

The primary experimental tool in the current study was diffuse reflectance infrared Fourier transform spectroscopy (DRIFTS, also abbreviated as FTIR or IR in this text) with CO and NO as probe molecules. Infrared spectroscopy[26] probes the energy and intensity of vibrational transitions of molecules, provided that the transitions alter the dipole moment. The frequency of molecular vibrations can be described using the harmonic oscillator model for diatomic molecules, in which both the force constant (corresponding to bond strength) and reduced mass of the oscillator (relating to the masses of atoms forming the bond) control the frequency. The energy of transitions between different vibrational modes often falls in the infrared range, so absorption of IR light can be used to probe the existence of different molecular vibrations. Vibrations of more complex molecules (2+ atoms) include bending and

combination vibrations, allowing for observation of multiple features for the same species. IR spectroscopy equipment is also readily available at the benchtop scale, so it is an attractive analytical tool especially for systems that contain simple molecules or well-defined vibrations in molecules of interest.

DRIFTS is an application of IR spectroscopy in which infrared light is reflected off a powder sample via diffuse reflection between particles in order to probe vibrational transitions occurring within the sample. This is suitable for characterization of heterogeneous catalyst powders, since samples can be loaded into the DRIFTS cell and analyzed without additional treatment, such as dispersion with solvents or the use of specialized support materials. The use of *in situ* DRIFTS cells provides reasonable representations of reactor conditions, and thus enables connections between kinetic and spectroscopic data collected in different reactors.

In this work, NO and CO are used as probe molecules for low loading $Rh/\gamma-Al_2O_3$ catalysts. Interactions of both molecules with Rh have been studied for decades, with Yang and Garland[27] identifying numerous Rh–CO structures in IR in 1957 which have been confirmed in studies since.[5,12,28–33] Specifically, the presence of Rh clusters and atoms can be probed via the vibration of adsorbed *CO molecules: CO adsorbs to particles in linear or bridged configurations, leading to IR peaks near 2060 and 1860 cm^{-1}, respectively, while CO adsorbs to Rh atoms to form the Rh *gem*-dicarbonyl ($Rh(CO)_2$), which exhibits two peaks near 2085 and 2015 cm^{-1}, corresponding to the coupled symmetric and asymmetric vibrations of both *CO molecules. NO probe molecule IR has also been used to identify types of Rh sites and the nature of *NO adsorbates. The free valence electron of NO leads to formation of both cationic and anionic *NO ligands, which affects the frequency of *NO vibrations.[22] More cationic *NO exhibits IR peaks above 1900 cm^{-1}, while anionic *NO has peaks typically below

1800 cm^{-1}.[30,33,34] As with *CO, the nature of the Rh site also affects *NO frequency, with Rh particles leading to lower adsorbed *NO frequencies (~1685 cm^{-1}) due to stronger Rh–NO interactions and a consequently weaker N–O bond.[29] The Rh dinitrosyl, Rh(NO)$_2$, has also been observed in some studies,[31,35] but its observation appears to vary significantly with experimental conditions, including the composition of the support.

Our investigation of the behavior of atomically dispersed Rh/γ-Al$_2$O$_3$ during NO reduction by CO begins first by characterizing the primary adsorbed ligands on the Rh sites under reaction conditions and then extends to the local environment surrounding these sites. With *in situ* IR spectroscopy, we identify Rh(CO)$_2$ as the primary form of Rh during catalysis, the consumption of which is likely a kinetically relevant step in NO reduction. Using a combination of *in situ*, temperature programmed, and cryogenic IR spectroscopy with UV photolysis, we produce proposed reaction intermediates (e.g. Rh(CO)(NO)$_2$) and also characterize interactions between Rh(CO)$_2$ and nearby *OH and NO-derived species on γ-Al$_2$O$_3$ that may be relevant for catalysis. These reactions also indicate that a Rh redox cycle may be involved in catalysis. In total, the data are consistent with two potential routes of Rh(CO)$_2$ consumption: *CO desorption from Rh(CO)$_2$, followed by NO adsorption to form Rh(CO)(NO)$_2$ and its subsequent reaction, and reactions between Rh(CO)$_2$ and surface bound NO-derived species. We propose further experiments to determine which of these processes is operative at TWC conditions.

2. Experimental Methods

2.1. Catalyst Synthesis

Rh/γ-Al$_2$O$_3$ catalysts (0.1 and 0.05 wt.%) were synthesized using dry impregnation of γ-Al$_2$O$_3$ (Sasol, Puralox TH 100/150) with a solution of Rh^{+3} nitrate hydrate (Sigma Aldrich) in HPLC-grade water (J.T. Baker) (1.5:1 ratio of solution to catalyst by mass) added in 200 μL increments. The catalyst was dried overnight in an oven at 100 °C, then calcined under flowing dry air at 350 °C for 4 hours in a tube furnace.

2.2 Infrared Spectroscopy

FTIR of the Rh/γ-Al$_2$O$_3$ catalysts in this work was performed in a Harrick Scientific DRIFTS cell equipped with a liquid nitrogen dewar (Praying Mantis Low Temperature Reaction Chamber inside a Praying Mantis Diffuse Reflection Accessory) using a Nicolet iS10 FTIR spectrometer equipped with a mercury cadmium telluride (MCT) detector. The temperature of the Harrick cell was controlled by a thermocouple in the catalyst bed and a heater beneath the bed connected to a temperature controller (Omega CN7800) along with liquid nitrogen to reach cryogenic temperatures. Previous studies[36] of DRIFTS cells of similar design to those used in these experiments indicate that thermal gradients within the bed can lead to temperature differences between the bed thermocouple reading and actual average bed temperature of up to approximately 20 °C, that is, the actual average temperature is up to 20 °C less than the thermocouple reading at relevant conditions. This uncertainty is more important for quantitative measurements rather than describing qualitative trends, as discussed with Redhead analysis below. Gas flow to the cell was regulated with mass flow controllers (Teledyne Hastings Digital 300 & HFC-202). Cryogenic measurements were performed under

vacuum pressure in the cell. Spectra were collected by averaging between 8 and 16 scans each with a data spacing of 0.482 cm^{-1}. Prior to all experiments, catalysts were pretreated *in situ* under flowing O$_2$ (Airgas) for 30 minutes at 350 °C and reduced under flowing 10% H$_2$/Ar (Airgas) for 1 hour at 100 °C (IR in Chapter 3) or 190 °C (IR in Chapters 4–6). Further details of specific experiments are provided in the text.

Temperature-programed desorption (TPD) measurements were executed by heating the sample in Ar at a rate (β) of 20 °C min^{-1} until all *CO desorbed while taking spectra continuously. The rate of band intensity loss was traced using the change in peak areas of deconvoluted spectra, integrated and fit using Origin® by fixing constant peak FWHM and positions. We estimate the CO binding energy range by solving the following form of the Redhead analysis equation numerically in MATLAB, similarly to our prior work:[53]

$$\ln\left(\frac{\beta}{k_B T_P^2}\right) = \frac{-E}{k_B T_P} + \ln\left(\frac{A}{E}\right) \tag{1}$$

where E is the binding energy, T_P is the peak desorption temperature, k_B is the Boltzmann constant, β is the temperature ramp rate (0.33 K s^{-1}), and A is the pre-exponential factor. When estimating the CO binding energy without an entropic barrier ($\Delta S = 0$), we use a preexponential factor (A) of 10^{13},[37] based on previous analysis of flat Rh surfaces where single molecular desorption occurs.[38] When estimating the upper limit of the CO binding energy, the pre-exponential factor (A) used is 6×10^{11} s^{-1} for a CO entropic desorption barrier of 52 J mol K^{-1} from Rh(CO)$_2$, as calculated in previous work.[39] Uncertainty of bed temperature readings can lead to overestimation of the peak desorption temperature T_P of up to 20 K, which is factored into the lower limit of binding energies. From these energies, we can estimate desorption enthalpy, ΔH:

$$\Delta H = E - RT_P \qquad\qquad (2)$$

where R is the ideal gas constant.

2.3. Photolysis of Rh/γ-Al₂O₃ Catalysts

The Rh–CO bond of $Rh(CO)_2$ has an electronic transition near 3.9 eV which can be excited by ultraviolet light,[40] which has been exploited in previous studies[40,41] to induce *CO desorption from $Rh(CO)_2$ at cryogenic temperatures. This technique is applied in this work for identification of Rh intermediates formed from $Rh(CO)_2$. Photolysis of the 0.1 wt% Rh/γ-Al₂O₃ catalyst was performed while the catalyst was monitored with DRIFTS in the low temperature Harrick cell using a 370 nm LED light source operated at 90 W. The LED was positioned directly adjacent to the Harrick cell containing the catalyst and directed towards the window above the catalyst bed. The light intensity that reached the catalyst bed was estimated to be less than 20 mW cm^{-2} based on measurements taken at the window of the DRIFTS cell. In low temperature photolysis experiments, the catalyst was cooled to between –115 and –125 °C under vacuum to collect a background spectrum after pretreatment, then heated to 150 °C and exposed to 5000 ppm CO prior to illumination. After Rh sites were saturated with *CO in the form of $Rh(CO)_2$, the catalyst was again cooled to cryogenic temperature. Photolysis was performed in flowing Ar or NO (under vacuum pressure) while collecting DRIFTS spectra. After photolysis, the catalyst bed was warmed to ambient temperature in flowing Ar or 5000 ppm CO, and then heated to 400 °C at 20 °C min^{-1} in 5000 ppm CO or a mixture of 5000 ppm CO and 1000 ppm NO. The temperature could not be controlled during warming from cryogenic to ambient temperature, but warming in all experiments followed approximately the

same first order behavior, shown in Figure 1. Additional details pertaining to each experiment are provided in the text.
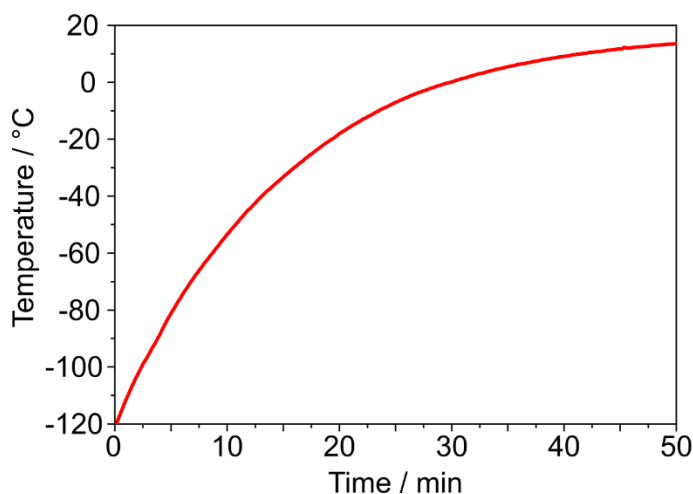
Figure 1. Temperature profile of the DRIFTS cell when warming from cryogenic to ambient temperature.

2.4. NO reduction light-off reactions

"Light-off" experiments were performed to test the reactivity of atomically dispersed Rh catalysts, where the reactor was heated at a constant rate under reactive environments from ambient temperature, mimicking engine start-up conditions. Catalysts were diluted with purified SiO_2 (Sigma Aldrich, CAS: 84878) to 2 mg Rh g_{cat}^{-1} in a home-built, temperature-controlled reactor system with mass flow controllers (Teledyne Hastings) to control CO, NO, H_2O and Ar gas flow concentrations. After pretreatment identical to that used before FTIR characterization (with the 100 °C reduction), catalysts were heated by 0.0833 °C s^{-1} from 20 to 450 °C while 4.17 cm^3 s^{-1} of 0.5 kPa CO and 0.1 kPa NO in Ar gas (1 bar total) flowed over a packed bed. Gas phase product compositions were identified by flowing reactor effluent through a Thermo Scientific Antaris IGS 2-meter Gas Cell set in a Nicolet iS10

10

FTIR spectrometer with a Mercury Cadmium Telluride (MCT) detector and using OMNIC Series Software to take 5 spectral scans every 10 s at high 0.5 resolution and 0.241 cm^{-1} data spacing. Reactants and products were calibrated with the TQ Analyst Pro Edition Software to identify established spectral signatures of known mixtures of CO, NO, N_2O, NH_3, CO_2, and H_2O in Ar at set pressure and temperature.

3. Hydroxyl Interactions with Rh(CO)$_2$

Adapted from:
Hoffman, A. J.; Asokan, C.; Gadinas, N.; Schroeder, E.; Zakem, G.; Nystrom, S. v.; Getsoian, A.; Christopher, P.; Hibbetts, D. Experimental and Theoretical Characterization of Rh Single-Atoms Supported on γ-Al2O3 with Varying Hydroxyl Content during NO Reduction by CO. *In Revision for publication in ACS Catalysis*.

The γ-Al$_2$O$_3$ surface has many local environments to host supported Rh species. Undercoordinated edge sites on γ-Al$_2$O$_3$ particles can be critical for some chemistries, such as ethanol dehydration.[42–45] These edges may also border different facets that are heterogeneously distributed on the γ-Al$_2$O$_3$ surface; previous microscopy studies have shown that the size of γ-Al$_2$O$_3$ facets can approach the nanometer scale.[46] Theoretical studies have suggested an *OH ligand is bound to Rh^{+1}(CO)$_2$ species supported on γ-Al$_2$O$_3$;[47] however, such studies did not account for a range of possible *OH concentrations on the surface, the effects of changing Rh oxidation states due to redox interactions with ligands, or compare calculations with experimental characterization data. The *OH species on the surface of γ-Al$_2$O$_3$ vary in concentration and structure with conditions according to DFT calculations of a γ-Al$_2$O$_3$ model derived from dehydrated boehmite,[48–52] and thermogravimetric and surface area analyses suggest that average coverages can range from 8–12 *OH nm^{-2} at the temperatures relevant to *CO desorption (573–673 K).[53,54] These 8–12 *OH nm^{-2} are not evenly distributed over the γ-Al$_2$O$_3$ surface—DFT in this work suggests that equilibrium *OH coverage is highly dependent on surface facet, so some regions of γ-Al$_2$O$_3$ exceed the average *OH coverage while others do not. Neighboring *OH may also form hydrogen bonding networks: at high coverage, densely packed *OH can form ice-like regions on the support,[55] and *OH gathered in surface depressions can form nest-like structures where water can accumulate,[56,57] similar to hydrogen

bond networks of silanol nests in zeolites.[58–62] Altogether, γ-Al$_2$O$_3$ presents a range of distinct *OH environments to atomically dispersed Rh species on the surface.

Studies of γ-Al$_2$O$_3$ hydroxyl groups have identified classes of *OH with different vibrational frequencies, acidities, and coordination to the support.[43,63,64] In general, *OH with sharp IR peaks and frequencies above 3650 cm^{-1} are considered "free," rather than part of a larger hydrogen bonding network, which exhibits a broad absorbance band centered between 3300–3400 cm^{-1}. Distinctions between free *OH with frequencies above 3650 cm^{-1} have been ascribed to varying number and type of coordinating Al support atom, and the acidity of free *OH increases with decreasing vibrational frequency (indicating a weaker O–H bond). Interactions between *OH, CO, and Rh have been previously observed: IR bands associated with *OH at 3679 and 3735 cm^{-1} decrease when CO is introduced to a 2.2 wt. % Rh/γ-Al$_2$O$_3$ sample while symmetric and asymmetric Rh(CO)$_2$ peaks grow, indicating that particular *OH are displaced or consumed during the dispersion and oxidation of Rh clusters to Rh^{+1}(CO)$_2$.[18,65] Interestingly, exposing the Rh/γ-Al$_2$O$_3$ to NH$_3$ mitigates the Rh dispersal process by bonding to the free γ-Al$_2$O$_3$ *OH groups that would otherwise be consumed during dispersion.[66] Clearly, interactions involving Rh, *OH, and gas phase species are critical to the nature of active sites under NO reduction conditions.

Rh species are likely deposited on several facets and in different *OH environments during synthesis but can become mobile and reconstruct on γ-Al$_2$O$_3$ depending on changing surface environments during catalyst pre-treatment and reaction conditions. CO-induced restructuring of atomically dispersed Rh/γ-Al$_2$O$_3$ relies on the migration of Rh(CO)$_2$ across the γ-Al$_2$O$_3$ surface to produce spatially isolated Rh species or to induce their re-agglomeration.[5,11–13,15,67,68] Consequently, sintering of atomically dispersed Rh can be

suppressed by anchoring organic ligands to limit Rh mobility.[39,69] Rh cluster disintegration can occur on the order of seconds when exposed to CO near ambient temperature, according to time-resolved EXAFS, with a low 17 kJ mol^{-1} barrier to Rh(CO)$_2$ formation from initially adjacent Rh atoms.[15] These results are reasonable, considering DFT studies of Pd diffusion that indicated an activation barrier between 15 and 72 kJ mol^{-1} for diffusion across dehydrated and hydrated (110) γ-Al$_2$O$_3$ surfaces, respectively.[70] The high mobility of Rh atoms may allow them to traverse the γ-Al$_2$O$_3$ surface and sample a range of surface facets, local adsorbate environments, and *OH coverages at relevant reaction conditions.

The construction of representative structural models of working catalytic active sites requires first identifying the structural elements present under operando conditions. *In situ* FTIR provides insights into the Rh structure during NO reduction by CO and the predominant adsorbate that saturates the active sites. Upon exposure to conditions of realistic TWC operation, 0.5 kPa CO and 0.1 kPa NO (5000 and 1000 ppm, respectively) at 205 °C, atomically dispersed Rh species exist predominantly as Rh(CO)$_2$ with characteristic frequencies at 2084 and 2012 cm^{-1} and without peaks associated with *NO on Rh expected in the range of 1900–1700 cm^{-1} (Figure 2).[5,12,30,31,34,35] Additionally, exposure of a CO-saturated catalyst to the mixture of NO and CO at 478 K (where the catalyst is reactive) does not cause the intensity of Rh(CO)$_2$ bands to decrease (Figure 3a). These data indicate that atomically dispersed Rh is primarily coordinated to CO, rather than NO, at conditions similar to those in automotive exhaust treatment. This preference for *CO on Rh atoms contrasts with Rh nanoparticles and surfaces, where NO adsorbs more strongly than CO resulting in an *NO saturated Rh surface under similar conditions.[29,71]
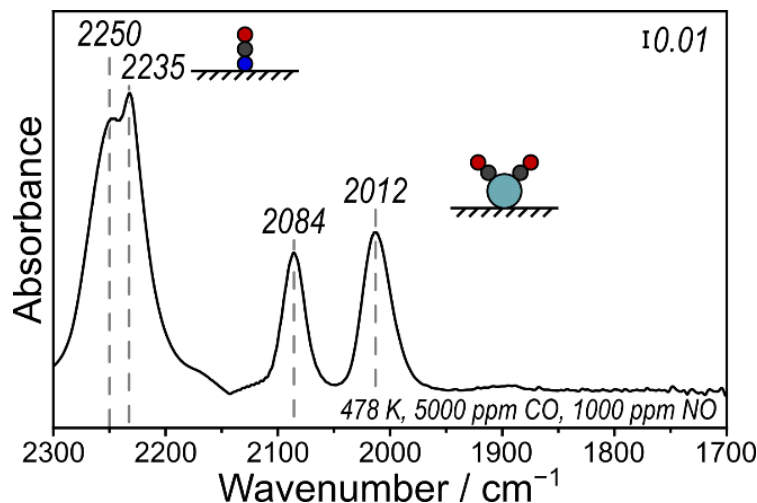
Figure 2. *In situ* IR spectra of 0.1 wt. % Rh/γ-Al$_2$O$_3$ during NO-CO reactions at 478 K for 600 s (0.5 kPa CO and 0.1 kPa NO, Ar balance, 1 bar total). Inset cartoons show the assigned species associated with the observed bands where oxygen is red, carbon is grey, nitrogen is blue and Rh is cyan.

Other features appear at 2255 and 2235 cm^{-1} under dry NO-CO reaction conditions, which are assigned to adsorbed *NCO species on Al$_2$O$_3$. IR spectra of a 0.05 wt. % Rh/γ-Al$_2$O$_3$ sample shows similarly shaped but shifted bands when exposed to ^{12}CO and ^{13}CO mixed with NO (Figure 3b). Both the sets of symmetric and asymmetric Rh(CO)$_2$ stretches and the features near 2230–2250 redshift by ~50 cm^{-1}, indicating that each is associated with species containing C, which further indicates the 2230–2250 cm^{-1} bands pertain to *NCO. Prior work[72,73] has indicated that such *NCO species can spill over onto the γ-Al$_2$O$_3$ support once formed during NO reduction by CO on Rh/γ-Al$_2$O$_3$, which is confirmed by the slow growth of these features without loss of Rh(CO)$_2$ in IR spectra collected at 523 K (Figure 3c). Thus, we conclude that *NCO is only adsorbed on the γ-Al$_2$O$_3$ support, while atomically dispersed Rh species exist almost exclusively as Rh(CO)$_2$ species under reaction conditions, so we focus on understanding the characteristics of Rh(CO)$_2$ as the catalyst approaches reaction conditions.

15
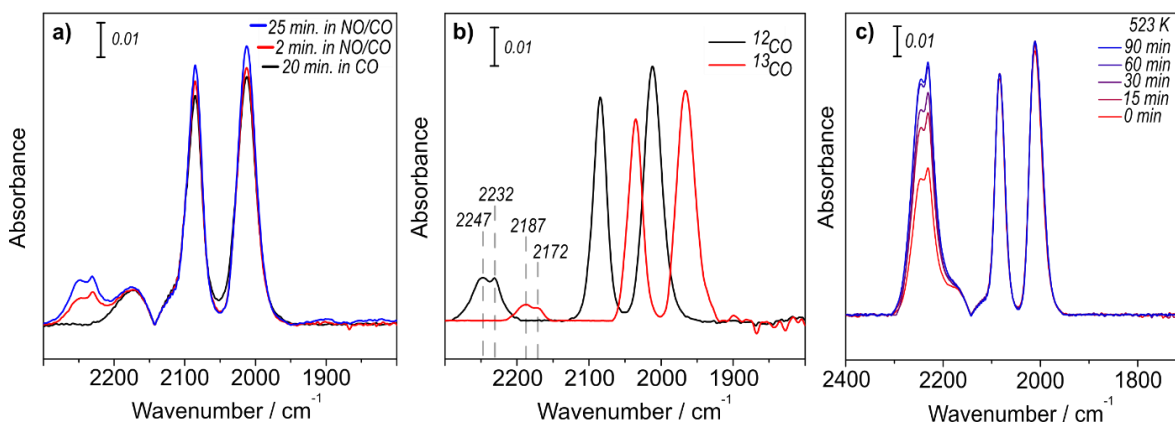
Figure 3. IR spectra of 0.05 wt.% Rh/γ-Al$_2$O$_3$ (a) during exposure to 0.5 kPa CO and 0.1 kPa NO (blue, red) after saturation with 0.5 kPa CO at 463 K (black), (b) after 25 minutes in 0.5 kPa CO and 0.1 kPa NO at 463 K (purged with Ar) (black) and after saturation with 10 kPa ^{13}CO and a pulse of 1 kPa NO at 463 K (purged with Ar) (red), and (c) during exposure to 0.5 kPa CO and 0.1 kPa NO at 523 K after exposure to the same mixture at 473 K. All gas mixtures were balanced with Ar.

The *CO stretching bands characteristic of the symmetric and asymmetric frequencies of Rh(CO)$_2$ species are observed at 2094 and 2020 cm^{-1} in CO probe molecule IR in Ar at 298 K, after the 0.1 wt. % Rh/γ-Al$_2$O$_3$ catalyst was pretreated *in situ* for 0.5 h at 623 K in pure O$_2$ at 1 bar and subsequently in 10 kPa H$_2$/Ar at 373 K and saturated by flowing 1% CO (Figure 4a). The absence of CO bands in IR spectra at frequencies characteristic of linear (~2080–2040 cm^{-1}) and bridge- or three-fold bound (~1950–1850 cm^{-1}) *CO on Rh clusters confirms that Rh exists primarily as atomically dispersed species following CO exposure in this sample.[29,71] Both the symmetric and asymmetric Rh(CO)$_2$ vibrational bands are asymmetric in shape and broad (> 30 cm^{-1} FWHM), suggesting the presence of multiple Rh(CO)$_2$ coordination environments.[15,20,74,75] Temperature programmed desorption (TPD) of *CO from the 0.1 wt. % Rh catalyst proceeds nonuniformly across both the symmetric and asymmetric Rh(CO)$_2$ bands, as the asymmetry shifts to lower frequency within each peak. This suggests that there are distinct Rh(CO)$_2$ species on the γ-Al$_2$O$_3$, each with its own characteristics symmetric and asymmetric frequencies; deconvolution of FTIR spectra yields good fits to the data by

including two pairs of peaks at 2094/2020 and 2084/2010 cm^{-1}, with full widths at half-maximum (FWHM) of 11/12 and 22/29 cm^{-1}, respectively (Figure 4b).

As the temperature increases from 293 to 493 K, the deconvoluted bands at 2094 and 2020 cm^{-1} decrease in intensity together while the bands at 2084 and 2010 cm^{-1} grow, suggesting that both species are $Rh(CO)_2$ and that the first converts to the second species as temperature increases. At 493 K, the 2084 and 2010 cm^{-1} peaks reach maximum area before decreasing. The peak positions and widths of the 2084 and 2010 cm^{-1} features were identified following complete loss of the 2094 and 2020 cm^{-1} features to enable deconvolution of the $Rh(CO)_2$ peaks in each spectrum during the TPD. The loss of the 2084 and 2010 cm^{-1} features is followed by the emergence and growth of bands at ~1985–1975 cm^{-1}, which reach a maximum area at 603 K. Previous work on atomically dispersed Rh/TiO_2 suggests that these bands appear because *CO desorbed sequentially from $Rh(CO)_2$ to form an $Rh(CO)$ intermediate when the Rh is complexed to an *OH species on the support.[76–78] Consistent with this, we observe that *CO desorbs sequentially from atomically dispersed Rh/γ-Al_2O_3; after the first *CO desorbs, $Rh(CO)$ species remains with *CO vibrational stretches of 1985–1975 cm^{-1}. The most prominent $Rh(CO)$ peaks appear at 1985 and 1975 cm^{-1} as distinct species; however, the large FWHM of these peaks (39 and 45 cm^{-1}, respectively) indicate that the local environment around $Rh(CO)$ varies significantly.
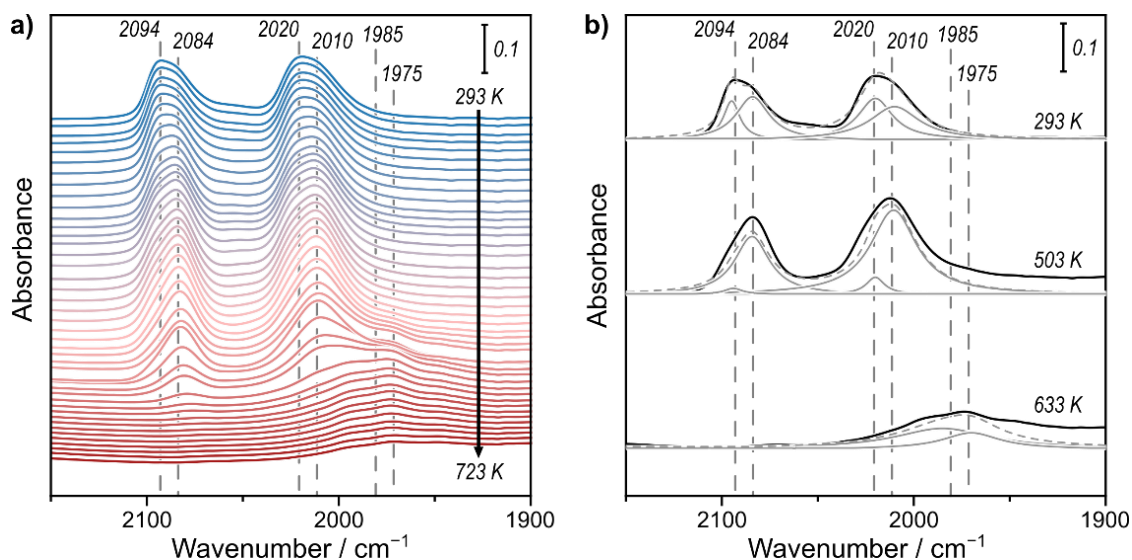
Figure 4. (a) IR spectra taken of 0.1 wt. % Rh/γ-Al$_2$O$_3$ every 10 K after sample is fully saturated with CO, and as temperature increases 0.33 K s^{-1} (20 K min^{-1}) from 293 K (blue) to 723 K (red). (b) Deconvolution spectra from (a) at 293, 503, and 633 K. Deconvoluted peaks (solid gray lines) are shown at each noted wavelength (2094, 2084, 2020, 2010, 1985, and 1975 cm^{-1}) with their sum (dashed gray line) at each temperature.

Table 1. Vibrational frequencies and full width at half maximum (FWHM) parameters for deconvoluted FTIR stretches associated with CO bound to atomically dispersed Rh$_1$/γ-Al$_2$O$_3$.

Species	Temperature range / K[a]	Wavenumber / cm^{-1}	FWHM / cm^{-1}
Rh(CO)$_2$	293–493 K	2094/2020	11/12
	493–603 K	2084/2010	22/29
Rh(CO)	> 603 K	1985 and 1975	49 and 36

[a]The temperature range at which the species dominates the surface based on IR bands.

Interestingly, the disappearance of peaks at 2084 and 2010 cm^{-1} closely corresponds to the temperature of light-off of NO reduction by CO over atomically dispersed Rh sites (Figure 5). The coincidence of *CO desorption with reactivity light-off suggests that the NO-CO reaction on Rh (CO)$_2$ sites begins with the desorption of *CO and that desorption is a kinetically relevant step. This is in direct contrast to NO reduction over Rh nanoparticles, where the Rh particle surface is NO-saturated and *NO is consumed by dissociating during light-off (10 wt. % Rh/γ-Al$_2$O$_3$, 273–673 K, 0.5 kPa CO and 0.1 kPa NO).[29] This highlights

the first mechanistic distinction between NO reduction by CO on Rh nanoparticles and by single atoms: the most abundant Rh species involves a different adsorbate.
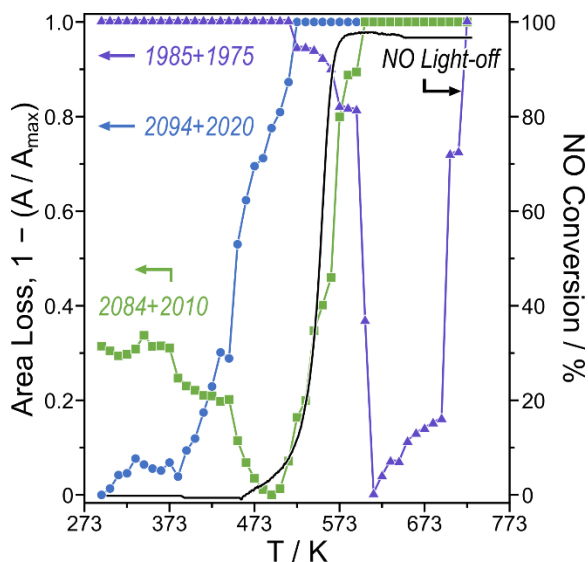
Figure 5. The total peak area loss for the sum peaks associated with the 2094 and 2020 cm^{-1} peaks (blue, ●), 2084 and 2010 cm^{-1} peaks (green, ■), and 1985 and 1975 cm^{-1} peaks (purple, ▲) normalized by the maximum sum of absorbance (A$_{max}$) as a function of temperature during TPD overlaid with NO conversion (%, black line) as a function of temperature at a ramp rate of 0.083 K s^{-1} in 0.5 kPa of CO and 0.1 kPa of NO over 200 mg of diluted 0.1% Rh/γ-Al$_2$O$_3$ catalyst (0.2 mg Rh).

The activation energy of desorption for each *CO on Rh in the experimental system was estimated using Redhead analysis[37] based on the temperature of maximum desorption (Table 2). The 2094/2020 cm^{-1} peaks associated with one type of Rh(CO)$_2$ species disappear at 493 K while the 2084/2010 cm^{-1} peaks grow, indicating that the 2094/2020 cm^{-1} species reconstructs to form the second species rather than desorbing. Therefore, the CO desorption energy for the 2094/2020 cm^{-1} Rh(CO)$_2$ species cannot be computed from the TPD. Furthermore, our prior work found that the desorption of *CO from Rh(CO)$_2$ had an entropic barrier, altering the appropriate rate constant for the pre-exponential factor using in Redhead analysis,[39] justifying here the use of two pre-exponential factors—6×10^{11} s^{-1} (yielding an upper limit for the adsorption energy) and the canonical 10^{13}—to calculate a range of possible *CO binding energies from Eq. 2. Thermal gradients in the bed up to 20 K are assumed for the lower

19

(weaker) bound of binding energies. The 2084/2010 cm^{-1} peaks reach maximum rate of change at 573 K, from which the desorption energy for the first *CO molecule from Rh(CO)$_2$ can be estimated as 143–161 kJ mol^{-1}, varying with the different possible pre-exponential factors and temperature gradients in the bed. The peaks associated with Rh(CO) species at 1985 cm^{-1} and 1975 cm^{-1} grow as the 2084/2010 cm^{-1} peaks disappear, then reach their maximum rate of desorption at 703 K, yielding a desorption energy of 193–199 kJ mol^{-1} for the second CO. These values can be compared with DFT predicted binding energies to validate a model for Rh(CO)$_2$, although as discussed later the direct desorption of CO from Rh(CO) may more likely involve ligand replacement steps from species bound to γ-Al$_2$O$_3$.

**Table 2.** Desorption energy and enthalpy (ΔH) values for *CO bound to atomically dispersed Rh on γ-Al$_2$O$_3$.

Adsorbate	Peak desorption temperature, T_P / K	Desorption energy, E / kJ mol^{-1}	Desorption enthalpy, ΔH / kJ mol^{-1}
CO from Rh(CO)$_2$	573	143[b]–161[a]	139[b]–157[a]
CO from Rh(CO)	703	193[b]–199	187[b]–193
Difference		32–56	30–54

[a] Upper limit of the *CO binding energy calculated using preexponential factor (A) of 6×10^{11} s^{-1} to account for the entropic barrier of desorption from Rh(CO)$_2$.
[b] Lower limit of *CO binding energy on Rh(CO)$_2$ and 1st order single molecule desorption was calculated with preexponential factor (A) of 10^{13} s^{-1} and peak desorption temperature 20 K less than the measured value to account for thermal gradients.

Given the density of *OH on γ-Al$_2$O$_3$ (8–12 *OH nm^{-2} on average between 300–400 °C), we investigated the effects of altering *OH environments on Rh(CO)$_2$ behavior. Exposing 0.1 wt. % Rh/γ-Al$_2$O$_3$ first saturated with CO to an Ar feed saturated with H$_2$O at 293 K increases the surface *OH coverage on γ-Al$_2$O$_3$. This increase in *OH coverage is evidenced by the loss of free *OH groups (> 3650 cm^{-1})[42,63,79] and growth of the broad hydrogen bonding *OH band from 3600–2500 cm^{-1},[42,55] indicating the formation of *OH-dense regions on the γ-

Al$_2$O$_3$ (Figure 6c). The growth of the H–O–H bending band at 1650 cm^{-1} also indicates the presence of molecularly adsorbed water (Figure 6a).[55] Water exposure noticeably tightens the bands associated with Rh(CO)$_2$ (~8 cm^{-1} reduction of FWHM) around centers at 2087/2013 cm^{-1} as *OH density increased (Figure 6b and Figure 7b), thus causing the peak centers to decrease. The reduction of the FWHM is likely because physisorbed water molecules near Rh sites homogenize the local coordination environment, indicating that the lower frequency Rh(CO)$_2$ species with peaks near 2087 and 2013 cm^{-1} formed during H$_2$O exposure exist in a highly hydrated environment. This is consistent with a seminal study of CO adsorption on Rh/Al$_2$O$_3$, in which water exposure shifted Rh(CO)$_2$ bands to lower frequency.[27]
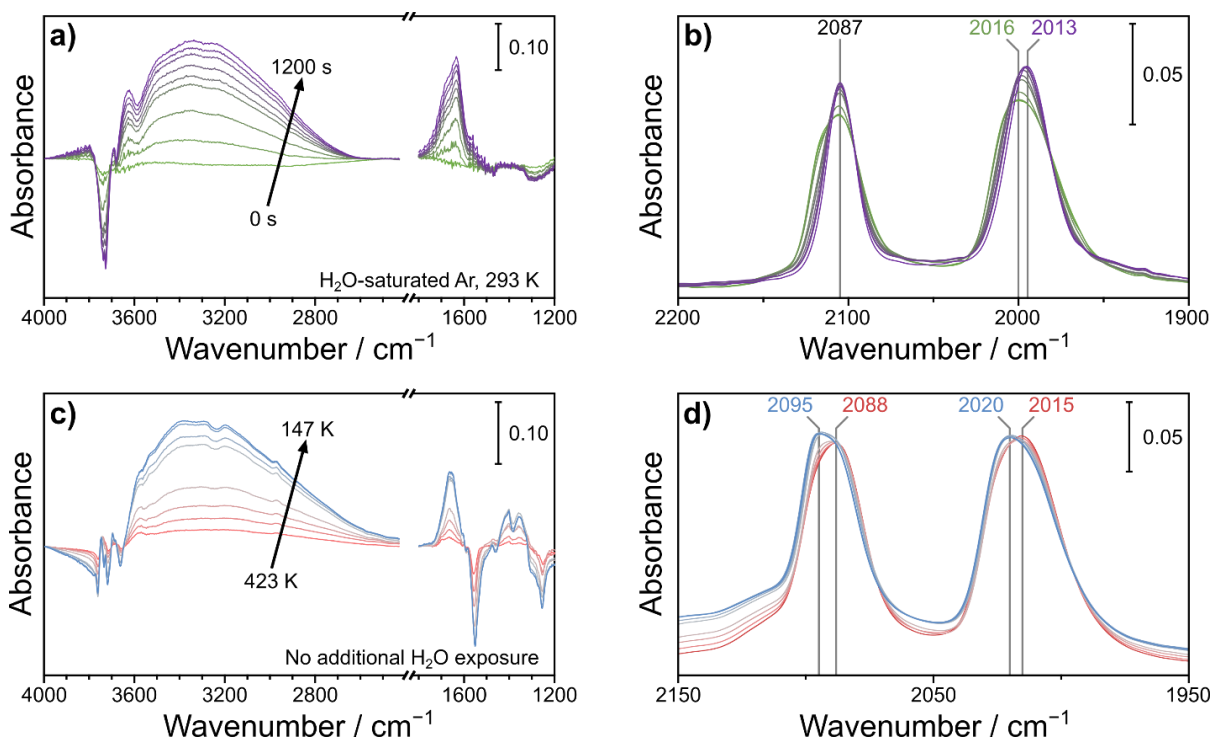
Figure 6. FTIR spectra of 0.1 wt. % Rh/γ-Al$_2$O$_3$ (a–b) saturated with CO at 298 K and exposed to a water-saturated Ar stream at 298 K for 1200 s and (c–d) saturated with CO at 423 K and cooled to 147 K, highlighting the O–H stretch and H–O–H bending regions in (a) and (c) and the Rh(CO)$_2$ stretch region in (b) and (d).
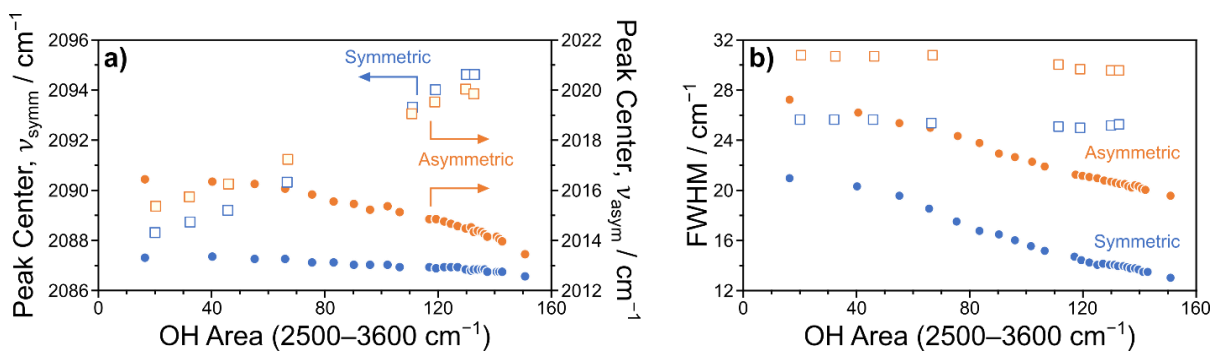
Figure 7. The (a) peak center and (b) FWHM of $Rh(CO)_2$ peaks as the area of the hydrogen bonding *OH band changes for symmetric (blue) and asymmetric (orange) stretches in samples brought to cryogenic temperatures (■, hollow) and exposed to H_2O at 298 K (●, filled).

Separately, 0.1 wt. % $Rh/\gamma\text{-}Al_2O_3$ was exposed to 10 kPa CO at 423 K to form $Rh(CO)_2$ and cooled to 147 K (Figure 6c–d). The $Rh(CO)_2$ bands initially appear similar in shape and position after CO adsorption to those at 423 K during TPD, but cooling to 147 K induces a shift in maximum intensity from 2088/2015 to 2095/2020 cm^{-1} for the $Rh(CO)_2$ peaks—the reverse effect of heating during TPD, indicating that the conversion between $Rh(CO)_2$ species observed during TPD prior to desorption is reversible. During cooling, the hydrogen bonding *OH region (integrated area between 3600–2500 cm^{-1}) and the H–O–H bending peak (1650 cm^{-1}) grow, indicating that trace water in the Ar feed molecularly adsorbs on the $\gamma\text{-}Al_2O_3$ during cooling. H_2O adsorption does not cause a substantial loss of free *OH groups (3800–3650 cm^{-1}), contrary to water exposure at room temperature, which presumably consumes most free *OH by condensing water on the surface. Assuming that molecular water exists only in *OH-saturated areas of $\gamma\text{-}Al_2O_3$, the persistence of free *OH during cooling suggests that some areas of the surface are saturated with *OH while others remain drier (and contain free, rather than hydrogen bonded, *OH). This could be due to either gaseous H_2O directly interacting with *OH or clustering of *OH or *H_2O on the surface. Despite increasing absorbance in the *OH region, the FWHM of the *CO features in $Rh(CO)_2$ do not tighten and the positions of maximum intensity of the *CO stretches shift to higher frequency during

cooling (Figure 7). This can be explained by OH–OH interactions on the support: at low temperature, densely packed *OH form ice-like layers on γ-Al$_2$O$_3$ from which Rh(CO)$_2$ is excluded by the strengthening hydrogen bonding networks. Whether this exclusion occurs by Rh(CO)$_2$ migration out of dense *OH regions or by *OH agglomeration away from Rh(CO)$_2$ is unclear. Regardless, these results suggest that *OH coverage alters *CO frequency in Rh(CO)$_2$ species and that the effects are moderated by temperature, which control interactions between *OH species.

Our collaborators at the University of Florida (Alex Hoffman and David Hibbitts) performed DFT calculations to explore the effects of *OH and *H$_2$O coverage on Rh(CO)$_2$ on the γ-Al$_2$O$_3$ surface derived from the (010) facet of dehydrated boehmite, while also considering effects of Rh oxidation state, additional ligands bounds to Rh, and γ-Al$_2$O$_3$ surface facet. First, they confirm that Rh is likely in a +1 state for Rh(CO)$_2$ species and that it is likely directly coordinated to an *OH group, as previous studies[17,18,67,80,81] have found. DFT also predicts that additional *OH species near Rh(CO)$_2$ on γ-Al$_2$O$_3$ also have an effect—increasing local *OH coverage around HO–Rh(CO)$_2$ can increase *CO frequencies by ~7 cm^{-1} from 2080/2015 cm^{-1} at 0 *OH nm^{-2} to 2086/2020 cm^{-1} at 6.79 *OH nm^{-2}, after which they significantly decrease to as low as 2071/1989 cm^{-1} at 7.92 *OH nm^{-2} and 10.18 *H$_2$O nm^{-2} (additional adsorbed molecular *H$_2$O in addition to *OH species) (Figure 8). The redshift occurring at higher *OH and *H$_2$O coverages (closer to expected average coverages of 8–12 *OH nm^{-2}) is consistent with the tightening of Rh(CO)$_2$ bands at lower frequency observed in our studies during water exposure and the 10 cm^{-1} redshift in Rh(CO)$_2$ frequency which occurs during TPD. The facet supporting HO–Rh(CO)$_2$ also affects *CO frequency, both directly through Rh-support interactions and indirectly by equilibrium *OH coverage. For instance,

HO–Rh(CO)$_2$ on dehydrated (001)$_b$ has frequencies of 2090 and 2020 cm^{-1}, and the (001)$_b$ facet retains fewer *OH than the (010)$_b$ or (100)$_b$ facets.[51,52] The facet dependence of *OH coverage and the likeliness of associative OH–OH interactions may lead to distinct patches of high and low *OH coverage on γ-Al$_2$O$_3$, rather than a continuous distribution, which could account for the appearance of the two distinct sets of Rh(CO)$_2$ bands observed in deconvolution of FTIR spectra.
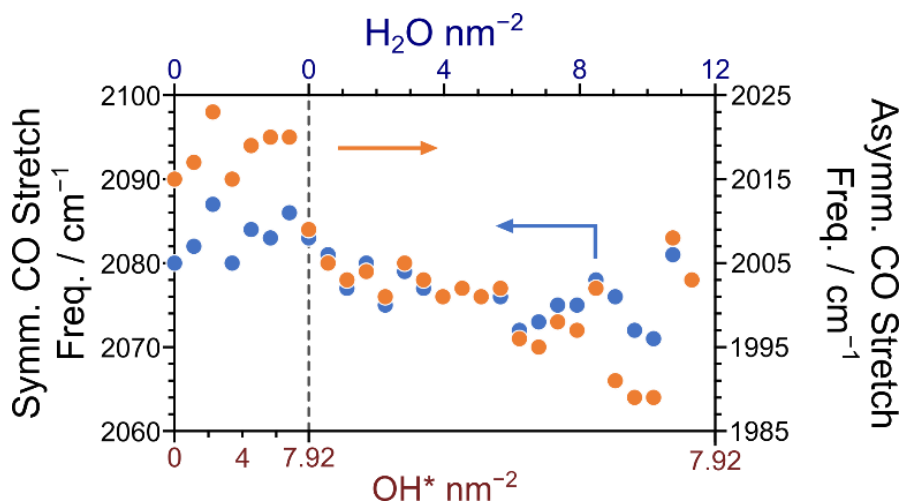

Figure 8. DFT predicted changes in the symmetric (blue) and asymmetric (orange) stretches of the Rh(CO)$_2$ with different surface concentrations of H*/OH* pairs and of molecular H$_2$O on γ-Al$_2$O$_3$(010)$_b$. The coverages within which H$_2$O adsorbs dissociatively to form H/OH pairs (in *OH nm^{-2}) and molecularly (in *H$_2$O nm^{-2}) are labeled along the bottom and top ordinate, respectively.

DFT also predicts that *OH density affects the adsorption/desorption characteristics of CO from Rh(CO)$_2$. The second *CO binding enthalpy ($\Delta H_{CO,2}$, enthalpy of binding the second *CO that forms Rh(CO)$_2$) weakens from -167 to -116 kJ mol^{-1} as the coverage of *OH and molecular *H$_2$O increase (Figure 9), suggesting that *CO desorption from HO–Rh(CO)$_2$ occurs more readily in high *OH coverage environments rather than low. When the second *CO adsorbs to form Rh(CO)$_2$, the additional *OH groups on γ-Al$_2$O$_3$ both stabilize the preceding state (Rh(CO)) and repel the additional *CO on the now saturated Rh; as such, binding energies for the second *CO weaken with additional *OH on the surface. This is

consistent with the hypothesis that the desorption of *CO from $Rh(CO)_2$ to form $Rh(CO)$ occurs from areas on γ-Al_2O_3 with higher hydroxyl coverage. The absolute value of the second *CO binding enthalpy, $\Delta H_{CO,2}$, from DFT of 116–167 kJ mol^{-1} captures the experimental range of 139–157 kJ mol^{-1} obtained from Redhead analysis. Consistency between trends in the CO frequency with *OH and *H_2O coverage, as well as the second *CO binding enthalpy suggest that the DFT calculations reasonably capture the salient features of the $Rh(CO)_2$ species observed in experiments and the desorption of the second *CO from $Rh(CO)_2$ to form $Rh(CO)$.

Alternatively, DFT predicts that increasing *OH and *H_2O coverage on γ-Al_2O_3 strengthens binding for the first *CO (to form $Rh(CO)$ from Rh) with $\Delta H_{CO,1}$ strengthening from -260 kJ mol^{-1} to -288 kJ mol^{-1} over the same range of *OH and *H_2O coverage considered for the loss of *CO from $Rh(CO)_2$. The additional *OH can coordinate to Rh without altering its oxidation state, which confers some additional stability when Rh has only one *CO ligand. However, the absolute value of the first *CO binding enthalpy from DFT of 260–288 kJ mol^{-1} is much higher than the experimental value of 187–193 kJ mol^{-1}. *CO desorption from $Rh(CO)$ to form a "bare" Rh in an unchanged oxidation state, as modeled here, is unlikely to occur in experiments, leading to doubts in DFT-derived binding energies of the first CO. Instead, it is likely that as *CO desorbs, new ligands (water- or surface-derived) take its place on the resulting Rh species. This process likely alters the Rh oxidation state and will stabilize the product of *CO desorption leading to a less exothermic desorption process. While IR spectroscopy is silent on the nature of the CO-less Rh complex, recent XAS has demonstrated that *CO desorption does indeed involve Rh coordination of additional oxygen species and likely the oxidation of Rh to the +3 state.[82]
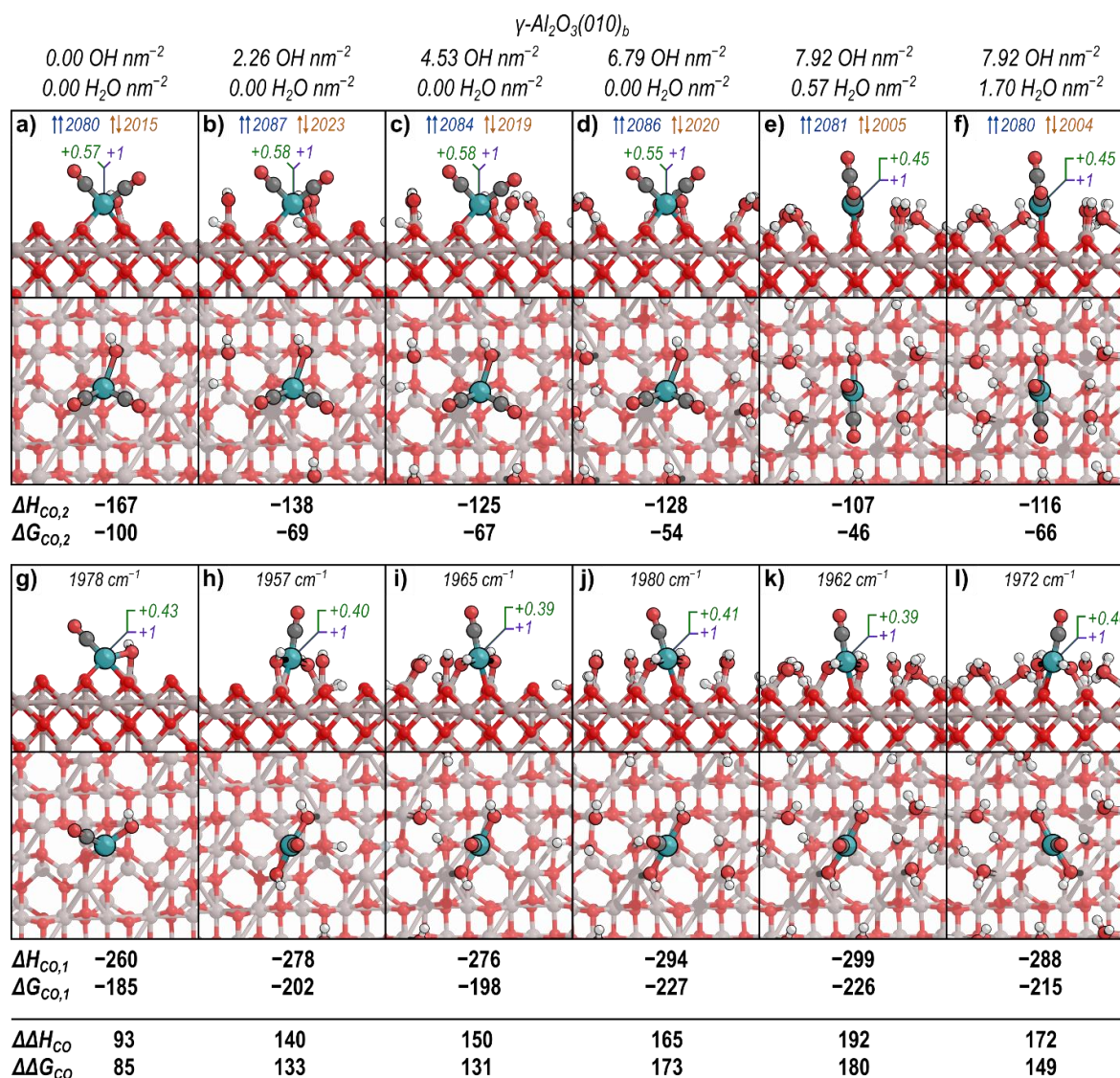
Figure 9. Models of (a–f) HO–Rh₁(CO)₂ and (g–l) HO–Rh₁(CO) on γ-Al₂O₃(010)ᵦ with adsorbed H₂O coverages of (a,g) 0.0 *OH nm⁻², (b,h) 2.26 *OH nm⁻², (c,i) 4.53 *OH nm⁻², (d,j) 6.79 *OH nm⁻², (e,k) 7.92 *OH nm⁻² and 0.57 *H₂O nm⁻² (where H₂O first adsorbs molecularly), and (f,l) 7.92 *OH nm⁻² and 1.70 *H₂O nm⁻² from additional H₂O dissociated on the γ-Al₂O₃ surface. For each structure, the *CO vibrational frequencies are shown in cm⁻¹, including symmetric (blue, ↑↑), asymmetric (orange, ↑↓), and monocarbonyl (black) stretches where appropriate. The assigned formal Rh oxidation state (purple) and partial charges from QUAMBO analysis (green) are also shown in *e*. Binding enthalpies (Δ*H*_CO) and free energies (Δ*G*_CO), as well as the differences for each between the first and second *CO (ΔΔ*H*_CO and ΔΔ*G*_CO) at 473 K are shown in kJ mol⁻¹ below their corresponding structures.

Taken together, the combination of experimental and theoretical data support the expected result that Rh(CO)₂ is in the +1 state, coordinated to *OH species native to γ-Al₂O₃,

and present on γ-Al_2O_3 surfaces in areas of varying *OH coverage. At ambient conditions, the HO–$Rh(CO)_2$ exist in heterogeneous areas of the support that contain a range of *OH coverages leading to broad *CO bands, and as temperature increases these HO–$Rh(CO)_2$ species migrate to more hydroxylated regions of γ-Al_2O_3 (conversion of 2094/2020 cm^{-1} bands to 2084/2010 cm^{-1} bands). Sequential *CO desorption then occurs from these HO–$Rh(CO)_2$ species in high hydroxyl coverage regions to form a $Rh(CO)$ species with a *CO band in the range 1985–1975 cm^{-1}. This process is depicted in Figure 10 below. It is thus proposed that the formed $Rh(CO)$ species in high hydroxyl coverage regions are likely active site models for the NO-CO reaction.

$Rh(CO)_2$

γ-Al_2O_3

Dense Surface OH Promote CO Desorption & Rh(CO) Formation
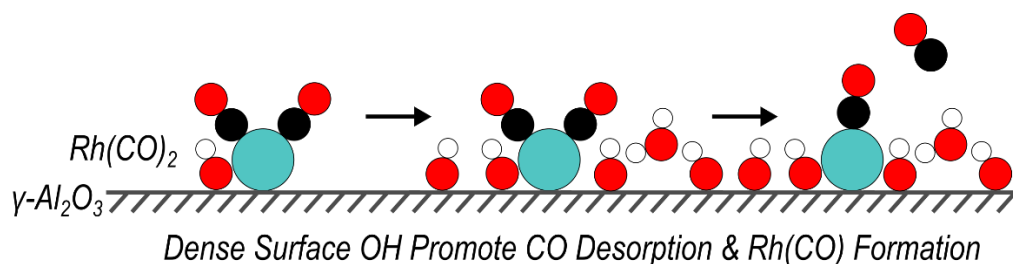
Figure 10. Schematic of $Rh(CO)_2$ behavior during temperature programmed desorption, in which $Rh(CO)_2$ translates on the γ-Al_2O_3 surface into *OH dense regions. These *OH promote *CO desorption and stabilize the Rh monocarbonyl. (Rh = blue, C = black, O = red, H = white).

## 4. Identification of a Reactive Intermediate in the NO-CO Reaction

The correspondence between light-off of NO reduction by CO and *CO desorption from $Rh(CO)_2$ during TPD suggests that *CO desorption is a required slow step of NO reduction under dry conditions. *In situ* IR of 0.1 wt.% $Rh/\gamma-Al_2O_3$ (0.5 kPa CO, 0.1 kPa NO, balance Ar, 205 °C) confirms that Rh sites are exist predominantly as $Rh(CO)_2$ at reaction conditions just prior to light-off (Figure 2). Therefore, an initial assumption of the mechanism that follows *CO desorption may be that NO adsorbs to the unsaturated Rh(CO) species, and a sequence of fast reactions take place between NO, CO, and derivatives thereof to yield the products N_2O, N_2, and CO_2. The lack of other observable Rh species in IR suggests that the steps following *CO desorption are faster than *CO desorption itself which generates potential $Rh–(NO)_x–CO$ intermediates, so identification of the relevant intermediate(s) cannot be performed *in situ,* as its concentration is exceedingly low.

The proposed $Rh–(NO)_x–CO$ species presumably form upon interaction of NO with unsaturated Rh(CO), so a model process of intermediate formation must produce this Rh species and make it available for NO adsorption. This requires that the atomically dispersed $Rh/\gamma-Al_2O_3$ catalyst be exposed to CO, which will produce $Rh(CO)_2$ under most conditions. The model process must also proceed at low enough temperatures to stabilize potential intermediate species, which are apparently highly reactive at temperatures near 200 °C—this eliminates thermal desorption of *CO for producing Rh(CO) to generate a $Rh–(NO)_x–CO$ intermediate. Instead, we turn to a photolytic mechanism under recent development in our group[82] which induces *CO desorption from $Rh(CO)_2$ to produce Rh(CO) at cryogenic temperatures, based on previous photolysis studies of heterogeneous $Rh(CO)_2$ supported on alumina[40,41] and of homogeneous metal carbonyl complexes.[83,84] Photolysis at cryogenic

conditions allows stabilization and spectroscopic characterization of the highly reactive Rh(CO) intermediate. Previous work has demonstrated that photolysis of Rh(CO)$_2$ could be achieved with ultraviolet light (> 2.8 eV) to generate a highly active Rh(CO) species that could activate stable molecules such as CO_2, O_2, and N_2.[41] This makes photolysis of the Rh–CO bond in Rh(CO)$_2$ an attractive alternative to thermally induced *CO desorption for the formation and study of potential reaction intermediates at low temperatures.

The photolysis of Rh(CO)$_2$ in 0.1 wt.% Rh/γ-Al$_2$O$_3$ was first performed in flowing Ar under vacuum at –120 °C using 370 nm light (intensity is estimated to be less than 20 mW cm^{-2} based on measurements taken at the window of the DRIFTS cell) and monitored with *in-situ* FTIR. First, the catalyst is treated in O$_2$ at 350 °C for 30 minutes, reduced in 10% H$_2$ at 190 °C for 1 hour, then cooled in Ar to –120 °C under vacuum. A background spectrum is taken at –120 °C, then the catalyst is heated in 5000 ppm CO to 150 °C and held for 30 minutes to generate Rh(CO)$_2$. It is then cooled in Ar back to –120 °C, at which point photolysis is performed. This leads to a decrease in the IR bands associated with Rh(CO)$_2$ at 2095 and 2019 cm^{-1} and the formation of a shoulder near 1975 cm^{-1} corresponding to Rh(CO) which is generated upon *CO desorption (Figure 11a). There is also likely a fraction of Rh(CO)$_2$ from which both *CO ligands are lost. The continued absence of features near 2060 cm^{-1} or 1850 cm^{-1}, which would correspond to linear and bridge bound *CO on Rh particles,[5,27] respectively, suggests that photolysis did not induce Rh agglomeration, though this cannot be ruled out if *CO desorbs as part of the agglomeration process. Detailed analysis in a separate study[82] suggest that photolysis of Rh(CO)$_2$ to generate Rh(CO) occurs primarily and most rapidly when Rh(CO)$_2$ exists in more hydroxylated areas of the support. This is consistent with inferences here on the mechanism of thermal desorption of *CO from Rh(CO)$_2$, further

29

motivating the use of cryogenic photolysis to generate reactive intermediates that are relevant to the thermal reaction mechanism at higher temperatures.
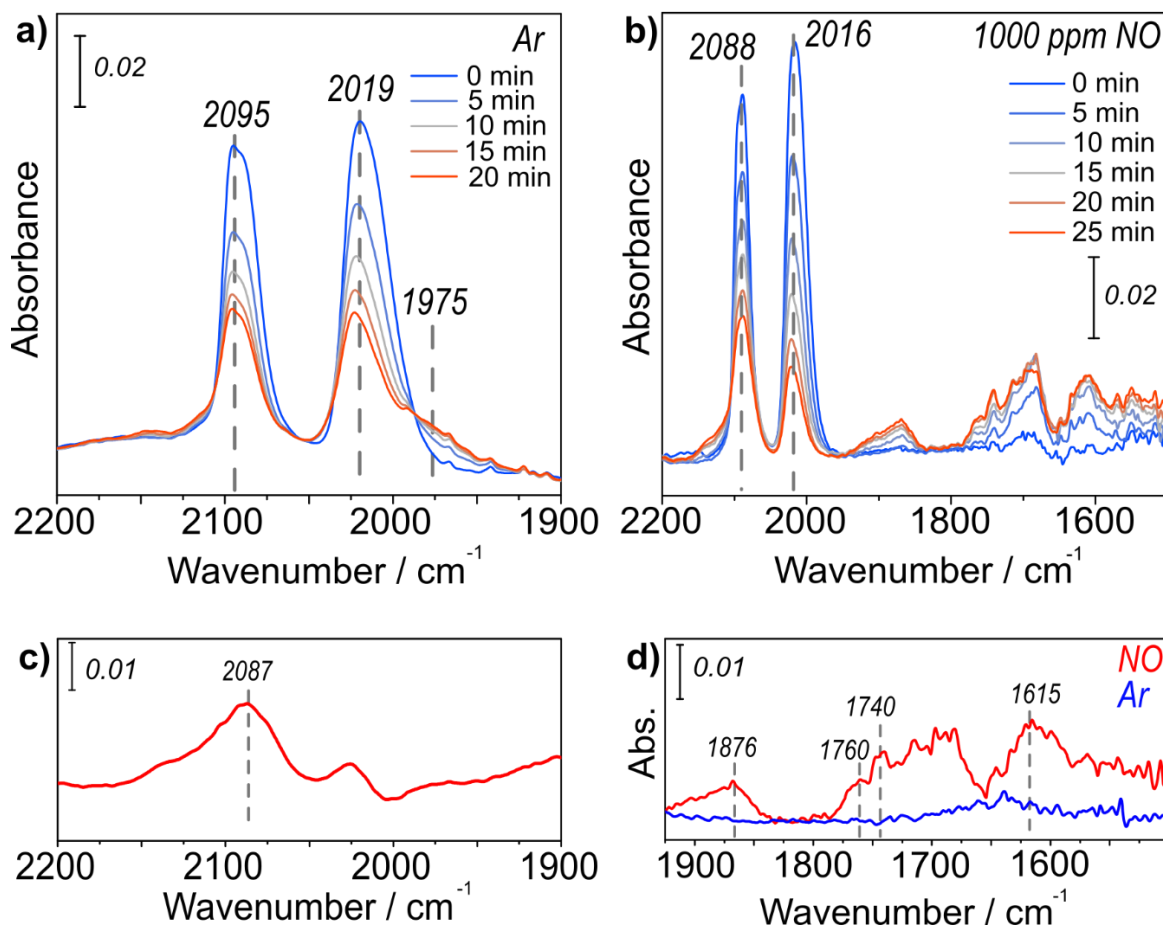

Figure 11. IR spectra of photolysis of $Rh(CO)_2$ in 0.1 wt.% Rh/γ-Al_2O_3 in (a) flowing Ar or (b) flowing 1000 ppm NO under vacuum at $-120\ °C$ using 370 nm light. Panel (c) shows the difference spectrum between spectra at 25 and 0 minutes in panel (b), scaled to minimize the size of $\nu_{CO,asym}$ at 2016 cm^{-1}. Panel (d) contains difference spectra (subtracted with common scale) from beginning to end of photolysis in Ar (blue) and NO (red).

The photolysis of $Rh(CO)_2$ was then performed at $-120\ °C$ in flowing NO (1000 ppm NO, balance Ar) to permit NO adsorption on the unsaturated $Rh(CO)$ species (Figure 11b). Photolysis in NO leads to substantial growth of multiple absorbance bands from 1500 to 1750 cm^{-1} and one at 1876 cm^{-1}, likely corresponding to multiple adsorbed *NO vibrations (Figure 11d). The peaks at 1876 and 1741/1760 cm^{-1} agree with features in IR spectra of 0.1 wt.% Rh/γ-Al_2O_3 exposed only to NO at $-120\ °C$ (Figure 12), suggesting NO adsorption occurred

on Rh atoms with no *CO ligands. New bands also appear between 1750 and 1650 cm^{-1} that do not correspond to IR in Figure 12, suggesting the formation of Rh–NO species distinct from those formed only by NO adsorption on Rh/γ-Al$_2$O$_3$. Absorbance between 1500 and 1650 cm^{-1} may be attributed to the formation of nitrate species on the support,[85–87] which will be further discussed in the context of the warming of these photolyzed systems.

Similar to photolysis in Ar, peaks corresponding to Rh(CO)$_2$ at 2088 and 2016 cm^{-1} decrease during photolysis in NO, but with different rates that causes the symmetric peak of the Rh(CO)$_2$ species to become larger than the asymmetric peak. This can be examined by subtracting spectra before and after photolysis and normalizing to the intensity of the asymmetric stretch, which reveals deviations in shape from the original Rh(CO)$_2$ bands (Figure 11c). From this difference spectrum, the shape change can be attributed to an increasing absorbance band between 2080–2090 cm^{-1}, which we attribute to the formation of a new *CO stretch. The exact position of the new feature is convoluted by the appearance of a shoulder at 2135 cm^{-1}, suggesting formation of oxidized Rh(CO).[17,88–90] The new *CO stretch (2080–2090 cm^{-1}) and *NO stretches between 1750 and 1650 cm^{-1} may be part of a mixed Rh–(NO)$_x$–CO species, which will be discussed in greater detail below. Importantly, Rh(CO)$_2$ is stable during exposure to 1000 ppm NO at –115 °C without photolysis (Figure 13), confirming that the loss of *CO and formation of Rh(CO) species that enable NO desorption at cryogenic temperature requires photolysis of Rh(CO)$_2$.
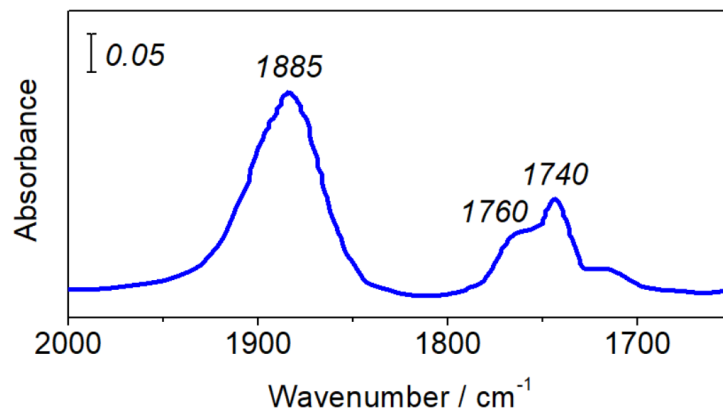
Figure 12. IR spectra of 0.1 wt.% Rh/γ-Al$_2$O$_3$ saturated with 1.5 % NO under vacuum at –120 °C.
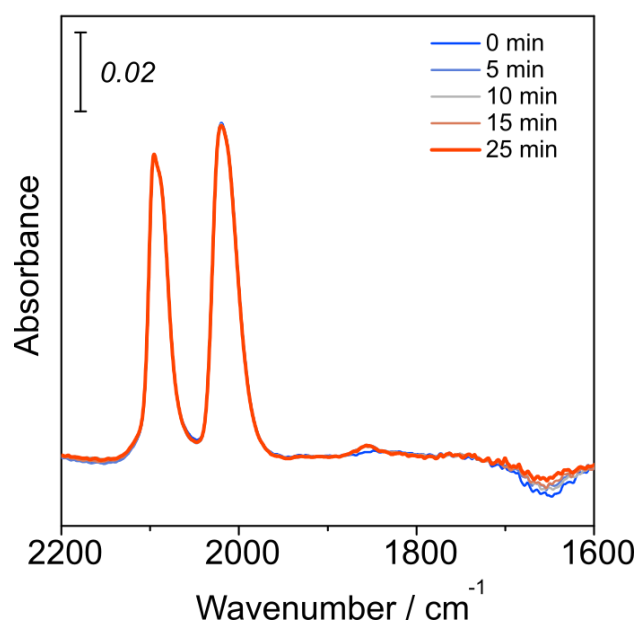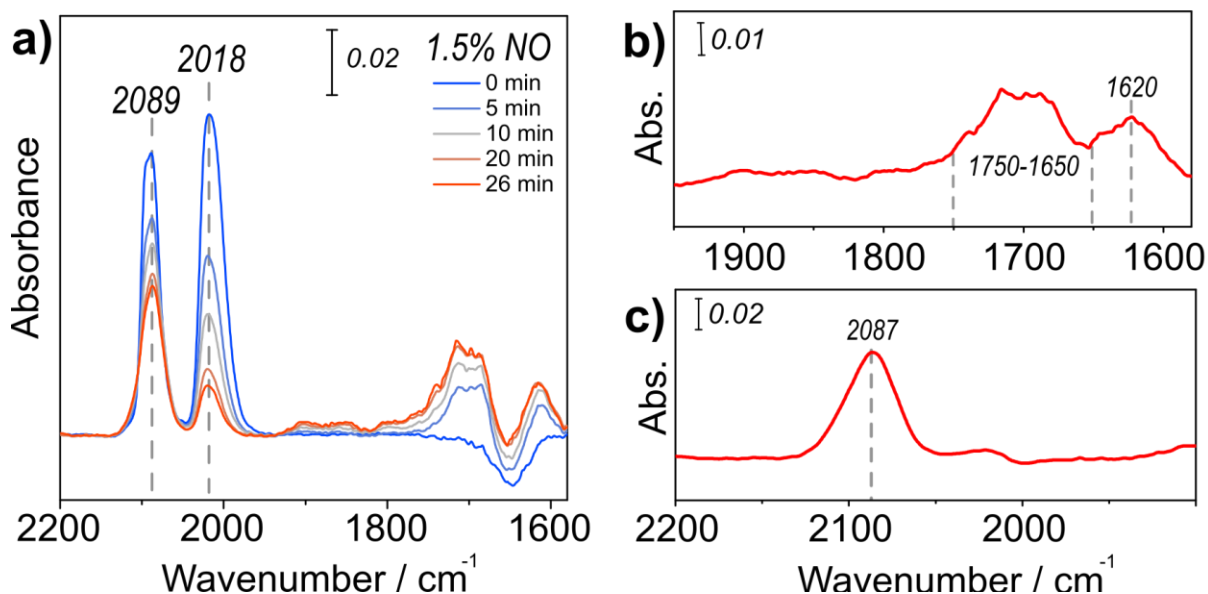

Figure 13. IR spectra of Rh(CO)$_2$ in 0.1 wt.% Rh/γ-Al$_2$O$_3$ during 25 minutes of exposure to 1000 ppm NO under vacuum at –115 °C. Spectra are nearly identical, so at most wavenumbers only the spectrum after 25 minutes (red) is visible.

Photolysis of Rh(CO)$_2$ was also performed in 1.5% NO to assess the effect of NO concentration. The CO region of the IR spectra in Figure 14a appears qualitatively identical to that in Figure 11b of photolysis in 1000 ppm NO. The negative peak in the initial Rh(CO)$_2$ spectrum centered at 1650 cm^{-1} suggests that there was water present in the background spectrum (taken at –120 °C) that desorbed during heating prior to CO adsorption at 150 °C.

32

With exposure to UV light and 1.5% NO, $Rh(CO)_2$ peaks at 2089 and 2018 cm^{-1} decrease in intensity as the symmetric stretch becomes relatively larger than the asymmetric stretch. The difference spectrum (normalized to the asymmetric stretch of $Rh(CO)_2$) reveals again the growth of the new *CO stretch near 2080–2090 cm^{-1}. After 26 minutes of photolysis in 1.5% NO, the ratio of the symmetric to asymmetric $Rh(CO)_2$ stretch is twice as large as that after photolysis in 1000 ppm NO, suggesting a higher yield of the species containing the new *CO stretch than from photolysis in 1000 ppm NO. Also notable is the diminished intensity of sharp *NO features at 1876 and 1741/1760 cm^{-1}, which correspond to Rh–NO species that do not contain CO, and the lack of changes to the spectra below 1600 cm^{-1}. Persistence of bands from 1750–1650 cm^{-1} is consistent with the notion that they are associated with $Rh–(NO)_x–CO$ species that also contain the *CO stretch between 2080–2090 cm^{-1}. Finally, no additional *NO stretches were observed during photolysis in 1.5% NO as compared to 1000 ppm NO, indicating that the higher NO concentration did not generate any additional species to those in 1000 ppm NO. Therefore, photolysis in 1.5% NO was performed for other tests without loss of comparability to the 1000 ppm NO photolysis system, which is more comparable to the representative TWC environment.

Figure 14. (a) IR spectra of photolysis of $Rh(CO)_2$ in 0.1 wt.% Rh/γ-Al_2O_3 in flowing 1.5% NO under vacuum at $-120\ °C$ using 370 nm light. Panel (b) shows the difference spectrum (subtracted with common scale) from beginning to end of photolysis. Panel (c) shows the difference spectrum between spectra at 26 and 0 minutes in panel (a), scaled to minimize the size of $\nu_{CO,asym}$ at 2016 cm^{-1}.

Our collaborators at the University of Florida, Alex Hoffman and David Hibbitts, performed DFT calculations to predict free energies of formation and frequencies of plausible Rh complexes that could form during photolysis of $Rh(CO)_2$ in NO environments. Upon NO adsorption onto Rh(CO) and Rh atoms at $-120\ °C$ and barring any reactions with ligands native to the support, $Rh(CO)(NO)_2$ and $Rh(NO)_3$ are the thermodynamically favorable configurations with free energies of -56 and -49 kJ mol^{-1} relative to $Rh(CO)_2$ at the same temperature (Figure 15). DFT calculated frequencies for $Rh(CO)(NO)_2$ are 2070, 1755, and 1645 cm^{-1} for the *CO and two *NO stretches, respectively (Table 3). Calculated frequencies for the *NO stretches of $Rh(NO)_3$ are 1768, 1720, 1635 cm^{-1}. These frequencies are in good agreement with the new *CO band that appears at 2080–2090 cm^{-1} during photolysis and the growth of multiple *NO absorption bands between 1600 and 1750 cm^{-1}. The corresponding frequencies and thermodynamic favorability of $Rh(CO)(NO)_2$ and $Rh(NO)_3$ suggest these species form during photolysis of $Rh(CO)_2$ in flowing NO, and we assign the *CO band at

34

$2080–2090 \text{ cm}^{-1}$ to the *CO stretch of $Rh(CO)(NO)_2$. Further details of these calculations will be provided in a future publication.
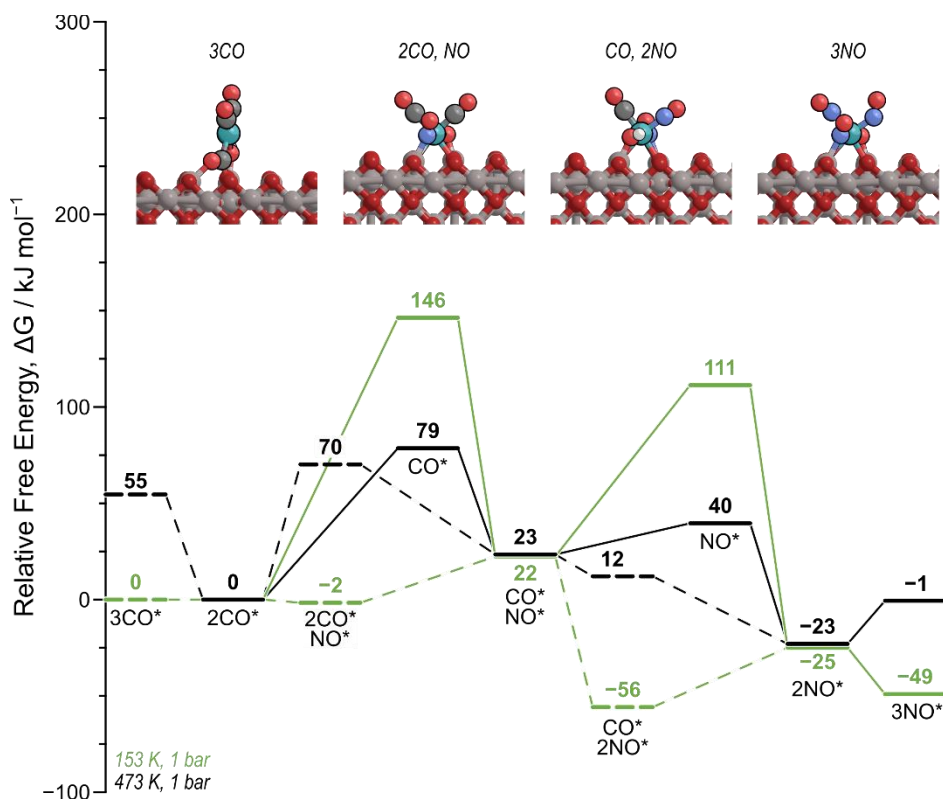
Figure 15. DFT predicted free energies of different Rh adsorbate structures relative to $Rh(CO)_2$ at 1 bar at 153 K (red) and 473 K (black). Adsorbates are listed next to the black curve. Structures were modeled as $HO–Rh(ads)$ on the $(010)_b$ facet of $\gamma\text{-}Al_2O_3$. Further details will be presented in a future publication.

Table 3. DFT predicted vibrational frequencies and free energies of formation of different Rh–adsorbate structures (each coordinated to OH) relative to $Rh(CO)_2$.

| Species | ΔG_f relative to $Rh(CO)_2$ / kJ mol^{-1} | | ν_{CO} / cm^{-1} | ν_{NO} / cm^{-1} |
	−120 °C, 1 bar	200 °C, 1 bar		
$Rh(CO)_2(NO)$	5	70	2103, 2043	1559
$Rh(CO)$	140	79	1978	—
$Rh(CO)(NO)$	23	23	2043	1655
$Rh(CO)(NO)_2$	−51	12	2070	1755, 1645
$Rh(NO)$	106	40	—	1844
$Rh(NO)_2$	−25	−23	—	1868, 1655
$Rh(NO)_3$	−49	−1	—	1726, 1671, 1643

The mixed $Rh(CO)(NO)_2$ is analogous to the $[RhCl_2(CO)(NO)_2]^-$ intermediate proposed in a previous study of NO reduction by CO over homogeneous $[RhCl_2(CO)_2]^-$ complexes.[23] Similar to the $Rh/\gamma-Al_2O_3$ system in which Rh–OH interactions are an important factor in *CO desorption during catalysis, researchers found that the presence of water and acid in the ethanol solvent accelerated the reaction rate five-fold. At NO:CO ratios of 4:3, they propose that $[RhCl_2(CO)(NO)_2]^-$ is the most abundant Rh intermediate (based on a color change and stoichiometric production of CO_2 and N_2O) and that consumption of this species is the rate limiting step. However, at low NO:CO ratios (which is relevant to our reaction conditions of 1:5 NO:CO), they found $[RhCl_2(CO)_2]^-$ to be most abundant (based on solution color) and its consumption to be limiting—similar to the *in situ* IR spectrum in this work which shows only the presence of the most abundant species, $Rh(CO)_2$.

Here, we demonstrate the use of UV photolysis to generate what could be the reactive intermediate of NO reduction by CO over atomically dispersed $Rh/\gamma-Al_2O_3$: $Rh(CO)(NO)_2$. This intermediate (or that containing dimerized NO, $Rh(CO)(N_2O_2)$) has been inferred in previous studies of analogous systems,[20,22,23] but not observed spectroscopically until now. The correspondence of IR spectra with DFT predicted structures supports our assignment of this species with IR peaks between 2080–2090 cm^{-1} and 1650–1750 cm^{-1}. *In situ* IR suggests that any reactive intermediates derived from $Rh(CO)_2$ readily react at elevated temperatures— therefore, photolytically generated $Rh(CO)(NO)_2$ should react as it warms from cryogenic to reaction temperature. We investigate this warming process for both photolyzed and unphotolyzed systems treated with NO at cryogenic temperatures to elucidate possible reaction pathways and any subsequent intermediates.

5. Interactions between Rh(CO)₂, NO and CO derived support species, and *OH

5.1. Behavior of Rh/γ-Al₂O₃ During Warming after Cryogenic NO Treatment

After either NO treatment of Rh(CO)₂ in the dark (Figure 13) or photolysis of Rh(CO)₂ in NO (Figure 11b–d) at –115 or –120 °C, respectively, the IR cell was purged with Ar under vacuum for at least 5 minutes and allowed to warm to ambient temperature in Ar. IR spectra during this warming process reveal an interesting phenomenon: all Rh–CO IR peaks (corresponding to either Rh(CO)₂ or Rh(CO)(NO)₂) disappear below –20 °C with the growth of features at 1870 cm⁻¹ and 1750 cm⁻¹, likely corresponding to Rh–NO species, and many features from 1620–1200 cm⁻¹ corresponding to NO and CO derived species on the support (Figure 16–Figure 20, further discussion below). Importantly, Rh(CO)₂ that was either photolyzed in Ar or held in Ar at cryogenic temperature (never exposed to NO) was stable during warming (Figure 19, further discussion below). While the reactive nature of photolytically generated Rh(CO)(NO)₂ species was expected, the reactivity of Rh(CO)₂ species exposed to NO in the dark was unexpected given the hypothesis of *CO desorption from Rh(CO)₂ being kinetically controlling.

To monitor the decay and growth of species in IR during warming, peak intensities were tracked for each species of interest in each spectrum and plotted against the temperature of the catalyst bed. The peaks of interest, their species assignments, and method of tracking are listed in Table 4. The Rh(CO)(NO)₂ species was tracked via the *CO stretch (ν_{CO}) due to significant overlap of *NO stretches from various species. The area of the *CO stretch of Rh(CO)(NO)₂ was computed by subtracting the area of the asymmetric stretch of Rh(CO)₂ from the area of the combined symmetric stretch and *CO stretch of Rh(CO)(NO)₂ in the initial

37

ratio of the symmetric to asymmetric stretch (~0.65), so as to estimate only the area corresponding to the *CO stretch of $Rh(CO)(NO)_2$ and not unphotolyzed $Rh(CO)_2$. Features from 1650–1300 cm^{-1} were tracked by the height of each peak relative to the absorbance at 1950 cm^{-1}, as a baseline. Area traces for all species should be considered qualitative at less than ~ 20 % fractional area due to changes in the baseline over the large temperature range in these experiments.

The warming process is broken into three phases: (I) Loss of $Rh(CO)(NO)_2$ (–120 to –75 °C), (II) Loss of $Rh(CO)_2$ and formation of Rh–NO at 1870 cm^{-1} (–75 to –50 °C), and (III) Formation of Rh–NO at 1750 cm^{-1} and NO and CO derived support species (–50 to –20 °C). Analysis focuses on comparing the behavior of photolyzed and unphotolyzed systems that were both exposed to 1000 ppm NO at low temperature.

Table 4. Features monitored during warming after low temperature experiments.

Frequency	Related Species	Region	Baseline	Ref.
~2015 cm^{-1}	$\nu_{CO,asym.}$ Of Rh(CO)$_2$	2050–1950 cm^{-1} (area)	2050–1950 cm^{-1}	5,12,27
~2085 cm^{-1}	ν_{CO} of Rh(CO)(NO)$_2$	(2120–2050 cm^{-1} area)–0.65*(2050–1950 cm^{-1} area)	2120–2050 cm^{-1}	This work
2343 cm^{-1}	CO$_2$	2350–2330 cm^{-1} (area)	2350–2330 cm^{-1}	91–93
2236 cm^{-1}	N$_2$O	2270–2200 cm^{-1} (area)	2270–2200 cm^{-1}	This work, 94
3740 cm^{-1}	Free surface *OH	3800–3715 cm^{-1} (area)	3800 cm^{-1}	42–44,63,64
1870 cm^{-1}	Rh–NO	1920–1830 cm^{-1} (area)	1920–1830 cm^{-1}	30,33,34
1750 cm^{-1}	Rh–(NO$^-$)	1790–1720 cm^{-1} (area)	1790–1720 cm^{-1}	30,33,34
1620 cm^{-1}	NO$_3^-$, COOH, representative of features at 1560 cm^{-1} and 1590 cm^{-1}	1620 cm^{-1} (height)	1950 cm^{-1}	85–87,93,95,96
1430 cm^{-1}	NO$_3^-$, hydrated NO$_3^-$, HCO$_3^-$	1430 cm^{-1} (height)	1950 cm^{-1}	85,91–93,96–98
1320 cm^{-1}	NO$_3^-$, hydrated NO$_3^-$, CO$_3^-$, COOH	1320 cm^{-1} (height)	1950 cm^{-1}	85,96,97,99
1230 cm^{-1}	NO$_2$, HCO$_3^-$	1280–1200 cm^{-1} (area)	1280–1200 cm^{-1}	85,86,91,93,96,98

In Phase I of warming from –120 to –75 °C, Rh(CO)(NO)$_2$ (only seen in experiments where Rh(CO)$_2$ was photolyzed in NO environments at cryogenic conditions) starts to decompose at –118 °C while peaks appear at 2343 and 2236 cm^{-1} (Figure 16a,c), with 5 % of Rh(CO)(NO)$_2$ lost when peaks at 2343 and 2236 cm^{-1} reach their maximum area. The feature at 2236 cm^{-1} matches the features of *N$_2$O on γ-Al$_2$O$_3$ at –120 °C (Figure 17). The feature at 2343 cm^{-1} is near the center of the gas phase CO$_2$ IR spectrum at 2349 cm^{-1}, but similar features have also been attributed to combination bands of nitrates.[86] However, a similar feature at 2343 cm^{-1} appears when warming Rh(CO)$_2$ that had not previously seen NO, though at –100 °C rather than –118 °C, and a small feature at 2277 cm^{-1} is present with ~0.75% of the area of the band at 2343 cm^{-1}, close to the natural abundance of ^{13}CO (1.1%). Both factors suggest that

the feature at 2343 cm^{-1} is indeed $*CO_2$ adsorbed on γ-Al_2O_3. The appearance of $*CO_2$ and $*N_2O$ with loss of $Rh(CO)(NO)_2$ is consistent with a reaction between the $*CO$ and two $*NO$ ligands, while appearance of $*CO_2$ during warming of $Rh(CO)_2$ that had not seen NO could be due to loss of a small fraction of reactive $Rh(CO)_2$. As this occurs, $*OH$ species near 3740 cm^{-1} are consumed—these $*OH$ are considered non-hydrogen bonding, reactive $*OH$ bound to Al support atoms.[42–44,63,64] In general, consumption of these $*OH$ occurs with decomposition of $Rh(CO)(NO)_2$ or $Rh(CO)_2$, suggesting that these decomposition processes involve reactions with $*OH$, consistent with our work demonstrating the importance of $*OH$ to $*CO$ desorption from $Rh(CO)_2$.
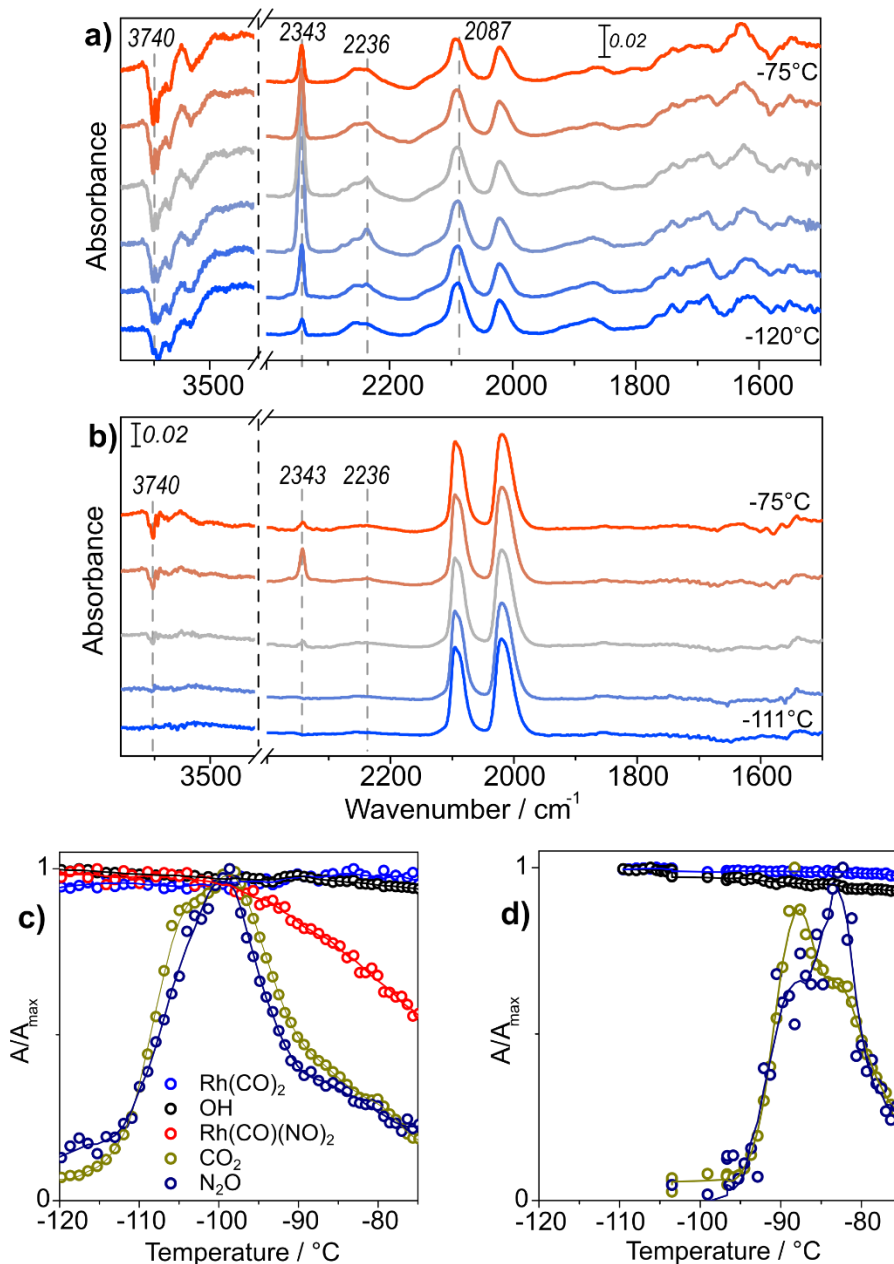
Figure 16. IR spectra of 0.1 wt.% Rh/γ-Al$_2$O$_3$ first saturated with CO to form Rh(CO)$_2$, then warmed from –120 to –75 °C after cryogenic (a) photolysis in 1000 ppm NO at –120 °C or (b) exposure to 1000 ppm NO for 25 minutes at –115 °C. Traces of Rh(CO)$_2$ (blue), free surface *OH (black), Rh(CO)(NO)$_2$ (red), CO$_2$ (navy), and N$_2$O (dark yellow) during warming after (c) photolysis and (d) cryogenic NO exposure. Lines in (c) and (d) are to guide the eye.

For the unphotolyzed Rh(CO)$_2$ species exposed to NO at –115 °C, no Rh(CO)$_2$ is lost nor is *CO$_2$ observed until –97 °C, at which point *OH at 3740 cm^{-1} start to be consumed. The maximum area of the *CO$_2$ peak is 35 % of that in the photolyzed sample. Interestingly,

41

a small amount of N_2O is formed at 2236 cm^{-1}, but only 17% of that in the photolyzed sample. This suggests that there could be some backspillover of *NO onto Rh sites as $Rh(CO)_2$ decomposes in the absence of photolysis. Further probe molecule IR of *CO_2 and *N_2O on the catalyst are needed to fully explain the behavior of these species during warming, but the correspondence of the appearance of *CO_2 with the onset of decomposition of either $Rh(CO)(NO)_2$ (photolyzed catalyst) or $Rh(CO)_2$ (unphotolyzed catalyst) suggests that the processes are connected.
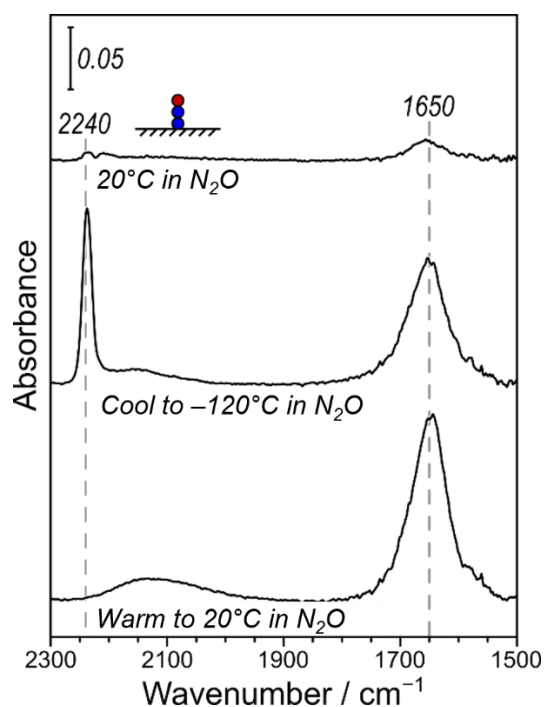
Figure 17. IR spectra of γ-Al_2O_3 exposed to 1000 ppm N_2O under vacuum. Catalyst was first exposed at 20 °C, then cooled to –120 °C, and warmed back to 20 °C.

From –120 to –75 °C, 45 % of $Rh(CO)(NO)_2$ formed during photolysis is lost, while 3 % of $Rh(CO)_2$ is in the unphotolyzed system is lost, demonstrating the significant reactivity of the $Rh(CO)(NO)_2$ intermediate. Phase II of warming from –75 to –50 °C marks the start of significant loss of $Rh(CO)_2$ from the unphotolyzed system that had been exposed to NO, while significant loss of remaining $Rh(CO)_2$ in the photolyzed material does not start until –62 °C

42

(Figure 18). After approximately 50% of $Rh(CO)_2$ is lost from the unphotolyzed sample, a Rh–NO stretch at 1870 cm^{-1} begins to form (starting at –57 °C), while in the photolyzed sample this occurs at a similar temperature to loss of remaining $Rh(CO)_2$. The formation of the 1870 cm^{-1} peak occurs in two steps for all samples. A maximum is reached between –55 and –50 °C as a feature at 1230 cm^{-1} also appears and reaches a maximum. After this, the area of the 1870 cm^{-1} peak decreases until new features at 3620, 1620, 1590, 1560 cm^{-1} (peaks at 1590 and 1560 cm^{-1} behave similarly to 1620 cm^{-1}) and a series of broad bands between 1500–1300 cm^{-1} begin to form and the area of the 1870 cm^{-1} peak grows to a second maximum. Another Rh–NO feature at 1750 cm^{-1} grows during this time as well, with only a single maximum near the temperature of the second maximum of the peak at 1870 cm^{-1}. The development of the 1320 cm^{-1} feature by –50 °C in the photolyzed sample occurs at the start of the next phase of warming in the unphotolyzed sample. The feature at 1560 cm^{-1} is more pronounced in the unphotolyzed sample, which could indicate that it originates from CO, since more *CO remained on the unphotolyzed material.
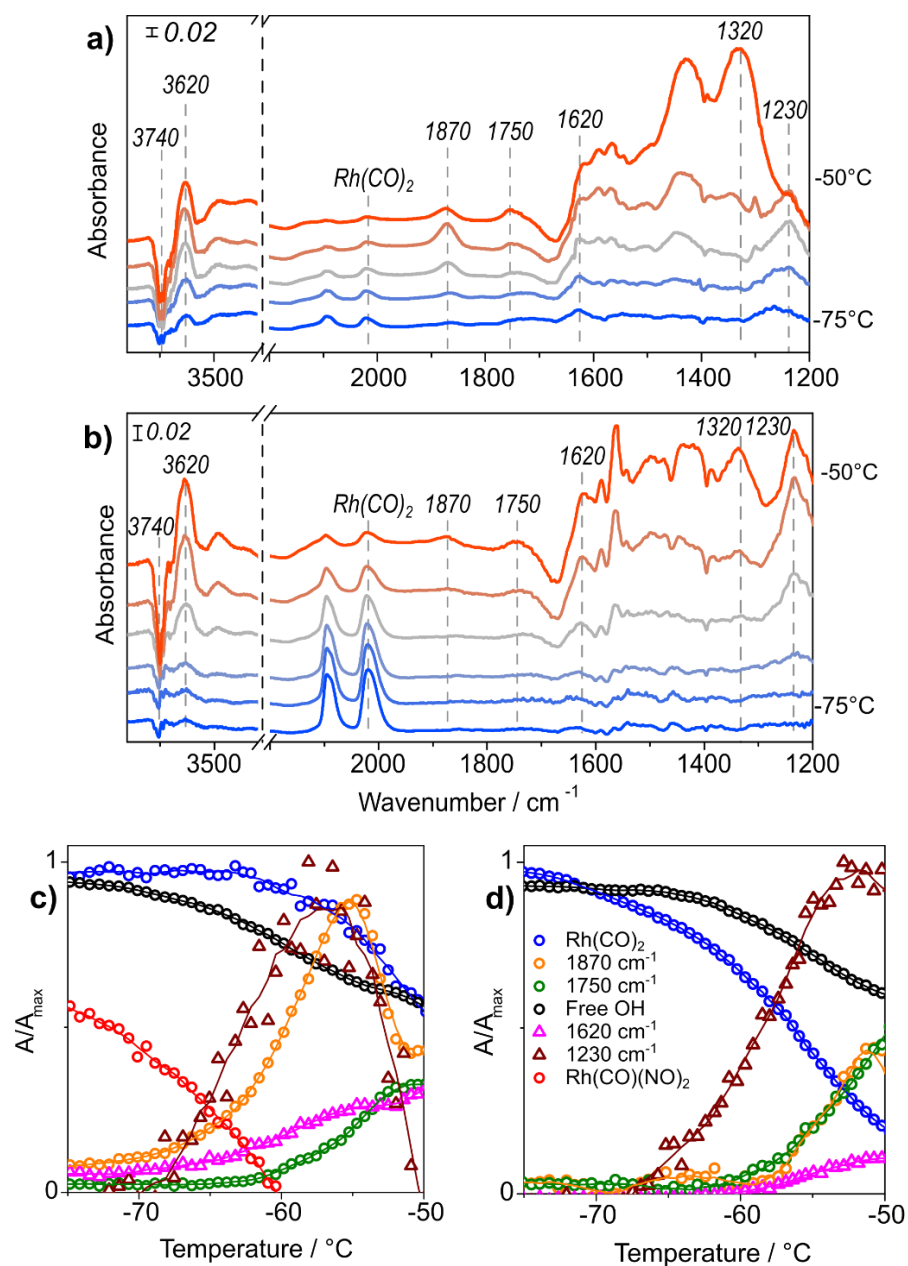
Figure 18. IR spectra of 0.1 wt.% Rh/γ-Al$_2$O$_3$ first saturated with CO to form Rh(CO)$_2$, (a) photolyzed at –120 °C in 1000 ppm NO or (b) exposed at –115 °C to 1000 ppm NO, during warming from –75 to –50 °C. Traces of Rh(CO)$_2$ (blue), free surface *OH (black), Rh(CO)(NO)$_2$ (red), Rh–NO at 1870 (orange) and 1750 cm^{-1} (green), and species at 1620 (pink) and 1230 cm^{-1} (dark red) during warming after (c) photolysis and (d) cryogenic NO exposure. Lines in (c) and (d) are to guide the eye.

The cause of the unexpected loss of Rh(CO)$_2$ in the unphotolyzed system exposed to NO is not obvious, as Rh(CO)$_2$ is typically stable in Ar or vacuum at temperatures below 200 °C. In control experiments in which Rh(CO)$_2$ is photolyzed in Ar at –120 °C or simply held in

Ar at –120 °C (the material is never exposed to NO), $Rh(CO)_2$ remains stable while warming to room temperature (Figure 19). In fact, $Rh(CO)_2$ appears to reform on the photolyzed catalyst with the loss of $Rh(CO)$ during warming, likely due to reverse spillover of CO-derived surface species onto Rh in a mechanism analogous to reverse spillover of *NO onto Rh sites in the NO experiments. It appears that NO treatment between –115 and –120 °C, even without photolysis, conferred reactivity to all $Rh(CO)_2$ in the material. In the absence of photolysis, NO treatment at –115 °C does not appear to alter the $Rh(CO)_2$ species at –120 °C (Figure 13), though it does lead to the appearance of a small feature at 1850 cm^{-1} which likely corresponds to the NO stretch of an NO-derived species. Increasing absorbance near 1650 cm^{-1} during NO exposure in the dark was also seen in a control experiment while holding the catalyst at –120 °C in Ar, so this likely corresponds to slow adsorption of trace water in the feed onto γ-Al_2O_3. Despite the small size of the feature at 1850 cm^{-1}, likely corresponding to an NO stretch, loss of $Rh(CO)_2$ in the unphotolyzed material during warming is still followed by growth of Rh–NO features at 1870 cm^{-1} and 1750 cm^{-1} and a similar mix of species between 1620 and 1200 cm^{-1}. It appears NO treatment at low temperature deposited significant amounts of *NO (or NO-derived species) on the surface that was barely visible in IR, yet later reactive with $Rh(CO)_2$.
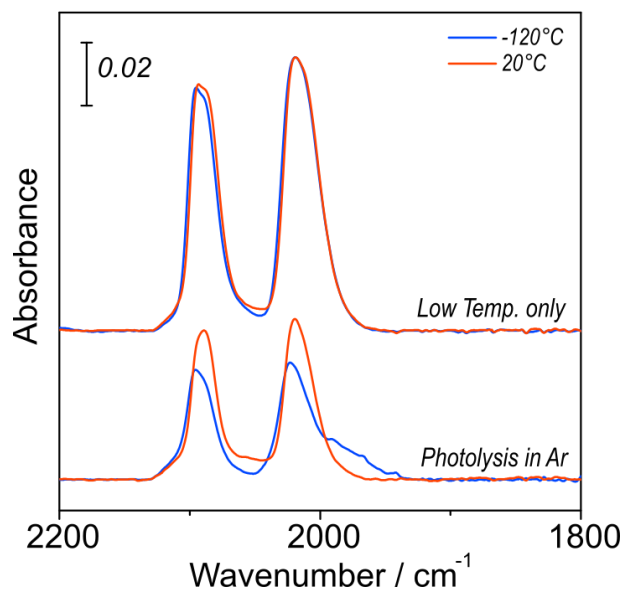
Figure 19. IR spectra of 0.1 wt.% Rh/γ-Al$_2$O$_3$ first saturated with CO to form Rh(CO)$_2$, after either (a) photolysis at –120 °C in Ar, followed by (b) warming to room temperature, or after (c) holding at –120 °C in Ar for 20 minutes, followed by (d) warming to room temperature.

During Phase III of warming (Figure 20), Rh–NO stretches at 1870 cm^{-1} and 1750 cm^{-1} are lost from –50 to –20 °C, though a small fraction of the feature at 1750 cm^{-1} remains at room temperature. Features from 1620 to 1560 cm^{-1} then decrease with broad growth centered at 1430 cm^{-1}. Previous studies of *NO$_2$ adsorption on alumina[85,86] have found that nitrate formation on the support begins first with the appearance of a feature at 1230 cm^{-1} (nitrite) followed by conversion to nitrate features between 1620 and 1500 cm^{-1}. This process is observed in both photolyzed and unphotolyzed materials exposed to NO as they warm from –70 to –45 °C, suggesting that nitrate species are building up on Al$_2$O$_3$. Loss of *OH at 3740 cm^{-1} is also met with new *OH stretches at 3620, 3480, and 3350 cm^{-1}. The lower O–H frequency suggests a weaker, more acidic O–H bond[42,64] likely formed by reaction with *NO to form acids such as HNO$_3$ or HONO.[85,86]
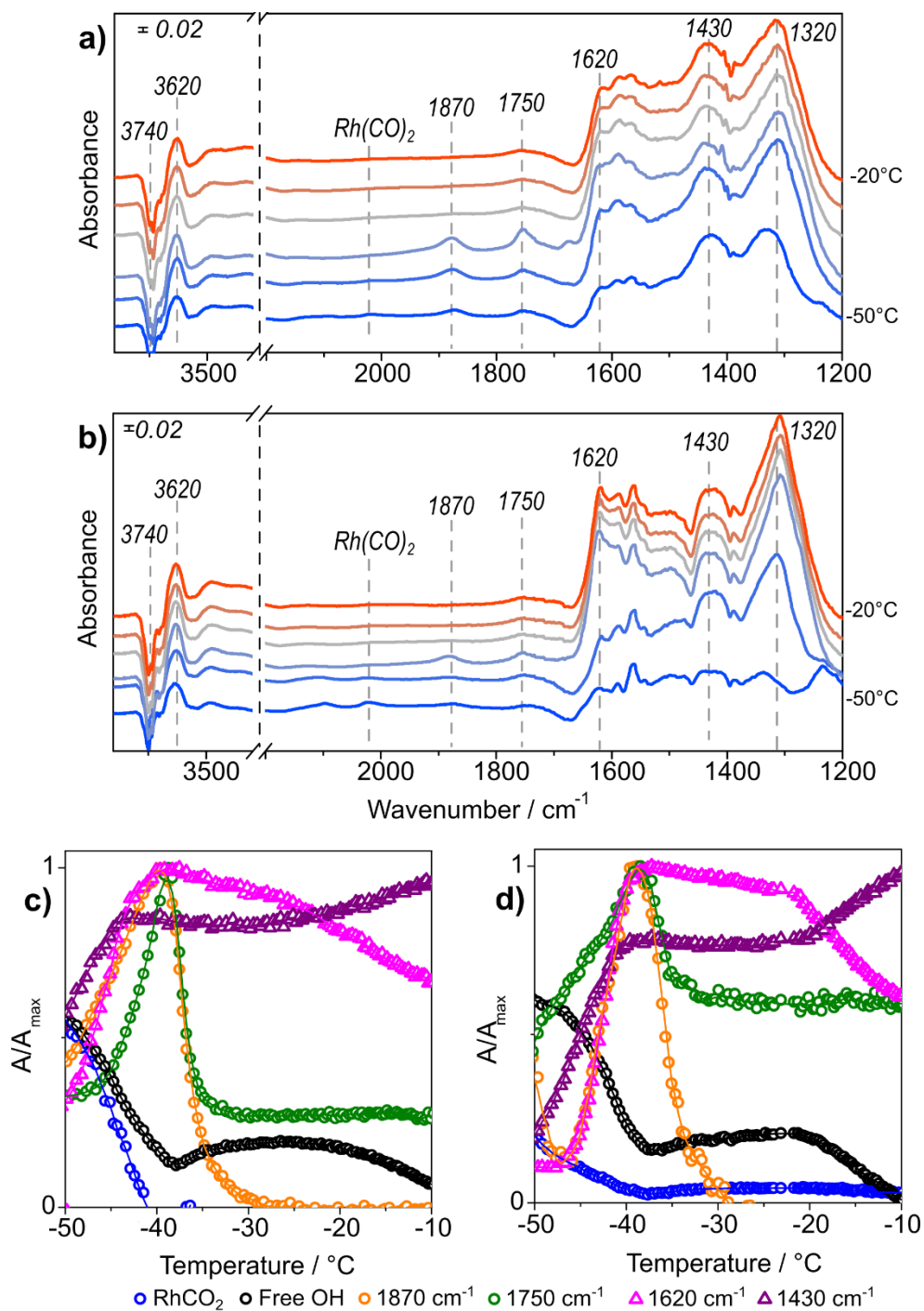
Figure 20. IR spectra of 0.1 wt.% Rh/γ-Al₂O₃ first saturated with CO to form Rh(CO)₂, (a) photolyzed at –120 °C in 1000 ppm NO or (b) exposed at –115 °C to 1000 ppm NO, during warming from –50 to –20 °C. Traces of Rh(CO)₂ (blue), free surface *OH (black), Rh–NO at 1870 (orange) and 1750 cm⁻¹ (green), and species at 1620 (pink) and 1430 cm⁻¹ (purple) during warming after (c) photolysis and (d) cryogenic NO exposure. Lines in (c) and (d) are to guide the eye.

47

Photolysis in 1.5% NO at –120 °C was also performed on $Rh(^{13}CO)_2$ (Figure 21), generated by exposure to pure ^{13}CO at 150 °C for 15 minutes to identify peaks containing C derived from $Rh(CO)_2$. Before photolysis, $Rh(^{13}CO)_2$ peaks were present in IR at 2037 and 1967 cm^{-1} with no visible peaks near 2090 and 2020 cm^{-1}, indicating that no ^{12}CO was present on Rh. During photolysis, a similar difference in the rate of loss of the symmetric and asymmetric *CO peaks of $Rh(CO)_2$ was observed, but a peak also formed at 2084 cm^{-1} and grew with time. The difference spectrum scaled to the size of the asymmetric stretch before and after photolysis reveals that two peaks formed during photolysis: one at 2042 cm^{-1} and another at 2084 cm^{-1}, similar to the peak between 2080–2090 cm^{-1} which formed during photolysis of natural $Rh(CO)_2$ (Figure 21c). We attribute the peak at 2042 cm^{-1} to ν_{CO} of $Rh(^{13}CO)(NO)_2$, but the presence of the peak at 2084 cm^{-1} suggests that only a fraction of $Rh(CO)(NO)_2$ was formed from $Rh(^{13}CO)_2$. The remainder may have formed from residual C-containing species on the support that were not removed during the oxidation and reduction pretreatment. Photolytic generation of unsaturated Rh at low temperature may have promoted reverse spillover of these species onto Rh sites during formation of $Rh(CO)(NO)_2$. This clearly shows that ligand exchange between atomically dispersed Rh species and the γ-Al_2O_3 support can be rapid.
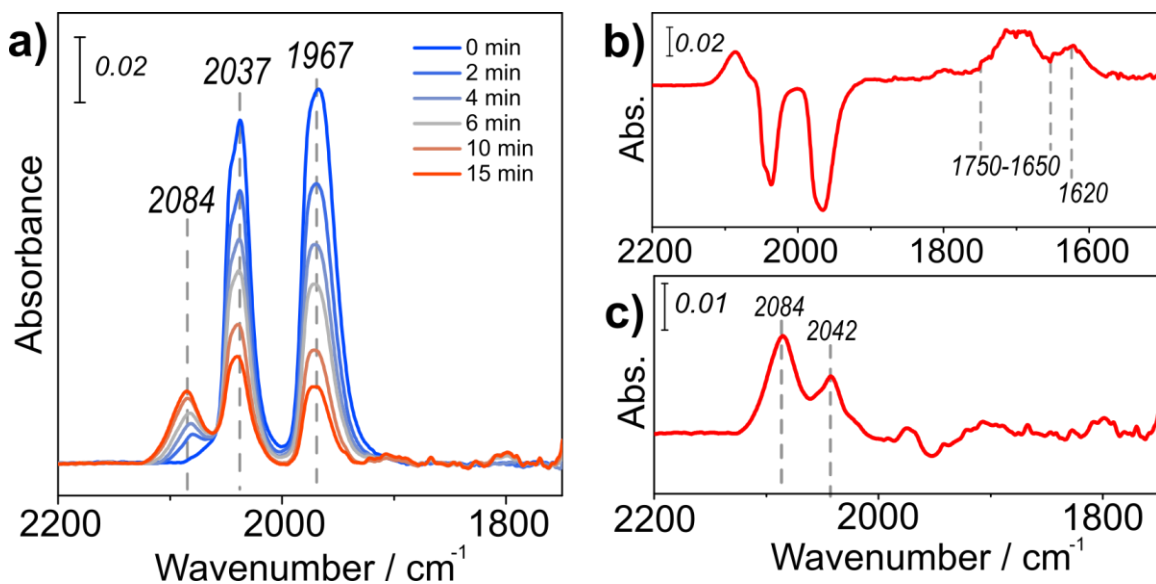
Figure 21. (a) IR spectra of photolysis of Rh(^{13}CO)$_2$ in 0.1 wt.% Rh/γ-Al$_2$O$_3$ in flowing 1.5% NO under vacuum at -120 °C using 370 nm light. Panel (b) contains difference spectra (subtracted with common scale) from beginning to end of photolysis. Panel (c) shows the difference spectrum between spectra at 15 and 0 minutes in panel (a), scaled to minimize the size of $\nu_{CO,asym}$ at 1967 cm^{-1}.

The subsequent warming of the material containing a fraction of Rh(^{13}CO)(NO)$_2$ and Rh(^{13}CO)$_2$ looked equivalent to the warming of ^{12}CO systems (Figure 22). Peaks at 1870 and 1750 cm^{-1} appeared *without* any additional nearby peaks. Even if some ^{12}CO was present on the material, the absence of shifted peaks when ^{13}CO is present indicates that these are entirely Rh–NO species. Therefore, we assign features at 1870 cm^{-1} and 1750 cm^{-1} to *NO adsorbed on Rh sites from reverse spillover NO-derived surface species to Rh$_2$ (discussed in greater detail below). Similar behavior is noted from 1650–1200 cm^{-1}, which shows qualitatively identical behavior to that of experiments with natural CO. Figure 23 shows the difference spectra from -120 to -20 °C of the 1650–1200 cm^{-1} region for comparison between the ^{13}CO and ^{12}CO systems, both of which show similar changes during warming. The strong absorbance of peaks and overlap with between nitrate and carbonate species makes it difficult to discern whether shifted peaks are present, but this does suggest that a majority of these peaks do not contain CO derived from Rh(CO)$_2$.

Notably, the *CO_2 feature at 2343 cm^{-1} was still quite intense in the ^{13}CO experiment, but the feature at 2277 (corresponding to *$^{13}CO_2$ on γ-Al_2O_3) is roughly 5 % of the area of the peak at 2343 cm^{-1}, compared to 0.75 % in the ^{12}CO experiments. The fact that the 2343 cm^{-1} peak remains dominant is likely a result of the reverse spillover of ^{12}CO to Rh which occurred during photolysis, but a larger *$^{13}CO_2$ feature at 2277 cm^{-1} in this experiment than in ^{12}CO experiments confirms this is indeed *CO_2.
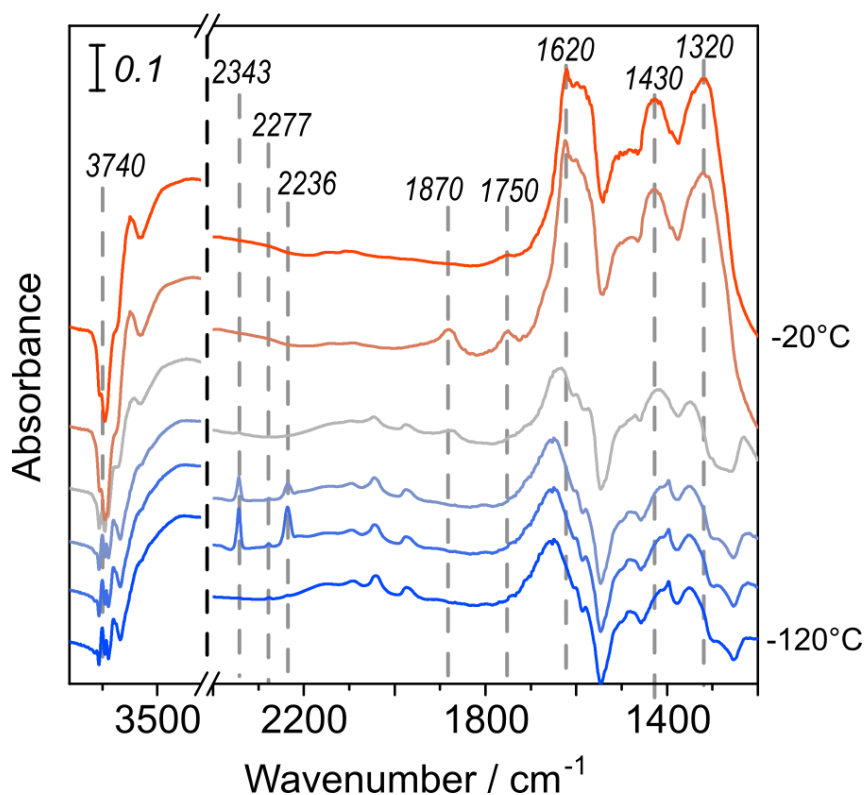
Figure 22. IR spectra of photolyzed Rh(^{13}CO)$_2$ during warming from –120 °C to –20 °C. Background spectrum taken at 150 °C. Large positive features at 1650 and 1400 cm^{-1} and the negative feature at 1550 cm^{-1} are due to background shifts from 150 °C to –120 °C.
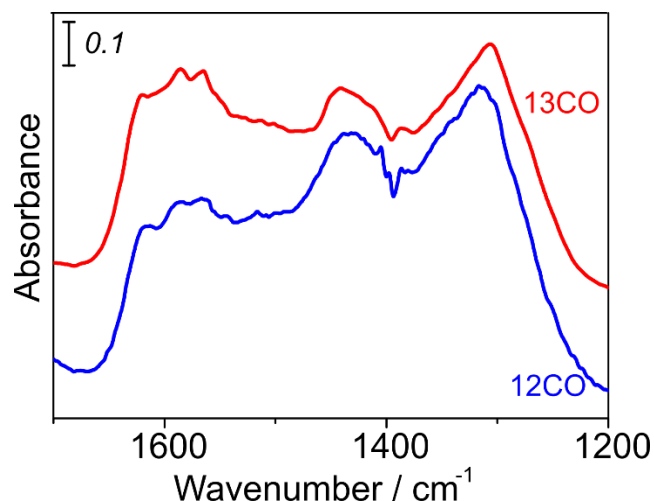
Figure 23. Difference IR spectra from –120 °C to –20 °C during warming of photolyzed $Rh(^{12}CO)_2$ (blue) and photolyzed $Rh(^{13}CO)_2$ (red).

The substantial growth of nitrates and/or N-acids on the support during warming of the material that had seen NO but not been photolyzed requires that substantial *NO was present on the material prior to reaction with $Rh(CO)_2$, yet the only spectral change attributable to NO during NO adsorption is the appearance of a very small feature at 1850 cm^{-1} (Figure 13). This phenomenon has been observed previously in cryogenic CO oxidation over Au/TiO_2 catalysts,[100] in which CO deposited at 120 K disappears from IR spectra after purging of the sample cell but reacts to form CO_2 upon introduction of O_2 to the catalyst. Disappearance of adsorbed *CO from IR spectra during evacuation was not discussed. The cause of the near invisible NO in our system could be configurational, in which configurations of adsorbed *NO at low temperature diminish the intensity of absorbance bands. Parallel adsorption does decrease absorbance in methods such as reflection adsorption infrared spectroscopy (RAIRS), in which IR light is reflected off a uniform surface and the orientation of absorbers affects absorbance.[101] This cannot be directly applied to DRIFTS, which does not rely on specular reflection of IR light, but it suggests that adsorption configuration, which is expectedly related to temperature, may play a role in this phenomenon.

5.2. Discussion of Low Temperature Reactions

In both photolyzed and unphotolyzed samples that were exposed to NO at low temperature and warmed to room temperature (during which time all observable *CO on Rh reacted), $Rh(CO)_2$ is not regenerated by admission of CO at room temperature. Instead, a small feature between 2150–2155 cm^{-1} is formed, which is indicative of CO adsorption on Rh^{+3},[90] (Figure 24). This indicates that Rh was oxidized from Rh^{+1}, as it exists in $Rh(CO)_2$, to Rh^{+3} during the surface reactions that occurred during warming from $-120\ °C$ to room temperature.
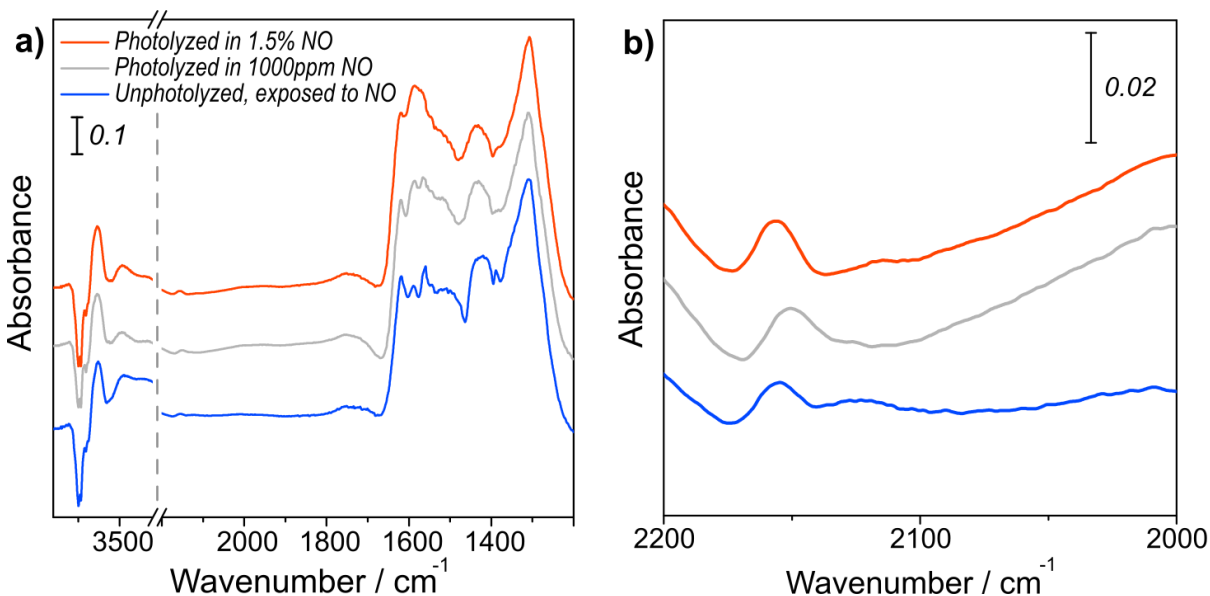
Figure 24. IR spectra of 0.1 wt.% $Rh/\gamma-Al_2O_3$ at 20 °C after saturation with CO, then cryogenic exposure to 1000 ppm NO (blue), photolysis in 1000 ppm NO (gray), or photolysis in 1.5% NO (red) under vacuum, followed by resaturation with CO at 20 °C. Panel (b) shows the 2200–2000 cm^{-1} region in panel (a) in greater detail.

The formation of $Rh^{+3}(CO)$ upon exposure of the reacted Rh species to CO at room temperature suggested that both decomposition of $Rh(CO)(NO)_2$ and $Rh(CO)_2$ (by reaction with NO-derived surface species) resulted in Rh oxidation. While the mechanism of Rh oxidation is unclear, it is possible that additional Rh–OH bonds form upon loss of *NO and *CO ligands from Rh which may oxidize Rh. EXAFS of $Rh(CO)_2$ during temperature

programmed desorption shows an increase in Rh–O coordination number, indicating that Rh oxidation can also occur during loss of *CO from $Rh(CO)_2$ at high temperature.[82] While the precise structure of Rh after *CO desorption is not clear from these experiments, an oxidized Rh^{+3} site is likely in an octahedral coordination environment.[102] This environment could include association of H_2O and *OH with Rh, the latter being derived from dissociation of multiple H_2O molecules and subsequent H_2 evolution and Rh oxidation from +1 to +3. In our system, some of these ligands may instead be derived from *NO, though again the precise structure of this Rh^{+3} species is not further evaluated in this work.

At this point, we will assign peaks that have been noted thus far in IR and make tentative hypotheses about what occurs during these low temperature reactions. Peaks at 1870 and 1750 cm^{-1} are likely Rh–NO species, based on previous studies of NO adsorption on Rh.[30,33,34] These features also align with the low temperature IR of NO adsorption on 0.1 wt.% Rh/γ-Al_2O_3 (Figure 12)—a catalyst in which Rh is atomically dispersed under reaction conditions (Figure 2). This suggests that Rh–NO features at 1870 and 1750 cm^{-1} correspond to atomically dispersed Rh species, but this is not confirmed as there may be a small fraction of Rh clusters present after reduction that are dispersed by CO *in situ* (which would not have occurred prior to collection of the spectrum in Figure 12). We do not focus on possible structural rearrangement of Rh during these processes, but this should be a consideration of future studies. The peak at 1870 cm^{-1} is near the frequency of NO gas at 1876 cm^{-1}, suggesting that this is a weakly interacting Rh–NO species. The free electron of NO allows it to adopt either a cationic (linear) or anionic (bent) configuration upon adsorption onto metals, leading to either electron transfer to or from the metal to NO, respectively.[22] Linear bound *NO can have frequencies above 1900 cm^{-1}, while bent *NO on Rh typically exhibits frequencies below

1800 cm^{-1}. Therefore, we assign the Rh–NO feature at 1750 cm^{-1} to bent *NO ligands (Rh(NO$^-$))—consistent with oxidation of Rh that was observed during the warming process.

The formation and decay of the feature at 1230 cm^{-1} in favor of higher frequency features is often observed in the adsorption of NO$_2$ to alumina and is indicative of a nitrite to nitrate conversion.[85,86] Peaks near 1640, 1460, 1430, 1230, and 3610 cm^{-1} are associated with bicarbonate formation upon reaction of CO$_2$ with surface *OH,[92,93,96,98] peaks near 1560, 1510, and 1300 cm^{-1} are associated with carbonates,[96,99] peaks near 1590, 1390, and 1320 cm^{-1} have been associated with formates on alumina,[96] and peaks near 1620, 1590, 1560, 1430, and 1320 cm^{-1} have been associated with nitrates.[85,86,97] The significant overlap of these features makes it difficult to assign these features to specific species in all spectra. Thus, changes in these regions are taken to be indicative of surface reactions involving *NO, *CO, *OH, or a combination thereof, unless precluded by other factors.

The loss of Rh(CO)$_2$ after photolysis in NO or NO treatment in the dark is not preceded by meaningful changes in the IR spectra that would indicate a reactive NO-derived surface species, likely because *NO is still tightly bound to the surface and unavailable for both reaction and observation in IR. In the unphotolyzed material, initiation of Rh(CO)$_2$ loss is followed by loss of *OH between 3700–3800 cm^{-1} on the support and generation of the nitrite band at 1230 cm^{-1} (Figure 18b,d), showing the connection between all three species. In the photolyzed material, substantial loss of *OH on the support precedes loss of Rh(CO)$_2$ by ~10 °C, though Rh(CO)(NO)$_2$ may be interacting with *OH during this time as it reacts (Figure 18a,c). The second maximum and first maximum of Rh–NO peaks at 1870 and 1750 cm^{-1} coincide with loss of *OH, loss of nitrites, and growth of nitrates, suggesting that this conversion process is involved with *NO population of Rh sites (Figure 20).

Hydroxyls likely play multiple roles in the decomposition of $Rh(CO)_2$, and three primary roles seem reasonable: by coordinating to and oxidizing Rh, by reacting with *CO in a reactive spillover process, or by reaction with NO. The first route would require either negatively charged *OH groups that swap support Al counterions for Rh, oxidizing Rh in the process, or dissociation of multiple H_2O and evolution of H_2 to produce two *OH species bound to Rh. Temperature programmed desorption of *CO has also been observed to cause an increase Rh–O coordination, suggesting the involvement of surface *OH or H_2O in replacement of *CO ligands and Rh oxidation.[82] The latter two routes of *OH interaction are evidenced by the appearance of IR peaks at 3620, 3480, and 3350 cm^{-1} (Figure 18), suggesting the formation of new *OH containing species (bicarbonates, formates, acids, etc. containing stretches between 1620 and 1200 cm^{-1}). Previous studies have noted the formation of these species upon adsorption of CO, CO_2, and NO_2 onto γ-Al_2O_3.

Whether loss of *CO concerts with *NO population of Rh is unclear—*CO could be reacting with *OH to form formates and bicarbonates, but the use of ^{13}CO during photolysis suggested that only a small fraction of features between 1620 and 1200 cm^{-1} contained CO from $Rh(CO)_2$, so the fate of *CO from $Rh(CO)_2$ in these reactions at low temperature is not clear. Reaction of $Rh(CO)_2$ with *OH alone is unlikely, as this does not occur in catalysts that were not exposed to NO at cryogenic temperatures, so we conclude that there are NO-derived surface species accessible to $Rh(CO)_2$ that facilitate reactive desorption of CO. A simple bond order conservation model would suggest that loss of *CO from $Rh(CO)_2$ requires to additional bonds to Rh to form; *NO support species may fulfill this role at low temperature in a way *OH alone cannot. Rh oxidation is also observed during this process—it may also occur concurrently with *CO desorption and may be an important role of *NO in the process.

The role of OH and acid in NO reduction catalysis over Rh atoms was also noted in the homogeneous $[RhCl_2(CO)_2]^-$ system.[23] There, both water and acid were found to increase the NO reduction reaction rate, which was rationalized by a proposed mechanism that includes water and acid in the catalytic cycle to mediate CO oxidation and NO reduction. In this mechanism, consumption of $[RhCl_2(CO)(NO)_2]^-$ began first with CO insertion, followed by reaction with H^+ to protonate NO ligands and reaction with H_2O to form a carboxyl ligand, and ended with decomposition to yield N_2O, CO_2, and reform H_2O and H^+. No alternative mechanisms in the absence of water and acid were provided. Interestingly, the presence of acid also affected the most abundant Rh species even for the same initial NO:CO ratio of 4:3. In the absence of acid, $[RhCl_2(CO)_2]^-$ was the dominant Rh species and its conversion to a Rh–NO–CO species was limiting. However, in the presence of acid, conversion of $[RhCl_2(CO)_2]^-$ to a mixed intermediate was facile such that the most abundant Rh species became the proposed $[RhCl_2(CO)(NO)_2]^-$ intermediate similar to what we identified via photolysis. It is possible, then, that acidic –OH groups generated by reaction of NO and *OH in our heterogeneous system could be a key factor in the reactivity of $Rh(CO)_2$ at low temperature.

It is worth noting that the onset of $Rh(CO)_2$ decomposition in the unphotolyzed system occurs *after* (at higher temperature during warming from cryogenic temperature) the onset of $Rh(CO)(NO)_2$ decomposition but *before* loss of residual $Rh(CO)_2$ remaining after photolysis (Figure 18c–d). This suggests that there are populations of $Rh(CO)_2$ that are more reactive than the rest; these $Rh(CO)_2$ are preferentially consumed during photolysis *or* are the first to react with surface *NO species during warming. Our study of *OH interactions with $Rh(CO)_2$ found that *OH dense regions of alumina facilitate *CO desorption from $Rh(CO)_2$ by stabilizing $Rh(CO)$, and that the heterogeneity of Al_2O_3 and its hydroxyl distribution can generate

relatively distinct populations of $Rh(CO)_2$. Multiple phases of formation of Rh–NO at 1870 cm^{-1} and differences between photolyzed and unphotolyzed $Rh(CO)_2$ suggest that there are different populations of $Rh(CO)_2$ that react differently.

Surface $*H_2O$ and $*OH$ are also implicated in the formation of nitrates during warming due to coincidence in changes in the IR spectra. Around –25 °C, peaks at 1320 and 1430 cm^{-1} grow at the expense of other features from 1200–1650 cm^{-1} (trace of 1430 cm^{-1} is representative of both peaks, Figure 20c–d), which is consistent with solvation of nitrate species in water.[85,97] As these nitrates become solvated, a broad absorbance band from 3500 to 2600 cm^{-1} begins to grow (not shown in Figure 20), indicating a growing hydrogen bonding network of surface $*OH$. This is likely due to a combination of trace water in the Ar feed and reorganization of surface water and $*OH$ with increasing temperature, and it reinforces interactions between water (and $*OH$) and NO-derived support species. It also supports the notion that $Rh(CO)_2$ is not solvated in $*OH$ dense regions at cryogenic temperature, only solvating as the catalyst approaches room temperature (Figure 6).

We aim to interpret the low temperature reactivity of $Rh(CO)(NO)_2$ and of $Rh(CO)_2$ with NO-derived surface species in the context of the high temperature (~ 200 °C) reduction of NO—for instance, determining if the formation of $Rh(CO)(NO)_2$ and/or the reaction of $Rh(CO)_2$ with surface derived NO species is operative at normal reaction conditions. At 200 °C, DFT predicts that $Rh(CO)(NO)_2$ is no longer in a significant free energy well among possible substitution products on $Rh(CO)_2$, but it is still more energetically favorable than $Rh(CO)$ or $Rh(CO)(NO)$ (Figure 15), though these calculations do not consider kinetics of formation or reactions of these intermediates. Therefore, we consider the transient formation of $Rh(CO)(NO)_2$ at reaction conditions to be a reasonable possibility, though we do not confirm

it here. There are two factors of the low temperature experiments that must be studied further in the context of high temperature reactions, which we start to address with the remainder of this work: the feasibility of a Rh redox process during a turnover of the reaction, and reactive *CO desorption with NO-derived surface species.

5.3. Regeneration of Rh(CO)$_2$ after Low Temperature Reactions

If Rh oxidation occurs in the course of a single turnover of NO reduction, then re-reduction of Rh would be required to replenish the most abundant Rh(CO)$_2$ species, in which Rh is in the +1 oxidation state. To investigate the re-reduction of Rh, catalysts were heated from room temperature to 380 °C after low temperature NO treatment (with and without photolysis) in either 5000 ppm CO or a mixture of 5000 ppm CO and 1000 ppm NO (the same mixture used in reactions) and monitored in IR. Note that these heating treatments were performed under vacuum, as required by the low temperature treatment. Heating of photolyzed systems was performed on catalysts that had been photolyzed in 1.5% NO, rather than 1000 ppm, but the spectra of the catalysts at room temperature appear similar between catalysts photolyzed in 1000 ppm or 1.5% NO or exposed to 1000 ppm NO at low temperature (Figure 24).

While heating the photolyzed catalyst at 20 °C min^{-1} in 5000 ppm CO, the Rh^{+3}(CO) peak at 2155 cm^{-1} grew in intensity and shifted to 2125 cm^{-1} by 320 °C (Figure 25a), though it should be noted that the reported temperature reading may exceed the actual bed temperature by up to 20 °C. The latter frequency of 2125 cm^{-1} is still high enough to suggest *CO is adsorbed to an oxidized Rh site, and some researchers have assigned this feature to an Rh^{+2}(CO), but the assignment has not been rigorously verified.[17,89] Alternatively, features at

2155 and 2125 cm^{-1} could correspond to Rh^{+3}(CO) in different local environments (e.g. low and high local *OH density, respectively). Either way, this suggests that the re-reduction of Rh^{+3} to Rh^{+1} may be a multistep process. At the same time, a feature emerged at 1938 cm^{-1} and shifted to 1905 cm^{-1} as it continued to grow. Above 320 °C, the *CO feature at 2125 cm^{-1} and feature at 1905 cm^{-1} decayed as Rh(CO)$_2$ peaks at 2089 and 2020 cm^{-1} appeared. Appearance of Rh(CO)$_2$ was met with rapid development of a doublet at 2250 and 2232 cm^{-1} corresponding to isocyanate (*NCO) on the support, which is also observed at reaction conditions with *in situ* IR. This suggests that formation of Rh(CO)$_2$ is required to turn over the reaction, and that residual *NO species were either on or adjacent to Rh, since NO was not flowing during heating. While this occurred more than 100 °C above which *NCO formation is observed *in situ*, the temperature was ramped at 20 °C min^{-1}, so appreciable rates of Rh reduction and Rh(CO)$_2$ formation at 200 °C cannot be excluded.

The behavior of the unphotolyzed catalyst exposed to 1000 ppm NO at –115 °C during a 20 °C min^{-1} temperature ramp in 5000 ppm CO began similarly to the photolyzed catalyst. Upon CO introduction at room temperature, a peak at 2155 cm^{-1} appeared indicating the formation of Rh^{+3}(CO), as well as a shoulder at 2120 cm^{-1} (Figure 25b). While warming the peak at 2155 cm^{-1} slowly shifted to 2125 cm^{-1}, and peaks at 2101 and 2034 cm^{-1} appeared by 155 °C. These likely correspond to Rh(CO)$_2$, but the frequencies are higher than those observed at similar temperatures during CO adsorption prior to low temperature treatment (2087 and 2013 cm^{-1}). This is also far below the temperature at which Rh(CO)$_2$ reformed in the photolyzed sample. Altogether this suggests that these Rh(CO)$_2$ were formed from a population of more reducible Rh species that were not present after photolysis. These Rh(CO)$_2$ peaks

decreased in intensity and slowly redshifted before growing again at 2090 and 2022 cm^{-1} at 315 °C, at which point *NCO also began to form.
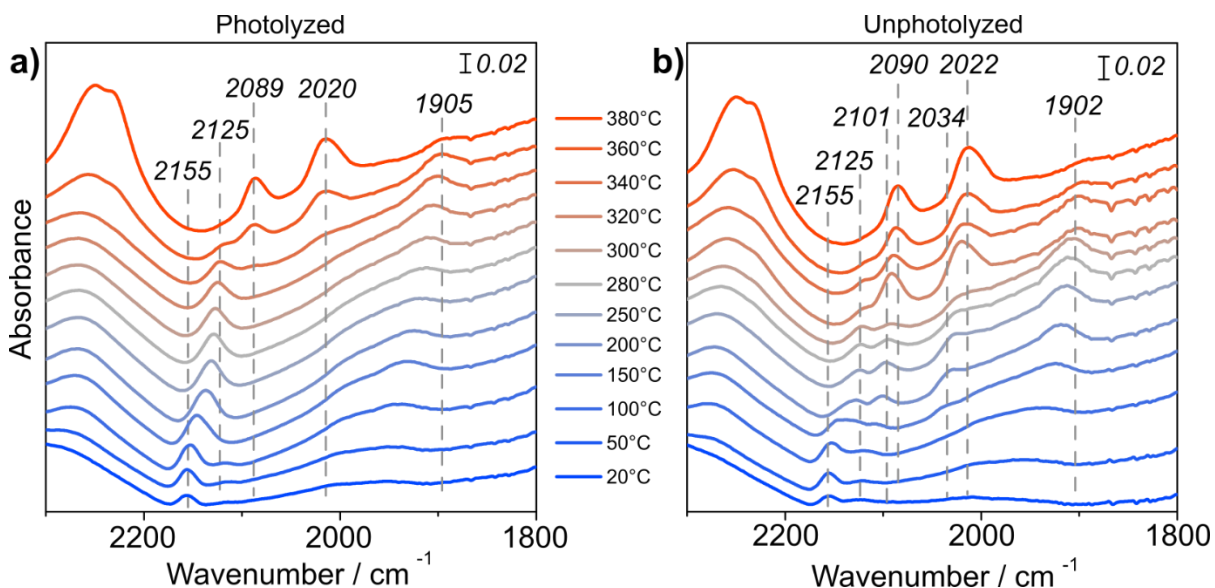
Figure 25. IR spectra of 0.1 wt.% Rh/γ-Al$_2$O$_3$ in flowing 5000 ppm CO under vacuum during heating from 20 °C to 380 °C at 20 °C min^{-1} after (a) photolysis in 1.5% NO and (b) after cryogenic exposure to 1000 ppm NO.

Heating the photolyzed sample in 5000 ppm CO and 1000 ppm NO produced very similar results to heating the unphotolyzed catalyst in 5000 ppm CO alone, noted by a similar formation and shift of the *CO feature starting at 2155 cm^{-1} and by the formation and decay of a high frequency Rh(CO)$_2$ species at 165 °C (Figure 26). The cause of the appearance of these high frequency bands in the unphotolyzed sample and photolyzed sample heated in NO and CO is unclear, but the lack of stability of this Rh(CO)$_2$ species in either CO or the NO/CO mixture is notable as this has not been observed in any other *in situ* IR studies in this work.

Also notable is the absence of the peaks corresponding to *NCO at 2250 and 2232 cm^{-1} even when the high frequency Rh(CO)$_2$ is present in flowing NO and CO at and above 200 °C. Under similar conditions (but at ambient pressure) for a catalyst that had not been taken to

low temperature, *NCO peaks were observed (Figure 2). This suggests either that this unstable high frequency $Rh(CO)_2$ is not reactive, or that it is reactive but does not proceed through a mechanism that produces *NCO. While the mechanism of *NCO production from $Rh(CO)_2$ is not known, it suggests that the high frequency $Rh(CO)_2$ are mechanistically distinct from other active $Rh(CO)_2$ that do produce *NCO. This is consistent with our previous work suggesting that Rh–OH interactions may be an important factor in determining the mechanism of NO reduction, since *OH can stabilize Rh monocarbonyl species and promote *CO desorption, and that $Rh(CO)_2$ in *OH dense regions of alumina tend to have lower vibrational frequencies. This high frequency $Rh(CO)_2$ species is likely not in an *OH dense region of $\gamma\text{-}Al_2O_3$, and so does not follow the same mechanism (if it catalyzes NO reduction at all).
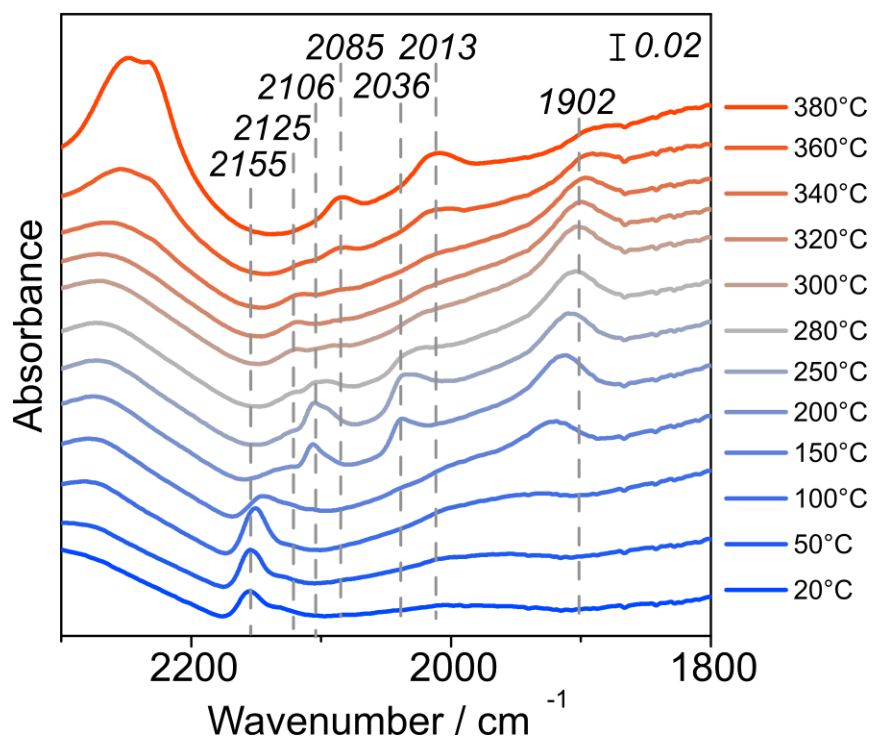
Figure 26. IR spectra of 0.1 wt.% $Rh/\gamma\text{-}Al_2O_3$ in flowing 5000 ppm CO and 1000 ppm NO under vacuum during heating from 20 °C to 380 °C at 20 °C min^{-1} after photolysis in 1.5% NO at –120 °C.

Heating of the photolyzed $Rh(^{13}CO)_2$ was also performed in flowing ^{13}CO to identify *CO species that form from the gas phase during heating (Figure 27). As expected, a band at

2100 cm^{-1} corresponding to Rh^{+3}(^{13}CO) appeared instead of at 2155 cm^{-1} upon ^{13}CO adsorption. The following heating process in ^{13}CO proceeded similarly to that in ^{12}CO. The peak at 2100 cm^{-1} shifted to 2080 cm^{-1} while a peak at 1940 cm^{-1} formed. This is the same frequency seen in ^{12}CO, indicating that this peak either corresponds to an *NO species or a *CO species formed by spillover of residual ^{12}C species from the support to Rh sites, which also occurred during low temperature photolysis. Loss of Rh^{+3}(CO) and the peak at 1940 (now shifted to 1920 cm^{-1}) is met with the growth of peaks at 2048 and 1980 cm^{-1} corresponding to Rh(^{13}CO)$_2$ at 275 °C. These peaks shift to 2044 and 1977 cm^{-1} by 350 °C, at which point *NCO is formed at 2189 and 2170 cm^{-1}. This is consistent with the previous result that high frequency Rh(^{12}CO)$_2$ do not produce *NCO.
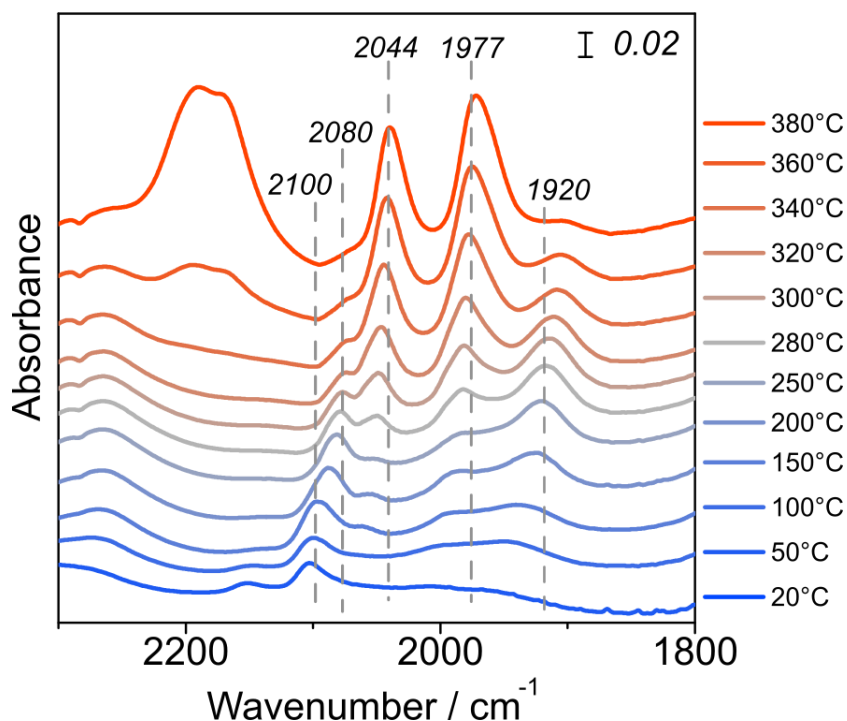
Figure 27. IR spectra of 0.1 wt.% Rh/γ-Al$_2$O$_3$ in flowing ^{13}CO under vacuum during heating from 20 °C to 380 °C at 20 °C min^{-1} after photolysis of Rh(^{13}CO)$_2$ in 1.5% NO at −120 °C.

5.4. Mechanistic Insights from Photolysis and Low Temperature Experiments

The low temperature experiments suggest three aspects of a potential NO reduction mechanism, which are summarized below and depicted in Figure 28:

First, $Rh(CO)(NO)_2$ forms when NO interacts with an unsaturated $Rh(CO)$ species. Unsaturated $Rh(CO)$ was generated via photolysis of $Rh(CO)_2$ at low temperature, but this may be achieved with a thermal or reactive *CO desorption process at high temperature. Both photolysis and thermal desorption of *CO to generate $Rh(CO)$ require local *OH species to stabilize $Rh(CO)$. The formation of $Rh(CO)(NO)_2$ at 200 °C is consistent with DFT that suggests it is more stable than either $Rh(CO)$ or $Rh(CO)(NO)$ species, and its high reactivity while warming in inert atmosphere at cryogenic temperature is consistent with *in situ* IR at elevated temperature in NO reduction reaction conditions that show only the presence of $Rh(CO)_2$. Similar intermediates have also been proposed in the homogeneous NO reduction chemistry ($[RhCl_2(CO)(NO)_2]^-$)[22,23] and in the atomically dispersed Rh/CeO_2 system[20] ($Rh(CO)(N_2O_2)$, in which two NO ligands have dimerized).

Second, $Rh(CO)_2$ interacts with *OH and NO-derived surface species. The complete reaction of $Rh(CO)_2$ below –20 °C caused by *NO (even in the unphotolyzed system exposed to NO at cryogenic temperature, where the nature of the adsorbed NO-derived species could not be determined by IR) suggests a very low energy barrier to this process, and the question remains whether the same type and amount of *NO surface species form at high temperature. It is possible that such a reactive desorption process could be involved in either the unsaturation of Rh sites for interaction with NO gas or the NO reduction pathway itself.

Third, interaction of $Rh(CO)_2$ with *NO surface species at low temperature and decomposition of $Rh(CO)(NO)_2$ oxidize Rh^{+1} to Rh^{+3}, suggesting a Rh redox cycle may be

involved in NO reduction catalysis. The oxidizing species are likely a combination of *NO and/or *OH/H_2O derived species, with Figure 28 qualitatively depicting this scenario. Metal oxidation by NO is a common aspect of NO coordination chemistry, and is reversible by CO treatment. Both intermediates in the homogeneous[22,23] ($[RhCl_2(CO)(NO)_2]^-$) and atomically dispersed Rh/CeO_2[20] (Rh(CO)(N_2O_2)) chemistries also implicate Rh oxidation from +1 to +3. The conversion of Rh^{+1} to Rh^{+3} could stabilize additional ligands via conversion from 4-coordinate (square planar) to 5- or 6-coordinate (square pyramidal or octahedral) geometries.[102] Two *NO ligands would likely be required to oxidize Rh to +3, and a variety of reaction pathways involving additional *CO ligands could be conceived. An oxidative NO adsorption process is also consistent with the lack of reactivity of Rh^{+3} before reduction and formation of $Rh^{+1}(CO)_2$—NO may not be able to displace other oxidizing ligands from Rh^{+3}, but it can oxidize a square planar Rh(CO)$_2$ complex and stabilize a complex with multiple *NO and *CO ligands *in situ*. Subsequent reactions could conceivably involve the re-reduction of Rh^{+3} to Rh^{+1} in the form of Rh(CO)$_2$, allowing the catalytic cycle to turn over.
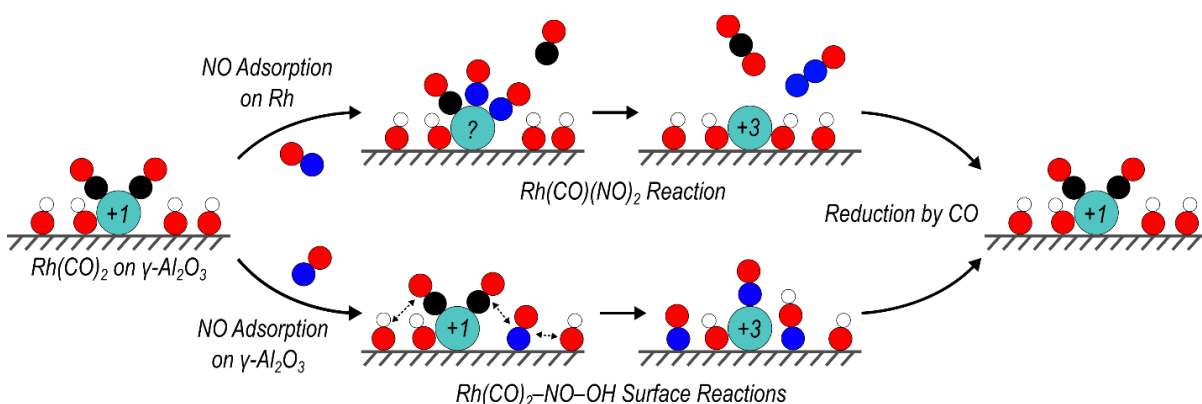
Figure 28. Proposed reaction pathways for Rh(CO)$_2$ during low temperature experiments. *CO desorption from Rh(CO)$_2$ (induced by photolysis) leads to formation of highly reactive Rh(CO)(NO)$_2$. Alternatively, NO adsorption on γ-Al_2O_3 leads to surface reactions between Rh(CO)$_2$, *NO, and *OH that consumes Rh(CO)$_2$. In both processes, Rh is oxidized from +1 to +3, but heating in CO leads to reduction of Rh and formation of Rh(CO)$_2$. (Rh = blue, N = blue, C = black, O = red, H = white).

While these hypothetical mechanistic steps provide insight to the mechanism of the catalytic reaction at 200 °C, they are not definitive as the types of surface species that form at high temperature could be different in identity and amount from those formed at low temperature. However, the reactivity of $Rh(CO)_2$ with *NO surface species at low temperature and the higher reactivity of the identified $Rh(CO)(NO)_2$ species are instructive: if conditions at high temperature dictate that these processes can occur, then their low energetic barrier suggests that they will. Therefore, we turn to investigating the catalytic system at high temperature to determine whether these processes occur at TWC conditions and propose a series of follow up experiments to address gaps in the present work.

6. IR of Atomically Dispersed Rh/γ-Al₂O₃ at or near Reaction Conditions

The reactivity of $Rh(CO)_2$ after exposure to NO at $-115\ °C$ motivates the question of whether $Rh(CO)_2$ is stable in NO at any temperature and whether the reactive NO-derived species is on the surface or in the gas phase. To test this, $Rh(CO)_2$ was generated by exposure of a previously oxidized Rh/γ-Al₂O₃ to 5000 ppm CO at 205 °C for 30 minutes on the same 0.1 wt.% Rh/γ-Al₂O₃ catalyst used for low temperature experiments. It was then exposed to 1000 ppm NO at ambient pressure (whereas low temperature experiments were conducted under vacuum) at various temperatures to provide the most liberal conditions for NO adsorption and potential reaction with $Rh(CO)_2$ (Figure 29). At 30 °C, $Rh(CO)_2$ is stable in both Ar and 1000 ppm NO, with less than 1 % loss of the symmetric *CO stretch after 2 minutes in either gas. There is a negative feature at 2032 cm^{-1}, but this is attributed to displacement of *CO on a small fraction of Rh clusters in the sample by *NO, which then leads to a peak at 1815 cm^{-1} that may correspond to *NO on Rh clusters.[29] There is no change in the region between 1650 and 1200 cm^{-1}, though the low temperature experiments demonstrated that NO and CO derived species on the support should be observable at this temperature if formed in large amounts.

After NO exposure at 30 °C, the catalyst was heated in Ar back to 205 °C. Re-exposure to CO was performed for 20 minutes until a similar level of $Rh(CO)_2$ saturation was achieved as in the initial state of this experiment. The catalyst was then cooled to 100 °C and again exposed to 1000 ppm NO. At this temperature $Rh(CO)_2$ remains stable in Ar, but is not stable in NO, with an 8 % loss in $Rh(CO)_2$ area in the first 2 minutes of NO exposure. The same process of heating in Ar, CO re-exposure at 205 °C, and exposure to NO at 205 °C and 150 °C

was performed. The rate of $Rh(CO)_2$ consumption in NO increased with increased temperature of NO exposure, while in Ar the species remained stable. These rates are shown in Figure 29c as the fraction of initial area of the symmetric stretch lost per minute (over a 2 minute period of maximum rate of loss) in either Ar or 1000 ppm NO as a function of temperature. There are two points in Figure 29c corresponding to low temperature experiments in which $Rh(CO)_2$ was cooled to -120 °C and held in Ar or exposed to NO. The rate of $Rh(CO)_2$ loss in those experiments was computed as the fractional area lost per minute over a 2 minute range centered at the temperature of maximum $Rh(CO)_2$ loss in the NO exposed catalyst, -56 °C.
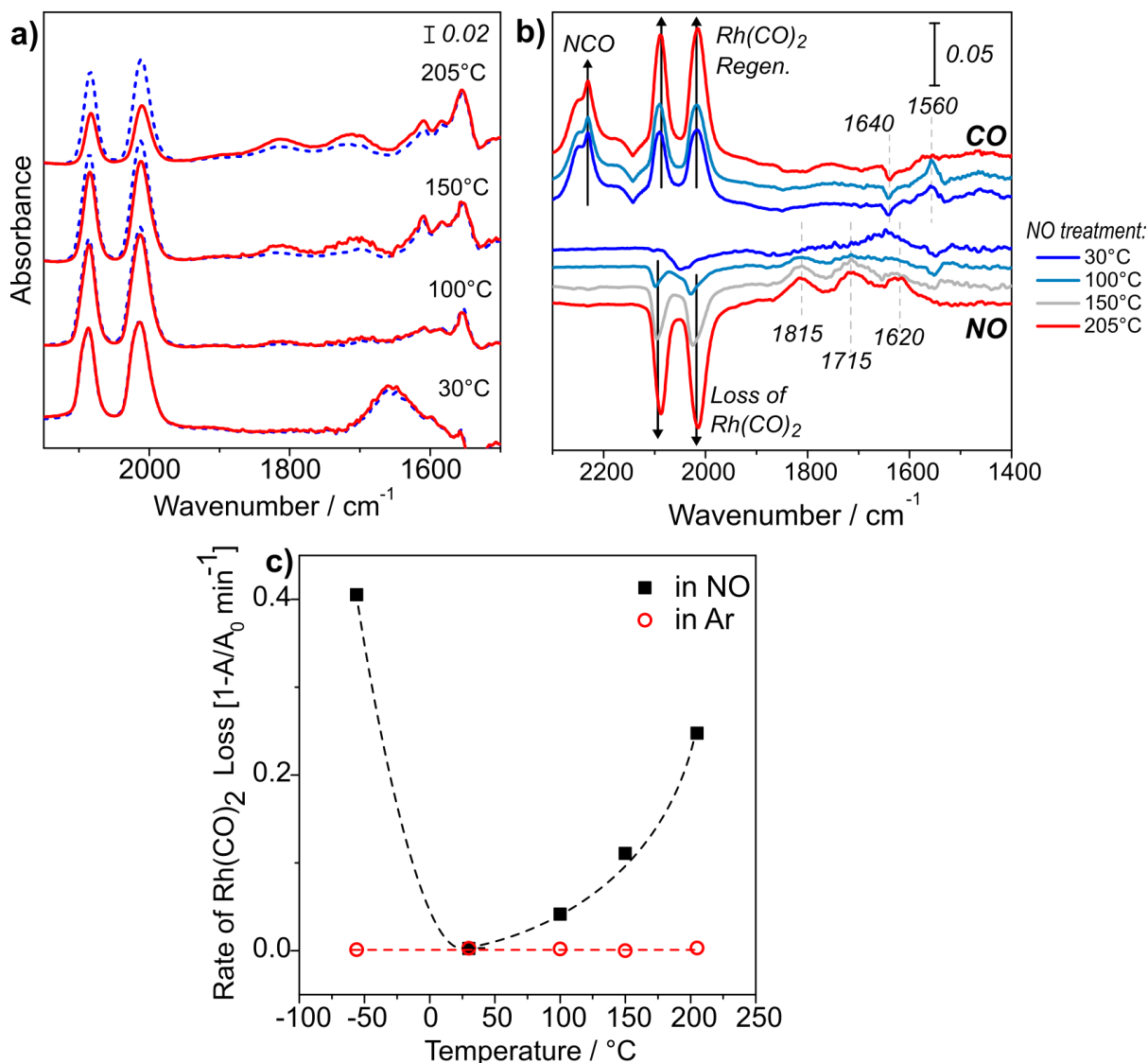
Figure 29. (a) IR spectra of 0.1 wt.% Rh/γ-Al$_2$O$_3$ during exposure to 0.1 kPa NO at 30, 100, 150, and 205 °C. The catalyst was first saturated with 0.5 kPa CO at 205 °C to form Rh(CO)$_2$, then cooled to treatment temperature in Ar. Spectra were taken after 1 minute (blue dash) and 3 minutes in NO (red line). (b) Difference spectra after 3 minutes in NO at 30, 100, 150, and 205 °C and after 3 minutes in CO at 205 °C following each treatment (except after 150 °C). Treatments were performed in the following order: 30, 100, 205, 150 °C. (c) Rate of loss of Rh(CO)$_2$ area at different temperatures, computed by loss of the symmetric stretch from 1 to 3 minutes in NO (black square) or in Ar (red circle) prior to NO treatment. Points at –56 °C correspond to the 2 minute average (about the maximum) rate of loss during warming *in Ar* after cryogenic treatment in NO (black square) or Ar (red circle).

At all temperatures, loss of Rh(CO)$_2$ in NO was met with generation of peaks near 1810, 1710, and 1615 cm^{-1}, likely corresponding to *NO adsorbed to Rh sites. These differ from the Rh–NO peaks observed during warming from low temperature at 1870 and 1750 cm$^-$

68

[1], suggesting that distinct species form in each temperature regime. The features formed at high temperature may correspond to *NO on small Rh clusters, based on the replacement of *CO on clusters at 30 °C and the typical frequencies of *NO on clusters of 1820 and 1685 cm^{-1}.[29] A clustering mechanism has been proposed for reactions of atomically dispersed Rh for NO reduction by CO, but this mechanism is often invoked to explain the rapid increase of conversion during light-off as the catalyst approaches and exceeds 300 °C.[25]

The distinction between high and low temperature behavior is also evident by the rapid regeneration of $Rh(CO)_2$ in the experiments depicted in Figure 29 (which had previously been consumed by reaction with NO at 205 °C) by exposure to CO at 205 °C. After low temperature reaction of $Rh(CO)_2$ with surface-bound *NO species, $Rh(CO)_2$ regeneration proceeded first by formation of $Rh^{+3}(CO)$ followed by reduction to Rh^{+1} and formation of $Rh(CO)_2$ at 320 °C (in a 20 °C min^{-1} ramp). However, $Rh^{+3}(CO)$ was not observed during CO exposure following reaction with NO at 205 °C, and $Rh(CO)_2$ formation began immediately upon CO admission. In fact, the rate of increase in $Rh(CO)_2$ peak area was 2.5 times higher upon CO admission than the rate of loss upon NO admission at the same temperature. The lack of $Rh^{+3}(CO)$ observation in these high temperature experiments and rapid $Rh(CO)_2$ regeneration could mean that either Rh was not oxidized to Rh^{+3}, or that its oxidizing ligands were more susceptible to reaction with CO. The lability of *NO ligands to act as oxidizers or neutral ligands in metal coordination chemistry could explain differences between low temperature and high temperature behavior even if Rh is oxidized to Rh^{+3} in both reactions. At low temperature, *OH is consumed during loss of $Rh(CO)_2$, whereas no *OH is consumed by interaction with NO at high temperature. *OH consumption at low temperature can be attributed to formation of acidic NO–OH species on the support, but also to Rh oxidation by adjacent *OH (or *H_2O)

groups. It may be that there is a higher barrier to the removal of these oxidizing ligands, derived from either *OH (*H_2O) or *NO, by reaction with CO than the removal of *NO present on Rh at and above 100 °C.

The apparent negative activation barrier between –56 and 30 °C in Figure 29c is similar to observations of CO oxidation catalysis over Au/TiO_2,[100] in which particular TiO_2 sites stabilized CO adsorption at low temperature, where it could react with O_2 on Au. We attribute the low temperature behavior in our study to a surface reaction between Rh(CO)$_2$ and surface bound NO-derived species, in which both the reaction kinetics and surface concentration of *NO species are temperature dependent. At –56 °C, the surface concentration of reactive NO-derived species is high enough such that even with low thermal energy, the reaction proceeds quickly. At room temperature and above, it may be that a similar surface reaction can occur kinetically, but that the surface concentration of reactive NO-derived species is too low. At temperatures of 100 °C and above, Rh(CO)$_2$ could be reacting through the same surface mediated mechanism, now with the coverage of NO-derived surface species limiting the rate but with sufficient thermal energy to turn over the majority of attempts. Alternatively, an entirely different mechanism could be operative, such as transient formation of a reactive 3+ ligand Rh species (such as Rh(CO)(NO)$_2$) that seemed likely based on the photolysis experiments.

At 205 °C, the rate of regeneration of Rh(CO)$_2$ (after reaction of Rh(CO)$_2$ with NO at 205 °C) upon introduction of 5000 ppm CO is 2.5 times higher than the rate of loss in 1000 ppm NO at the same temperature. These are the same concentrations used during reactions and *in situ* IR at similar temperatures, so one may interpret this result as indicative of the following process during reaction: NO reacts with Rh(CO)$_2$ at the rates observed in Figure 29 during

reaction, but $Rh(CO)_2$ is regenerated as soon as it is consumed during reaction, so the *in situ* IR spectra show only the presence of $Rh(CO)_2$. The rate of loss of $Rh(CO)_2$ in NO at 205 °C corresponds to a turnover frequency of approximately 4 minutes, similar to the steady state reaction rate in 0.5 kPa CO and 0.1 kPa NO at the same temperature in preliminary kinetic studies. This suggests that the mechanism by which NO reacts with $Rh(CO)_2$ in the absence of gaseous CO may be that which occurs during reaction.

Consumption of $Rh(CO)_2$ by reaction with NO should be a favorable condition for the generation of NO-derived surface species, rather than CO-derived species (since there is no gaseous CO), and regeneration of $Rh(CO)_2$ should generate the latter. Figure 29b shows the difference spectra after 3 minutes in either 5000 ppm CO at 205 °C or 1000 ppm NO at 30, 100, 150, and 205 °C. During each NO exposure at or above 100 °C, negative features appear near 2090 and 2020 cm^{-1}, indicating consumption of $Rh(CO)_2$, and positive features at 1815 and 1713 cm^{-1} are indicative of Rh–NO species (Figure 29b). At 205 °C, the same peaks are also visible with an additional positive feature at 1617 cm^{-1}, which may be attributed to nitrate formation on the support. This indicates that as temperature increases, *NO spillover occurs to form more surface nitrates. At 30 °C, negative $Rh(CO)_2$ features are very small while a single negative feature at 2032 cm^{-1} is more prominent, indicating loss of linear bound *CO on Rh clusters. This is likely due to dispersion of Rh clusters into atoms, as intensity at this frequency remained low following CO and NO exposures. Each CO exposure at 205 °C generated positive features at 2250, 2230, 2089, and 2015 cm^{-1} indicating the formation of *NCO and $Rh(CO)_2$, respectively (Figure 29b). A negative feature at 1640 cm^{-1} and positive feature at 1560 cm^{-1} indicate interactions with surface species, possibly a change in binding modes of a nitrate or carbonate. It is worth noting that the overall coverage of surface species is likely to

71

be lower than during low temperature treatment, so it is not surprising that surface reactions are not well resolved in IR at these conditions.

The absence of *NCO generation during NO exposure to $Rh(CO)_2$, during which $Rh(CO)_2$ reacts, indicates that NO reaction with $Rh(CO)_2$ alone either does not follow the same mechanism or does not produce a full turnover of the reaction that occurs in mixtures of NO and CO. Reintroduction of CO does produce *NCO, suggesting that *NCO production may originate from regeneration of $Rh(CO)_2$ in the catalytic cycle.

The final indication of reaction between $Rh(CO)_2$ and NO-derived surface species *in situ* is an apparent (though small) decrease in stability of $Rh(CO)_2$ after exposure to the reaction mixture of 5000 ppm CO and 1000 ppm NO (1 bar) at 190 °C. IR spectra of $Rh(CO)_2$ in 0.05 wt.% $Rh/\gamma-Al_2O_3$ after 3 and 5 minutes in Ar (following CO adsorption) are nearly indistinguishable, and the difference spectrum shows only 2 % loss of $Rh(CO)_2$ area during this time (Figure 30). Peaks at 1650, 1590, 1560, 1470, 1435, and 1240 cm^{-1} are visible after CO adsorption, indicating formation of a mix of carbonates, bicarbonates, and formates. Note that previous studies of residence time distributions of gases in similar Harrick DRIFTS cells have found that 90% of gas in the cell can be purged out in 66 seconds at a flow rate of 45 cm^3 min^{-1} at 25 °C.[103] Our cells are purged with Ar at 70 cm^3 min^{-1} (20 °C reference) when the cell is at 190 °C, so well over 90% of the 5000 ppm CO gas mixture should be purged after 180 seconds in Ar and indicates that $Rh(CO)_2$ stability in IR is not simply due to equilibrium with gas phase CO.

When $Rh(CO)_2$ is then exposed to a mixture of 5000 ppm CO and 1000 ppm NO (1 bar), *NCO bands appear at 2250 and 2230 cm^{-1} and absorbance increases at 1612, 1590, 1560, and 1460 cm^{-1}, which could indicate carbonate and/or nitrate formation. Importantly, when the

NO/CO mixture is purged for 3 minutes in Ar, $Rh(CO)_2$ intensity decreases by 5 % in the following 2 minutes (Figure 30b). This is 2.5 times more $Rh(CO)_2$ loss than after exposure to only CO, suggesting that exposure to NO and CO conferred a small degree of reactivity to $Rh(CO)_2$, potentially through the formation of nearby NO-derived surface species that react with $Rh(CO)_2$. Again, it is likely that more than 90% of the gas mixture (which contains CO and NO in a 5:1 ratio) was purged by Ar prior to collection of these spectra, suggesting this is due to reactions on the surface. The difference spectrum during this 2 minute loss does not indicate consumption of surface *NO species between 1650 and 1200 cm^{-1}, but this could be due to relatively low extinction coefficients and coverages of these species relative to $Rh(CO)_2$.
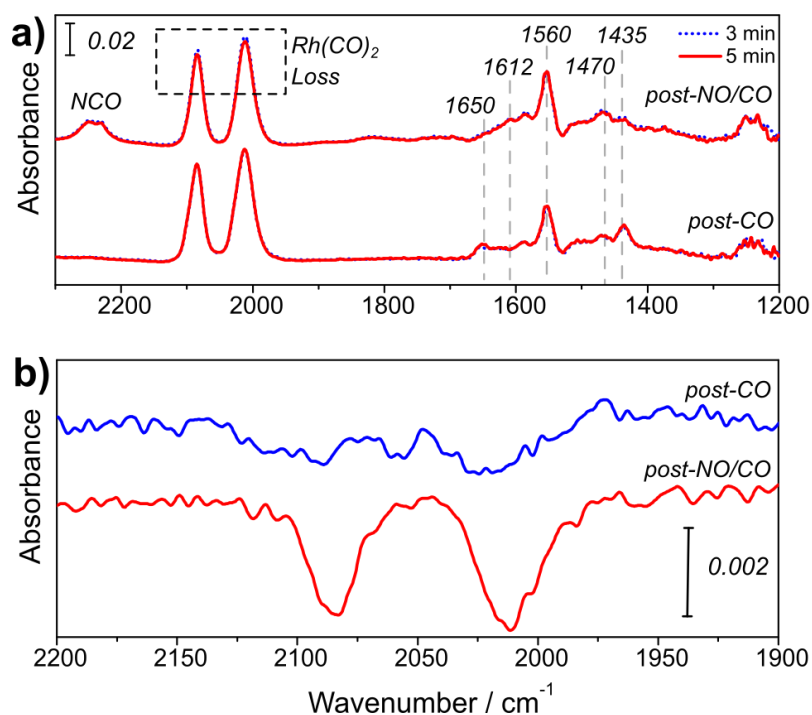
Figure 30. (a) IR spectra of 0.05 wt.% Rh/γ-Al_2O_3 following exposure to 0.5 kPa CO for 20 minutes then after exposure to 0.5 kPa CO and 0.1 kPa NO for 25 minutes, after purging in Ar for 3 minutes (blue dash) and 5 minutes (red line). (b) Difference spectra from 3 to 5 minutes in Ar after exposure to CO (blue) and after exposure to NO and CO (red).

The reactivity of $Rh(CO)_2$ after exposure to NO and CO is consistent with a surface reaction mechanism between $Rh(CO)_2$ and NO-derived surface species observed at cryogenic

temperatures, while the negative apparent activation barrier of $Rh(CO)_2$ reactions with NO from cryogenic to ambient temperature suggests a possible shift from a surface- to desorption-mediated reaction. Next, we outline experiments aimed at clarifying the operative mechanism of $Rh(CO)_2$ reactivity at TWC startup conditions.

7. Conclusions and Suggested Experiments

We first established that interactions between Rh(CO)$_2$ and *OH on γ-Al$_2$O$_3$ affect Rh(CO)$_2$ reactivity by lowering the energy barrier for *CO desorption from Rh(CO)$_2$ and stabilizing the Rh(CO) product. These interactions likely occur through Rh(CO)$_2$ migration to *OH dense regions of γ-Al$_2$O$_3$, from which *CO desorption occurs (Figure 31) and are relevant at reaction temperature. The remainder of the work expanded on this notion of Rh(CO)$_2$ interactions with support-bound species by identifying reactions between Rh(CO)$_2$ and NO-derived species on the support. We also employed photolysis to generate observable amounts of a potential reactive intermediate in the reduction of NO by CO, Rh(CO)(NO)$_2$. These conclusions are described below and depicted in Figure 32, and subsequent experiments to explore their mechanistic relevance at high temperature are proposed.

Dense Surface OH Promote CO Desorption & Rh(CO) Formation
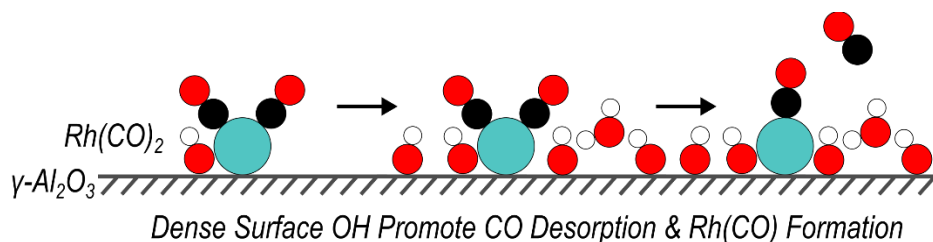
Figure 31. Schematic of Rh(CO)$_2$ behavior during temperature programmed desorption, in which Rh(CO)$_2$ translates on the γ-Al$_2$O$_3$ surface into *OH dense regions. These *OH promote *CO desorption and stabilize the Rh monocarbonyl. (Rh = blue, C = black, O = red, H = white).
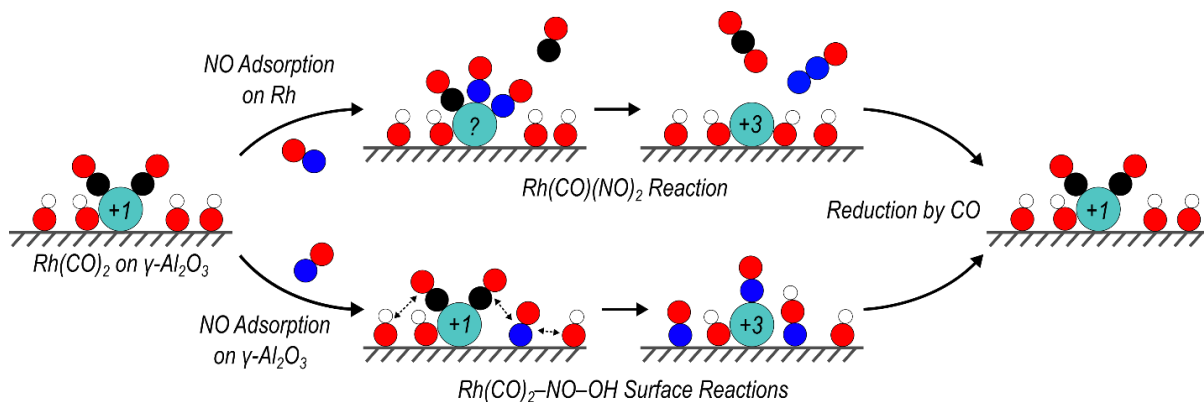
Figure 32. Proposed (simplified) reaction pathways for $Rh(CO)_2$ during low temperature experiments. *CO desorption from $Rh(CO)_2$ (induced by photolysis) leads to formation of highly reactive $Rh(CO)(NO)_2$. Alternatively, NO adsorption on γ-Al_2O_3 leads to surface reactions between $Rh(CO)_2$, *NO, and *OH that consumes $Rh(CO)_2$. In both processes, Rh is oxidized from +1 to +3, but heating in CO leads to reduction of Rh and formation of $Rh(CO)_2$. (Rh = blue, N = blue, C = black, O = red, H = white).

First, $Rh(CO)(NO)_2$ is a reasonable candidate for the Rh intermediate formed during reaction. This intermediate was formed upon NO adsorption to unsaturated Rh(CO) generated by photolysis at low temperature, where it was observed in IR to have vibrations at approximately 2080–2090 cm^{-1} and between 1750–1650 cm^{-1}. This species is highly reactive and appeared to generate CO_2 and N_2O upon decomposition which was complete below –50 °C. It also aligns with similar species proposed, but not spectroscopically identified, in previous studies of NO reduction by CO over Rh atoms: $Rh(CO)(N_2O_2)$ in Rh/CeO$_2$[20] and $[Rh(CO)(NO)_2Cl_2]^-$ in the homogeneous chemistry.[22,23] UV-vis spectroscopy in the homogeneous chemistry was used to identify $[RhCl_2(CO)_2]^-$, but experimental limitations precluded its use to identify $[Rh(CO)(NO)_2Cl_2]^-$ *in situ*—though researchers noted that the intermediate was green. This motivates *in situ* UV-vis for the Rh/γ-Al_2O_3 system: cryogenic photolysis of $Rh(CO)_2$ in the presence of NO could be performed under observation with UV-vis. Rh–CO absorption bands of $Rh(CO)_2$ near 260 and 325 nm should decrease during photolysis[82] as a new band, potentially near 500 nm according to studies of the homogeneous chemistry,[22,23] should appear as $Rh(CO)(NO)_2$ forms. Importantly, this technique could also be

used to monitor the oxidation state of Rh during warming, as fully oxidized Rh/γ-Al$_2$O$_3$ (via reaction with O$_2$) has a broad absorbance band around 440 nm.[82]

We consider the formation of the Rh(CO)(NO)$_2$ intermediate to be reasonable at reaction conditions based on the formation of Rh(CO) by thermal desorption of *CO, and DFT suggests that Rh(CO)(NO)$_2$ is the most stable intermediate at the experimental conditions and has similar vibrational frequencies to those observed by IR. However, in our study it is unclear whether this species is formed by adsorption of gaseous NO to Rh(CO) or by reverse spillover of *NO from NO-derived surface species—we only attempted to form this intermediate in the presence of gaseous NO. An experiment to interrogate the formation mechanism of Rh(CO)(NO)$_2$ could involve the generation of Rh(CO)$_2$, then exposure of the catalyst to NO at cryogenic temperature, followed by photolysis in Ar. NO exposure should generate surface-bound NO-derived species and photolysis should generate unsaturated Rh(CO) species. If Rh(CO)(NO)$_2$ does not form during photolysis, then it would suggest that reactions of surface bound NO-derived species with Rh(CO)$_2$ (observed when Rh(CO)$_2$ was exposed to NO at cryogenic temperatures, followed by warming to room temperature) proceed through a different mechanism than NO adsorption onto unsaturated Rh(CO) sites to form Rh(CO)(NO)$_2$.

The second conclusion of this work is that Rh can be oxidized from +1 to +3 by surface interactions of Rh(CO)$_2$ with NO-derived species and/or after formation and decomposition of Rh(CO)(NO)$_2$. This hypothesis parallels redox cycles described in homogeneous NO reduction by [RhCl$_2$(CO)$_2$]$^-$ and proposed pathways of NO reduction over atomically dispersed Rh/CeO$_2$, and it could conceivably occur during reaction here. While we do not know the coordination environment of Rh^{+3} generated in low temperature reactions, if CO can reduce this species back to Rh^{+1}(CO)$_2$ on a faster timescale than the overall reaction, then it is eligible for

continued consideration in reaction mechanisms. This can be tested by performing the low temperature reaction of $Rh(CO)_2$ with surface bound NO-derived species, then exposing to CO at various temperatures (held constant, rather than the temperature programmed experiment that was performed already) and monitoring the rate of $Rh(CO)_2$ formation in IR.

The last, most interesting conclusion of this work is that $Rh(CO)_2$ can readily react with surface-bound NO-derived species below –50 °C, despite being stable in NO at room temperature. This likely proceeds by reaction of $Rh(CO)_2$ with both *OH and *NO surface species; IR spectra and previous studies of the homogeneous catalytic system suggest that acidic NO-derived species generated by reaction with *OH may be relevant to the reactivity. To investigate whether surface reactions between $Rh(CO)_2$ and NO-derived surface species on Al_2O_3 are relevant at high temperature, the following experiment can be performed. First, isotopically labeled nitrates can be generated by exposure of the catalyst (already containing $Rh(CO)_2$) to a mixture of ^{15}NO and O_2 at room temperature (or above). Assuming that these nitrates are not sufficiently concentrated to immediately react with $Rh(CO)_2$ at room temperature, heating the catalyst in CO and ^{14}NO after labeled nitrate deposition would be useful. If labeled reaction products ($^{15}N_2O$ or $^{15}N_2$) are observed (either by mass spectrometry or gas phase FTIR) before $^{14}N_2$ or $^{14}N_2O$, then it is likely that surface reactions of nitrates with $Rh(CO)_2$ occurred before interaction with gas phase NO, and that such a surface mechanism could be operative at typical reaction conditions. Another potential experiment for discriminating between these pathways could involve the generation of nitrates by flowing NO and O_2 at $Rh(CO)_2$ at a variety of temperatures. If a promotional effect to $Rh(CO)_2$ reactivity is afforded by generating nitrates at ambient temperature (at which $Rh(CO)_2$ is stable in NO)

but not at elevated temperature (~200 °C), then it is likely that surface reactions indeed cease to be relevant at reaction temperature.

This work highlights many potential complexities of NO reduction by CO over atomically dispersed Rh and that future studies must consider more than simply the species on Rh. Interactions with *OH and NO-derived surface species on γ-Al_2O_3, and resulting Rh oxidation, have been demonstrated here, but future study is needed to confirm their importance under typical reaction conditions. Finally, the identification of $Rh(CO)(NO)_2$ as the potential intermediate was performed with a photolysis technique that may prove useful for similar chemistries. This intermediate may also inform subsequent theoretical studies of possible reaction paths. Importantly, we do not identify possible routes for the production of N_2, which is observed in dry NO reduction over atomically dispersed Rh. This is the desired product of the reaction, so future studies should also be aimed at connecting the processes described here to that of N_2 production. In total, clarifying mechanistic aspects of dry NO reduction will ultimately provide a framework for study of NO reduction in the presence of water, the reaction of interest to manufacturers seeking to reduce harmful emissions.

References

(1)   Gerard, D.; Lave, L. B. Implementing Technology-Forcing Policies: The 1970 Clean Air Act Amendments and the Introduction of Advanced Automotive Emissions Controls in the United States. *Technological Forecasting and Social Change* **2005**, *72* (7), 761–778.

(2)   Shelef, M.; Graham, G. W. Why Rhodium in Automotive Three-Way Catalysts? *Catal. Rev.* **1994**, *36* (3), 433–457.

(3)   Kean, A. J.; Harley, R. A.; Littlejohn, D.; Kendall, G. R. On-Road Measurement of Ammonia and Other Motor Vehicle Exhaust Emissions. *Environmental Science and Technology* **2000**, *34*, 3535–3539.

(4)   Rood, S.; Eslava, S.; Manigrasso, A.; Bannister, C. Recent Advances in Gasoline Three-Way Catalyst Formulation: A Review. *Proc. Inst. Mech. Eng., Part D* **2020**, *234* (4), 936–949.

(5)   Cavanagh, R. R.; Yates, J. T. Site Distribution Studies of Rh Supported on Al2O3 - An Infrared Study of Chemisorbed CO. *J. Chem. Phys.* **1981**, *74* (7), 4150–4155. https://doi.org/10.1063/1.441544.

(6)   Getsoian, A. (Bean); Theis, J. R.; Paxton, W. A.; Lance, M. J.; Lambert, C. K. Remarkable Improvement in Low Temperature Performance of Model Three-Way Catalysts through Solution Atomic Layer Deposition. *Nat. Catal.* **2019**, *2* (7), 614–622.

(7)   Solymosi, F.; Pásztor, M. An Infrared Study of the Influence of CO Chemisorption on the Topology of Supported Rhodium. *J. Phys. Chem.* **1985**, *89*, 4789–4793.

(8)   Solymosi, F.; Bánsági, T.; Novák, E. Effect of NO on the CO-Induced Disruption of Rhodium Crystallites. *J. Catal.* **1988**, *112*, 183–193.

(9)   Paul, D. K.; Yates, J. T. Protection of a Rh/Al$_2$O$_3$ Catalyst under Extreme Environmental Conditions. *J. Phys. Chem.* **1991**, *95*, 1699–1703.

(10)   Goldsmith, B. R.; Sanderson, E. D.; Ouyang, R.; Li, W. X. CO- and NO-Induced Disintegration and Redispersion of Three-Way Catalysts Rhodium, Palladium, and Platinum: An Ab Initio Thermodynamics Study. *J. Phys. Chem. C* **2014**, *118*, 9588–9597.

(11)   Van't Blik, H. F. J.; van Zon, J. B. A. D.; Koningsberger, D. C.; Prins, R. EXAFS Determination of the Change in Structure of Rhodium in Highly Dispersed Rh/γ-Al$_2$O$_3$ Catalysts after CO and/or H$_2$ Adsorption at Different Temperatures. *J. Mol. Catal.* **1984**, *25*, 379–396.

(12)   Yates, J. T.; Kolasinski, K. Infrared Spectroscopic Investigation of the Rhodium Gem-Dicarbonyl Surface Species. *The Journal of Chemical Physics* **1983**, *79* (2), 1026–1030. https://doi.org/10.1063/1.445844.

(13)   Dent, A. J.; Evans, J.; Fiddy, S. G.; Jyoti, B.; Newton, M. A.; Tromp, M. Rhodium Dispersion during NO/CO Conversions. *Angew. Chem.* **2007**, *119* (28), 5452–5454.

(14)   Ouyang, R.; Liu, J. X.; Li, W. X. Atomistic Theory of Ostwald Ripening and Disintegration of Supported Metal Particles under Reaction Conditions. *J. Am. Chem. Soc.* **2013**, *135* (5), 1760–1771.

(15)   Suzuki, A.; Inada, Y.; Yamaguchi, A.; Chihara, T.; Yuasa, M.; Nomura, M.; Iwasawa, Y. Time Scale and Elementary Steps of CO-Induced Disintegration of Surface Rhodium Clusters. *Angew. Chem.* **2003**, *115* (39), 4943–4947.

(16)   Srinivasan, A.; Depcik, C. Review of Chemical Reactions in the NO Reduction by CO on Rhodium/Alumina Catalysts. *Catal. Rev.: Sci. Eng.* **2010**, *52* (4), 462–493.

(17)   Rice, C. A.; Worley, S. D.; Curtis, C. W.; Guin, J. A.; Tarrer, A. R. The Oxidation State of Dispersed Rh on Al2O3. *J. Chem. Phys.* **1981**, *74* (11), 6487–6497.

(18)   Basu, P.; Panayotov, D.; Yates, J. T. Rhodium-Carbon Monoxide Surface Chemistry: The Involvement of Surface Hydroxyl Groups on Al2O3 and SiO2 Supports. *J. Am. Chem. Soc.* **1988**, *110*, 2074–2081.

(19)   Asokan, C.; Yang, Y.; Dang, A.; Getsoian, A.; Christopher, P. Low-Temperature Ammonia Production during NO Reduction by CO Is Due to Atomically Dispersed Rhodium Active Sites. *ACS Catal.* **2020**, *10* (9), 5217–5222.

(20)   Khivantsev, K.; Vargas, C.; Tian, J.; Kovarik, L.; Jaegers, N. R.; Szanyi, J.; Wang, Y. Economizing on Precious Metals in Three-Way Catalysts: Thermally Stable and Highly Active Single-Atom Rhodium on Ceria for NO Abatement under Dry and Industrially Relevant Conditions. *Angew. Chem. Int. Ed.* **2021**, *60*, 391–398.

(21)   Yao, H. C.; Japar, S.; Shelef, M. Surface Interactions in the System Rh/Al2O3. *J. Catal.* **1977**, *50*, 407–417.

(22)   Eisenberg, R. The Coordination Chemistry of Nitric Oxide. *Acc. Chem. Res.* **1975**, *8*, 26–34.

(23)   Meyer, C. D.; Eisenberg, R. The Catalytic Reduction of Nitric Oxide by Carbon Monoxide Using Dichlorodicarbonylrhodium(I) Anion. *J. Am. Chem. Soc.* **1976**, *98* (6), 1364–1371.

(24)   Zhang, S.; Tang, Y.; Nguyen, L.; Zhao, Y. F.; Wu, Z.; Goh, T. W.; Liu, J. J.; Li, Y.; Zhu, T.; Huang, W.; Frenkel, A. I.; Li, J.; Tao, F. F. Catalysis on Singly Dispersed Rh Atoms Anchored on an Inert Support. *ACS Catalysis* **2018**, *8* (1), 110–121.

(25) Newton, M. A.; Jyoti, B.; Dent, A. J.; Fiddy, S. G.; Evans, J. Synchronous, Time Resolved, Diffuse Reflectance FT-IR, Energy Dispersive EXAFS (EDE) and Mass Spectrometric Investigation of the Behaviour of Rh Catalysts during NO Reduction by CO. *Chemical Communications* **2004**, No. 21, 2382–2383.

(26) Smith, B. C. *Fundamentals of Fourier Transform Infrared Spectroscopy*, 2nd ed.; CRC Press, 2011.

(27) Yang, A. C.; Garland, C. W. Infrared Studies of Carbon Monoxide Chemisorbed on Rhodium. *J. Phys. Chem.* **1957**, *61*, 1504–1512.

(28) Yates, J. T.; Duncan, T. M.; Worley, S. D.; Vaughan, R. W. Infrared Spectra of Chemisorbed CO on Rh. *J. Chem. Phys.* **1979**, *70* (3), 1219–1224.

(29) Hoffman, A. J.; Asokan, C.; Gadinas, N.; Kravchenko, P.; Getsoian, A. B.; Christopher, P.; Hibbitts, D. Theoretical and Experimental Characterization of Adsorbed CO and NO on γ-Al_2O_3-Supported Rh Nanoparticles. *J. Phys. Chem. C* **2021**, *125*, 19733–19755.

(30) Dictor, R. IR Study of the Behavior of CO, NO, and CO+NO over Rh-Al2O3. *J. Catal.* **1988**, *109*, 89–99.

(31) Hyde, E. A.; Rudham, R.; Rochester, C. H. Infrared Study of the Interactions between NO and CO on Rh/Al_2O_3 Catalysts. *J. Chem. Soc., Faraday Trans.* **1984**, *80*, 531–547.

(32) Hamadeh, I.; Griffiths, P. Diffuse Reflectance FT-IR Studies of the Adsorption of CO on Rh/Al_2O_3 Catalysts. *Appl. Spectrosc.* **1987**, *41* (4), 611.

(33) Solymosi, F.; Sarkany, J. An Infrared Study of the Surface Interaction Between NO and CO on Rh/Al2O3 Catalyst. *Appl. Surf. Sci.* **1979**, *3*, 68–82.

(34) Arai, H.; Tominaga, H. An Infrared Study of Nitric Oxide Adsorbed on Rhodium-Alumina Catalyst. *J. Catal.* **1976**, *43*, 131–142.

(35) Liang, J.; Wang, H. P.; Spicer, L. D. FTIR Study of NO Chemisorbed on Rh/Al_2O_3. *J. Phys. Chem.* **1985**, *89* (26), 5840–5845.

(36) Li, H.; Rivallan, M.; Thibault-Starzyk, F.; Travert, A.; Meunier, F. C. Effective Bulk and Surface Temperatures of the Catalyst Bed of FT-IR Cells Used for in Situ and Operando Studies. *Physical Chemistry Chemical Physics* **2013**, *15* (19), 7321–7327. https://doi.org/10.1039/c3cp50442e.

(37) Redhead, P. A. Thermal Desorption of Gases. *Vacuum* **1962**, *12* (5), 274.

(38) Campbell, C. T.; Sellers, J. R. V. The Entropies of Adsorbed Molecules. *J. Am. Chem. Soc.* **2012**, *134* (43), 18109–18115.

(39) Zakem, G.; Ro, I.; Finzel, J.; Christopher, P. Support Functionalization as an Approach for Modifying Activation Entropies of Catalytic Reactions on Atomically Dispersed Metal Sites. *J. Catal.* **2021**, *404*, 883–896.

(40)   Wovchko, E. A.; Zubkov, T. S.; Yates, J. T. Electronic Excitation of $Rh^I(CO)_2$ Species on Al_2O_3 Surfaces : Photodissociation of the Rh^I- CO Bond. *J. Phys. Chem. B* **1998**, *102*, 10535–10541.

(41)   Wovchko, E. A.; Yates, J. T. Chemical Bond Activation on Surface Sites Generated Photochemically from $Rh^I(CO)_2$ Species. *Langmuir* **1999**, *15* (10), 3506–3520.

(42)   Morterra, C.; Magnacca, G. A Case Study: Surface Chemistry and Surface Structure of Catalytic Aluminas, as Studied by Vibrational Spectroscopy of Adsorbed Species. *Catalysis Today* **1996**, *27* (3–4), 497–532. https://doi.org/10.1016/0920-5861(95)00163-8.

(43)   Busca, G. The Surface of Transitional Aluminas: A Critical Review. *Catalysis Today* **2014**, *226*, 2–13.

(44)   Phung, T. K.; Herrera, C.; Larrubia, M. Á.; García-Diéguez, M.; Finocchio, E.; Alemany, L. J.; Busca, G. Surface and Catalytic Properties of Some γ-Al2O 3 Powders. *Applied Catalysis A: General* **2014**, *483*, 41–51. https://doi.org/10.1016/j.apcata.2014.06.020.

(45)   Batista, A. T. F.; Baaziz, W.; Taleb, A. L.; Chaniot, J.; Moreaud, M.; Legens, C.; Aguilar-Tapia, A.; Proux, O.; Hazemann, J. L.; Diehl, F.; Chizallet, C.; Gay, A. S.; Ersen, O.; Raybaud, P. Atomic Scale Insight into the Formation, Size, and Location of Platinum Nanoparticles Supported on γ-Alumina. *ACS Catal.* **2020**, *10*, 4193–4204.

(46)   Kovarik, L.; Genc, A.; Wang, C.; Qiu, A.; Peden, C. H. F.; Szanyi, J.; Kwak, J. H. Tomography and High-Resolution Electron Microscopy Study of Surfaces and Porosity in a Plate-like γ-Al_2O_3. *J. Phys. Chem. C* **2013**, *117*, 179–186.

(47)   Roscioni, O. M.; Dyke, J. M.; Evans, J. Structural Characterization of Supported $Rh^I(CO)_2$/γ-Al_2O_3 Catalysts by Periodic DFT Calculations. *J. Phys. Chem. C* **2013**, *117*, 19464–19470.

(48)   Digne, M.; Sautet, P.; Raybaud, P.; Euzen, P.; Toulhoat, H. Use of DFT to Achieve a Rational Understanding of Acid-Basic Properties of γ-Alumina Surfaces. *J. Catal.* **2004**, *226*, 54–68.

(49)   Raybaud, P.; Chizallet, C.; Mager-Maury, C.; Digne, M.; Toulhoat, H.; Sautet, P. From γ-Alumina to Supported Platinum Nanoclusters in Reforming Conditions: 10 Years of DFT Modeling and Beyond. *J. Catal.* **2013**, *308*, 328–340.

(50)   Krokidis, X.; Raybaud, P.; Gobichon, A. E.; Rebours, B.; Euzen, P.; Toulhoat, H. Theoretical Study of the Dehydration Process of Boehmite to γ-Alumina. *J. Phys. Chem. B* **2001**, *105*, 5121–5130.

(51)   Digne, M.; Sautet, P.; Raybaud, P.; Euzen, P.; Toulhoat, H. Hydroxyl Groups on γ-Alumina Surfaces: A DFT Study. *J. Catal.* **2002**, *211*, 1–5.

(52) Pigeon, T.; Chizallet, C.; Raybaud, P. Revisiting γ-Alumina Surface Models through the Topotactic Transformation of Boehmite Surfaces. *J. Catal.* **2022**, *405*, 140–151.

(53) McHale, J. M.; Auroux, A.; Perrotta, A. J.; Navrotsky, A. Surface Energies and Thermodynamic Phase Stability in Nanocrystalline Aluminas. *Science (1979)* **1997**, *277*, 788–789.

(54) Hietala, J.; Root, A.; Knuuttila, P. The Surface Acidity of Pure and Modified Aluminas in Re/γ-Al$_2$O$_3$ Metathesis Catalysts as Studied by ^{1}H MAS NMR Spectroscopy and Its Importance in the Ethenolysis of 1,5-Cyclooctadiene. *J. Catal.* **1994**, *150*, 46–55.

(55) Al-Abadleh, H. A.; Grassian, V. H. FT-IR Study of Water Adsorption on Aluminum Oxide Surfaces. *Langmuir* **2003**, *19*, 341–347.

(56) Chiche, D.; Chizallet, C.; Durupthy, O.; Chanéac, C.; Revel, R.; Raybaud, P.; Jolivet, J. P. Growth of Boehmite Particles in the Presence of Xylitol: Morphology Oriented by the Nest Effect of Hydrogen Bonding. *Phys. Chem. Chem. Phys.* **2009**, *11*, 11310–11323.

(57) Ngouana Wakou, B. F.; Corral Valero, M.; Raybaud, P. Theoretical Insights into the Interaction of Oxygenated Organic Molecules and Cobalt(II) Precursor with Revisiting γ-Al$_2$O$_3$ Surfaces. *J. Phys. Chem. C* **2018**, *122*, 19560–19574.

(58) Paukshtis, E. A.; Yaranova, M. A.; Batueva, I. S.; Bal'zhinimaev, B. S. A FTIR Study of Silanol Nests over Mesoporous Silicate Materials. *Microporous and Mesoporous Mater.* **2019**, *288*, 109582.

(59) Bukowski, B. C.; Bates, J. S.; Gounder, R.; Greeley, J. Defect-Mediated Ordering of Condensed Water Structures in Microporous Zeolites. *Angew. Chem. Int. Ed.* **2019**, *58*, 16422–16426.

(60) Chen, N. Y. Hydrophobic Properties of Zeolites. *J. Phys. Chem.* **1976**, *80* (1), 60–64.

(61) Li, Z.; Jiang, X.; Xiong, G.; Nie, B.; Liu, C.; He, N.; Liu, J. Towards the Preparation of Binderless ZSM-5 Zeolite Catalysts: The Crucial Role of Silanol Nests. *Catal. Sci. Technol.* **2020**, *10*, 7829–7841.

(62) Sulpizi, M.; Gaigeot, M. P.; Sprik, M. The Silica-Water Interface: How the Silanols Determine the Surface Acidity and Modulate the Water Properties. *J. Chem. Theory Comput.* **2012**, *8*, 1037–1047.

(63) Tsyganenko, A. A.; Filimonov, V. N. Infrared Spectra of Surface Hydroxyl Groups and Crystalline Structure of Oxides. *Journal of Molecular Structure* **1973**, *19* (2), 579–589. https://doi.org/10.1016/0022-2860(73)85136-1.

(64) Zaki, M. I.; Knozinger, H. Carbon Monoxide - a Low Temperature Infrared Probe for the Characterization of Hydroxyl Group Properties on Metal Oxide Surfaces. *Mat. Chem. Phys.* **1987**, *17*, 201–215.

(65)   Hucul, D. A.; Brenner, A. A Strong Metal-Support Interaction between Mononuclear and Polynuclear Transition Metal Complexes and Oxide Supports Which Dramatically Affects Catalytic Activity. *J. Phys. Chem.* **1981**, *85* (5), 496–498.

(66)   Paul, D. K.; Marten, C. D.; Yates, J. T. Control of $Rh^I(CO)_2$ Formation on Rh/Al_2O_3 Catalysts by Complexation of Surface -OH Groups Using NH_3. *Langmuir* **1999**, *15*, 4508–4512.

(67)   Van't Blik, H. F. J.; van Zon, J. B. A. D.; Huizinga, T.; Vis, J. C.; Koningsberger, D. C.; Prins, R. Structure of Rhodium in an Ultradispersed $Rh/\gamma-Al_2O_3$ Catalyst as Studied by EXAFS and Other Techniques. *J. Am. Chem. Soc.* **1985**, *107* (11), 3139–3147.

(68)   Chuang, S. S. C.; Tan, C. D. Combined Infrared and Mass Spectrometric Study of Reactions of Adsorbed NO and CO on 0.5 Wt% Rh/SiO_2 Catalyst. *Catal. Today* **1997**, *35*, 369–377.

(69)   Zhang, J.; Asokan, C.; Zakem, G.; Christopher, P.; Medlin, J. W. Enhancing Sintering Resistance of Atomically Dispersed Catalysts in Reducing Environments with Organic Monolayers. *Green Energy and Environment* **2021**, 4–10.

(70)   Valero, M. C.; Raybaud, P.; Sautet, P. Influence of the Hydroxylation of $\gamma-Al_2O_3$ Surfaces on the Stability and Diffusion of Single Pd Atoms: A DFT Study. *J. Phys. Chem. B* **2006**, *110*, 1759–1767.

(71)   Hecker, W. C.; Bell, A. T. Reduction of NO by CO over Silica-Supported Rhodium: Infrared and Kinetic Studies. *J. Catal.* **1983**, *84*, 200–215.

(72)   Yoo, C. J.; Getsoian, A. (Bean); Bhan, A. NH_3 Formation Pathways from NO Reduction by CO in the Presence of Water over Rh/Al_2O_3. *Appl. Catal., B* **2021**, *286*, 119893.

(73)   Solymosi, F.; Bansagi, T. Infrared Spectroscopic Study of the Adsorption of Isocyanic Acid. *J. Phys. Chem.* **1979**, *83* (4), 552–553.

(74)   Serna, P.; Gates, B. C. Zeolite-Supported Rhodium Complexes and Clusters: Switching Catalytic Selectivity by Controlling Structures of Essentially Molecular Species. *J. Am. Chem. Soc.* **2011**, *133*, 4714–4717.

(75)   Matsubu, J. C.; Yang, V. N.; Christopher, P. Isolated Metal Active Site Concentration and Stability Control Catalytic CO_2 Reduction Selectivity. *J. Am. Chem. Soc.* **2015**, *137*, 3076–3084.

(76)   Asokan, C.; Thang, H. V.; Pacchioni, G.; Christopher, P. Reductant Composition Influences the Coordination of Atomically Dispersed Rh on Anatase TiO_2. *Catal. Sci. Technol.* **2020**, *10*, 1597–1601.

(77)   Doherty, F.; Goldsmith, B. R. Rhodium Single-Atom Catalysts on Titania for Reverse Water Gas Shift Reaction Explored by First Principles Mechanistic Analysis and Compared to Nanoclusters. *ChemCatChem* **2021**, *13*, 3155–3164.

(78)   Thang, H. V.; Pacchioni, G. On the Real Nature of Rh Single-Atom Catalysts Dispersed on the ZrO_2 Surface. *ChemCatChem* **2020**, *12*, 2595–2604.

(79)   Peri, J. B. A Model for the Surface of γ-Alumina. *J. Phys. Chem.* **1965**, *69* (1), 220–230.

(80)   van Zon, J. B. A. D.; Koningsberger, D. C.; Van't Blik, H. F. J.; Prins, R.; Sayers, D. E. On the Detection with EXAFS of Metal-Support Oxygen Bonds in a Highly Dispersed Rhodium on Alumina Catalyst. *J. Chem. Phys.* **1984**, *80*, 3914–3915.

(81)   Kraushofer, F.; Haager, L.; Eder, M.; Rafsanjani-Abbasi, A.; Jakub, Z.; Franceschi, G.; Riva, M.; Meier, M.; Schmid, M.; Diebold, U.; Parkinson, G. S. Single Rh Adatoms Stabilized on α-Fe_2O_3 (1$\bar{1}$02) by Coadsorbed Water. *ACS Energy Lett.* **2021**, *7*, 375–380.

(82)   Schroeder, E. K.; Finzel, J.; Christopher, P. Photolysis of Atomically Dispersed Rh/Al_2O_3 Catalysts: Controlling CO Coverage in Situ and Promoting Reaction Rates. *Manuscript submitted for publication*.

(83)   Schultz, R. H.; Bengali, A. A.; Tauber, M. J.; Weiller, B. H.; Wasserman, E. P.; Kyle, K. R.; Moore, C. B.; Bergman, R. G. IR Flash Kinetic Spectroscopy of C-H Bond Activation of Cyclohexane-d_0 and -d_{12} by Cp∗$Rh(CO)_2$ in Liquid Rare Gases: Kinetics, Thermodynamics, and an Unusual Isotope Effect. *J. Am. Chem. Soc.* **1994**, *116* (16), 7369–7377.

(84)   Ford, P. C.; Ryba, D. W.; Belt, S. T. Reactive Intermediates in the Carbonylation of Metal—Alkyl Bonds. *Advances in Chemistry Series* **1993**, 27–43.

(85)   Qingxin, M.; Liu, Y.; He, H. Synergistic Effect between NO2 and So2 in Their Adsorption and Reaction on γ-Alumina. *Journal of Physical Chemistry A* **2008**, *112* (29), 6630–6635. https://doi.org/10.1021/jp802025z.

(86)   Börensen, C.; Kirchner, U.; Scheer, V.; Vogt, R.; Zellner, R. Mechanism and Kinetics of the Reactions of NO2 or HNO3 with Alumina as a Mineral Dust Model Compound. *Journal of Physical Chemistry A* **2000**, *104* (21), 5036–5045. https://doi.org/10.1021/jp994170d.

(87)   Anderson, J. A.; Millar, G. J.; Rochester, C. H. Infrared Study of the Adsorption of NO, NO2 and CO on Rh/AI2O3 Catalysts. *J. Chem. Soc. Faraday Trans.* **1990**, *86* (3), 571–576.

(88)   Wey, J. P.; Neely, W. C.; Worley, S. D. Infrared Spectroscopy at High Pressure: Interaction of CO with Oxidized Rh/Al_2O_3. *J. Catal.* **1992**, *134*, 378–381.

(89) Wovchko, E. A.; Yates, J. T. Activation of O_2 on a Photochemically Generated Rh^I Site on an Al_2O_3 Surface: Low-Temperature O_2 Dissociation and CO Oxidation. *J. Am. Chem. Soc.* **1998**, *120* (40), 10523–10527.

(90) Kecskés, T.; Raskó, J.; Kiss, J. FTIR and Mass Spectrometric Study of HCOOH Interaction with TiO_2 Supported Rh and Au Catalysts. *Appl. Catal., A* **2004**, *268*, 9–16.

(91) Rege, S. U.; Yang, R. T. A Novel FTIR Method for Studying Mixed Gas Adsorption at Low Concentrations : H_2O and CO_2 on NaX Zeolite and Alumina. *Chem. Eng. Sci.* **2001**, *56*, 3781–3796.

(92) Wovchko, E. A.; Yates, J. T.; Pennsyl, V.; February, R. v. Photochemical Activation of CO_2 on $Rh^I(CO)_2/Al_2O_3$–CO_2 Dissociation and Oxygen Atom Exchange. *J. Am. Chem. Soc.* **2004**, *7863* (17), 7544–7550.

(93) Szanyi, J.; Kwak, J. H. Dissecting the Steps of CO_2 Reduction: 1. The Interaction of CO and CO_2 with $γ$-Al_2O_3: An in Situ FTIR Study. *Physical Chemistry Chemical Physics* **2014**, *16* (29), 15117–15125.

(94) Morterra, C.; Boccuzzi, F.; Coluccia, S.; Ghiotti, G. Infrared Study of the Adsorption of Nitrous Oxide on $η$-Alumina. *J. Catal.* **1980**, *65*, 231–234.

(95) Westerberg, B.; Fridell, E. A Transient FTIR Study of Species Formed during NOx Storage in the $Pt/BaO/Al_2O_3$ System. *J. Mol. Catal. A: Chem.* **2001**, *165*, 249–263.

(96) Nelson, N. C.; Nguyen, M. T.; Glezakou, V. A.; Rousseau, R.; Szanyi, J. Carboxyl Intermediate Formation via an in Situ-Generated Metastable Active Site during Water-Gas Shift Catalysis. *Nature Catalysis* **2019**, *2* (10), 916–924.

(97) Miller, T. M.; Grassian, V. H. Heterogeneous Chemistry of NO_2 on Mineral Oxide Particles: Spectroscopic Evidence for Oxide-Coordinated and Water-Solvated Surface Nitrate. *Geophysical Research Letters* **1998**, *25* (20), 3835–3838.

(98) Baltrusaitis, J.; Jensen, J. H.; Grassian, V. H. FTIR Spectroscopy Combined with Isotope Labeling and Quantum Chemical Calculations to Investigate Adsorbed Bicarbonate Formation Following Reaction of Carbon Dioxide with Surface Hydroxyl Groups on Fe_2O_3 and Al_2O_3. *Journal of Physical Chemistry B* **2006**, *110* (24), 12005–12016.

(99) Feng, X.; Wang, Z.; Mu, L.; Chen, Z.; Liang, J.; Xiao, C. The Different Evolution Behaviors of Carbonate-like Species on Pt/CeO_2 and Pt/Al_2O_3 by in Situ DRIFTS-MS Study. *Catalysis Today* **2021**, *400–401*, 1–7.

(100) Lee, I.; Zaera, F. Catalytic Oxidation of Carbon Monoxide at Cryogenic Temperatures. *J. Catal.* **2014**, *319*, 155–162.

(101) Muir, M.; Molina, D. L.; Islam, A.; Abdel-Rahman, M. K.; Trenary, M. Adsorption Properties of Acrolein, Propanal, 2-Propenol, and 1-Propanol on Ag(111). *Phys. Chem. Chem. Phys.* **2020**, *22* (43), 25011–25020.

(102) Cotton, F. A.; Wilkinson, G. *Advanced Inorganic Chemistry*, 3rd ed.; John Wiley & Sons, 1972.

(103) Srinivasan, P. D.; Nitz, S. R.; Stephens, K. J.; Atchison, E.; Bravo-Suarez, J. J. Modified Harrick Reaction Cell for in Situ/Operando Fiber Optics Diffuse Reflectance UV–Visible Spectroscopic Characterization of Catalysts. *Appl. Catal., A* **2018**, *561*, 7–18.

(104) Hoffman, A. J.; Asokan, C.; Gadinas, N.; Schroeder, E.; Zakem, G.; Nystrom, S. v.; Getsoian, A.; Christopher, P.; Hibbitts, D. Experimental and Theoretical Characterization of Rh Single-Atoms Supported on γ-Al$_2$O$_3$ with Varying Hydroxyl Content during NO Reduction by CO. *In revision for publication in ACS Catalysis*.

Appendix. Author Contributions

Primary author: Nick Gadinas

Contributors: Alex Hoffman, Chithra Asokan, Emily Schroeder, Phil Christopher, David Hibbitts, Andrew Getsoian.

Chapter 1. Introduction

This chapter was written by NG.

Chapter 2. Experimental Methods

Sections 2.1, 2.2, and 2.4 were written by CA and adapted from Ref. 104. Section 2.3 was written by NG.

Chapter 3. Hydroxyl Interactions with $Rh(CO)_2$

The writing in this chapter was shared by NG (60%), CA (20%), and AH (20%) and adapted from Ref. 104. Figures 2–9 were produced by AH with data collected by CA (2, 4, 5), AH (8, 9), NG and ES (6, 7). Figure 10 was produced by NG. Initial conceptual design of this work originated from AH, CA, DH, AG, and PC, but the final conclusions of this work involved discussion primarily with NG, ES, and PC.

Chapter 4. Identification of a Reactive Intermediate in the NO-CO Reaction

This chapter was written by NG. Data in Figure 12 was collected by CA, and Figure 15 and Table 3 were produced by AH. All other data and figures were produced by NG. Conceptual design of this work originated from NG, ES, and PC.

Chapter 5. Interactions between $Rh(CO)_2$, NO and CO derived support species, and *OH

The data in Figure 17 was collected by CA, and the figure was produced by AH. All other writing, data collection, and figure production was performed by NG. Conceptual design of this work originated from NG.

Chapter 6. IR of Atomically Dispersed $Rh/\gamma\text{-}Al_2O_3$ at or near Reaction Conditions

The text, data, and figures in this section were produced by NG. Concepts in this section originated from NG and PC.

Chapter 7. Conclusions and Suggested Experiments

The text and figures in this section were produced by NG.